

# Three Tales of Two Theories

*Experimental Investigations of Inelastic Charge Transport in Nanoscopic Junctions*

E-Dean Fung

Submitted in partial fulfillment of the  
requirements for the degree of  
Doctor of Philosophy  
under the Executive Committee  
of the Graduate School of Arts and Sciences

COLUMBIA UNIVERSITY

2020

© 2020

E-Dean Fung

All Rights Reserved

## Abstract

Three Tales of Two Theories: Experimental Investigations of Inelastic Charge Transport in Nanoscopic Junctions

E-Dean Fung

Since the single-molecule diode was first envisioned by Aviram and Ratner in 1974, researchers have investigated how the electronic properties of molecules might be designed to achieve a variety of device functionality. However, although electron-phonon and electron-photon interactions have been studied in systems where the molecule is poorly electronically coupled to the environment, only a few experimental modalities exist for studying inelastic transport in two-terminal single-molecule junctions. Furthermore, each phenomena typically has a few possible mechanisms which must be distinguished. The objective of this dissertation is to expand the experimental tools available for probing inelastic transport in single-molecule junctions, with special attention to electron-photon interactions.

Throughout the dissertation, we utilize the scanning tunneling microscope break-junction technique to form either tunnel junctions or single-molecule junctions. By repeatedly pushing and pulling a Au STM tip into a Au-coated mica substrate, a variety of junction geometries are sampled to give a distribution of device performances. Transport and optical measurements are made while controlling the electrode displacement and junction bias independently, which permits flexible experimental design.

The body of the dissertation is divided into three chapters, each chapter exploring a different phenomenon. In the first chapter, I study light emission from tunnel junctions driven at high bias. It was shown previously that electroluminescence from tunnel junctions can have photon energies exceeding the classical limit, so-called overbias emission. Multi-electron processes and blackbody

radiation have been proposed as possible explanations for this extraordinary result. We demonstrate that the intensity of the overbias emission depends superlinearly on the junction conductance even at room temperature, which strongly supports the theory from multi-electron processes. Additionally, we show that blackbody radiation-like effects can be produced by multi-electron processes.

In the second chapter, I demonstrate experimentally the enhanced conductance of single-molecule junctions under illumination. Again, we consider two mechanisms for enhancement, namely photon-assisted tunneling and hot-electron distributions. By carefully comparing the two theories, we find that their steady-state signatures are nearly identical, but that the contribution from hot-electron distributions is larger in our system. This is confirmed by measuring a conductance enhancement at a polarization where photon-assisted tunneling is negligible.

In the third chapter, I explore both junction rupture and nonlinear transport phenomena in single-molecule junctions around the resonant tunneling regime. Importantly, we develop non-linear regression curve-fitting to allow straightforward extraction of key transport parameters on individual single-molecule junctions. We observe a strong correlation between the bias at which the junction ruptures and the level alignment of the dominant transport orbital, which suggests that, in the resonant tunneling regime, the tunneling electrons interact strongly with the nuclear degrees of freedom.

However, we also find that not all junctions rupture and those that sustain display negative differential resistance and hysteresis. We hypothesize that this nonlinear behavior is due to a change in the charge state of the molecule. We study the stability of this charge state and find that the dynamics of charging and discharging occur on millisecond timescales. Although the blocking-state and polaron models each predict parts of our data, neither are fully consistent with the experiments in their entirety. This reveals opportunities for further experimental and theoretical investigations into transport in the resonant tunneling regime.

## Table of Contents

List of Tables . . . . .	iv
List of Figures . . . . .	v
Acknowledgments . . . . .	viii
Dedication . . . . .	x
Chapter 1: Introduction . . . . .	1
1.1 The Landauer-Büttiker Formalism . . . . .	2
1.2 The Scattering Matrix . . . . .	6
1.3 Inelastic Transport and Incoherence . . . . .	8
1.4 STM Break-Junction Technique . . . . .	10
1.5 Thesis Outline . . . . .	13
Chapter 2: Too Cool for Blackbody Radiation . . . . .	14
2.1 Preface . . . . .	14
2.2 Introduction . . . . .	14
2.3 Experimental Methods . . . . .	15
2.4 Multi-Electron Processes . . . . .	17
2.5 Blackbody Radiation . . . . .	21

2.6	Conclusions . . . . .	25
2.7	Supplementary Information . . . . .	25
2.7.1	Data Analysis Methods . . . . .	25
2.7.2	Coulomb Blockade Model . . . . .	27
2.7.3	Variability in $\beta$ . . . . .	30
2.7.4	The Role of $D(E)$ . . . . .	32
Chapter 3: Too Hot for Photon-Assisted Transport . . . . .		35
3.1	Preface . . . . .	35
3.2	Introduction . . . . .	35
3.3	Experimental Methods . . . . .	37
3.4	Experimental Results . . . . .	37
3.5	Theoretical Discussion . . . . .	41
3.6	Conclusion . . . . .	46
3.7	Supplementary Information . . . . .	46
3.7.1	Additional Data . . . . .	46
3.7.2	Theory for Non-Equilibrium Electron Distributions . . . . .	47
3.7.3	Equivalence of Photon-Assisted Tunneling and Hot-Electron Transport . . .	48
3.7.4	Derivation for $\Delta\rho_0$ . . . . .	49
3.7.5	Additional Calculations . . . . .	50
Chapter 4: Breaking Down Resonance . . . . .		52
4.1	Preface . . . . .	52
4.2	Introduction . . . . .	52

4.3 Current-Voltage Measurements . . . . .	54
4.4 Curve-Fitting . . . . .	55
4.5 Charging Dynamics . . . . .	58
4.6 Theoretical Discussion . . . . .	61
4.7 Conclusion . . . . .	64
4.8 Supplementary Information . . . . .	65
4.8.1 Additional Data . . . . .	65
4.8.2 Selection Algorithm for <i>I</i> - <i>V</i> Data . . . . .	67
4.8.3 Reversibility Experiment . . . . .	70
4.8.4 Curve Fitting . . . . .	71
4.8.5 Fitting the Polaron Model in Polar Solvent . . . . .	74
4.8.6 Density Functional Theory-Based Transport Calculations of Squaraine . . . . .	75
Conclusions and Outlook . . . . .	77
References . . . . .	102

## **List of Tables**

3.1	Measured peak-conductance values and calculated on-off ratios. . . . .	39
3.2	Measured peak-conductance values and calculated on-off ratios for polarization perpendicular to the plane of incidence . . . . .	47
4.1	Number of traces after each selection algorithm . . . . .	69
4.2	Estimated reorganization energies . . . . .	75

## List of Figures

1.1	Schematic of single-molecule junction . . . . .	1
1.2	Transmission function and frontier orbitals for 1,4-diaminobenzene . . . . .	4
1.3	Transmission function for single-level model and visualization of bias window . . .	5
1.4	Schematic of scattering matrix formalism . . . . .	6
1.5	Schematic of inelastic transport via coupling to a single vibrational mode . . . . .	9
1.6	Schematic of scanning tunneling microscope and graph of a conductance trace . . .	11
1.7	1D and 2D conductance histograms of 4,4'-bipyridine . . . . .	12
2.1	Schematic of STM modified for light detection . . . . .	15
2.2	Visualization of experimental design and 2D photovoltage-conductance histograms for light emission experiment . . . . .	16
2.3	Electroluminescence spectrum collected with bandpass filters . . . . .	17
2.4	Illustrations of mechanisms for overbias light emission . . . . .	18
2.5	Calculated spectrum for fixed conductance and integrated spectra as a function of conductance . . . . .	20
2.6	2D photovoltage-conductance histograms for underbias and overbias electrolumi- nescence and supporting theoretical calculation . . . . .	21
2.7	Theoretical spectra from multi-electron processes at 2000 K and conductance de- pendence of blackbody radiation . . . . .	22
2.8	Results from Buret <i>et al.</i> reproduced using multi-electron process theory . . . . .	23

2.9	Results from Downes <i>et al.</i> reproduced using multi-electron process theory . . . . .	24
2.10	2D photovoltage-conductance histograms for light emission experiments performed with bandpass filters . . . . .	26
2.11	Comparisons between Xu model and approximate model . . . . .	29
2.12	Histograms of fitted $\beta$ for three different applied biases . . . . .	31
2.13	Electroluminescence data collected without filters and with $2\text{ k}\Omega$ resistor . . . . .	32
2.14	Additional calculations exploring the effect of $D(E)$ . . . . .	33
3.1	Schematic of STM modified for illuminated break-junction measurements . . . . .	36
3.2	Optical image of illuminated STM tip . . . . .	37
3.3	1D conductance histograms of dark and illuminated 4,4'-bipyridine junctions and extracted peak-conductances for a series of measurements alternating illumination .	38
3.4	Temperature dependent measurements of 4,4'-bipyridine junctions . . . . .	40
3.5	2D conductance histograms of 4,4'-bipyridine junctions with and without illumination and displacement-controlled 1D conductance histogram . . . . .	41
3.6	Diagrams and calculations showing the near-equivalence of photon-assisted tunneling and hot-electron charge transport . . . . .	44
3.7	1D conductance histograms and extracted peak-conductances for junctions illuminated with light polarized perpendicular to the plane of incidence . . . . .	45
3.8	Non-equilibrium hot-electron distributions and conductance enhancement due to localized and propagating surface plasmons . . . . .	48
3.9	Additional calculations of enhancement ratio as a function of junction bias . . . . .	50
4.1	Molecular structure of TDO4 and squaraine . . . . .	53
4.2	Sample trace showing experimental design and 2D current-time histograms for $I$ - $V$ measurement of TDO4 junctions in TCB . . . . .	54
4.3	Sample $I$ - $V$ trace and correlation histogram between threshold bias and level alignment of TDO4 junctions in TCB . . . . .	56

4.4	Histograms of fitted $\varepsilon$ and $\Gamma$ for TDO4 junctions measured in TCB before and after charging . . . . .	57
4.5	Dependence of threshold bias on ramp speed . . . . .	59
4.6	2D current-time histograms of sequential bias ramps demonstrating reversibility . .	60
4.7	Percent of junctions reversed as a function of hold bias and hold time . . . . .	61
4.8	Diagrams for models of NDR and hysteresis in single-molecule junctions . . . . .	62
4.9	2D current-time histogram of aligned traces showing abrupt NDR and histogram of peak-to-valley ratios for TDO4 junctions in TCB . . . . .	65
4.10	Summary of data analysis for $I$ - $V$ experiments of TDO4 and squaraine junctions measured in TCB and PC . . . . .	66
4.11	Summary of data analysis for reversibility experiments of TDO4 and squaraine junctions measured in TCB and PC . . . . .	67
4.12	Visualization of selection algorithms for $I$ - $V$ experiment . . . . .	68
4.13	Visualization of selection algorithms for reversibility experiment . . . . .	70
4.14	Comparison between Landauer formalism with and without low-temperature approximation and comparison between fitting on linear and logarithmic scales . . . .	72
4.15	Histograms of root-mean-square error from curve-fitting . . . . .	73
4.16	$I$ - $V$ trace showing typical root-mean-square error and dependence of fitted $\varepsilon$ on threshold bias . . . . .	74
4.17	Histograms of fitted $\varepsilon$ and $\Gamma$ for experiments performed in polar solvent assuming the polaron model . . . . .	75
4.18	Calculated transmission function and isosurfaces of resonant scattering states for squaraine junctions . . . . .	76

## Acknowledgements

First and foremost, I am deeply indebted to my advisor, Prof. Latha Venkataraman. She continues to inspire me with her unparalleled work ethic, her incisive intellect, and her uncompromising integrity. More importantly, her ability to balance her commitment to her students, the academic community, and her family is extraordinary. For her priceless mentorship, for indulging my academic interests, and for her generosity in difficult times, I will forever be grateful.

Second, I would be remiss not to thank Prof. Nanfang Yu for his early support. Seven years ago when I had no research experience and a middling resume, he gave me the opportunity to do research and, more importantly, spent his precious time as a young assistant professor to mentor me. I can say with confidence that I would not be where I am today without his initial act of charity.

I must thank the many synthetic chemists with whom I have collaborated without much success (at least as measured by publications): Melissa Ball, Natalia Gadjieva, Jonathan Lo, Evan Doud, Marta Diez Castellnou, Mariano Macchione, Fay Ng, Prof. Stefan Matile, and Prof. Colin Nuckolls. I am afraid any seeds of knowledge contained in the fruits of their labor fell on fallow ground due to my utter lack of chemical intuition, but I am grateful for their hard work and for teaching me what little I know about chemical nomenclature.

Many thanks to Anders Borges, Marc Garner, Prof. Gemma Solomon, David Gelbwaser, Prof. Uri Peskin, and Prof. Misha Galperin for both fruitful collaborations and their tutelage. It has taken me five years to even begin to understand non-equilibrium Green's functions, and my admiration for their work has grown proportionally.

Thank you to Prof. Chris Marianetti for his class on density function theory, which has proven more critical to my understanding than I could have anticipated. And my sincere gratitude to Prof. Ana Asenjo-Garcia for agreeing to serve on my defense committee.

My thanks to Sajan Shrestha, Adam Overvig, and Aaron Sternbach for their advice and help designing the light detection apparatus. I could not have done it without them.

To the chemistry graduate students and in particular to James, thank you for the happy hours and for being so incredibly hospitable. The sense of community you foster is truly enviable.

To the alumni of the Venkataraman lab, both those I have worked with and those I have yet to meet, thank you for paving the way, for the advice and guidance, and, in many cases, for directly inspiring this work. To the current members of the lab, your brilliance and creativity never cease to amaze me. Thank you all for making graduate school a joy.

Jyoti, Mel, Owen, Sai, Shaowen, Tim, and Yi. My APAM comrades. We made it! Thank you for the solidarity over the years.

To Wen Xuan, Peijie, and the Goldhersz family, thank you for your generosity in my first year in New York City.

To Chris and Dennis, for the years of steadfast friendship, thank you.

To my sister, for always being there in my times of need, thank you.

The final thanks goes to my mother and father, for the countless unrecognized sacrifices over the years. Spending six years in academic purgatory is a luxury paid for by their unyielding love and support. If I have achieved anything worthwhile in my time here, all the credit must go to them.

*To my mother and father*

## Chapter 1: Introduction

Single-molecule electronics is the study of electron transport through single-molecule systems [1]. Like solid-state and organic electronics, single-molecule electronics seeks to characterize, understand, and optimize the properties relevant to making useful devices. Unlike traditional electronics, these properties are determined by the details of the molecular structure and are not averaged over the bulk. This makes single-molecule devices at once more precise and more variable. More precise, because the form of the molecule is determined with atomic precision. More variable, because small differences in geometry can result in measurable differences in transport [2–5]. Of course, the electronic properties of molecules themselves is the foundation of modern chemistry. In single-molecule electronics, however, the molecule can be strongly influenced by its interaction with electrodes, which are still described by mesoscopic physics. It is this interplay between solid-state physics and quantum chemistry that make single-molecule electronics both challenging and fascinating.

Figure 1.1 depicts a schematic of a two-terminal single-molecule device and highlights its different components. Specifically, the device is composed of the left and right electrodes, the molecular bridge, and the solvent environment. For the systems I will consider, the molecular bridge can be further decomposed into the anchoring functional groups (linkers) and the molecular backbone.

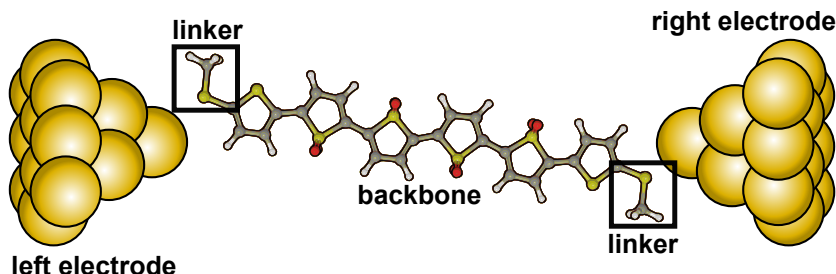


Figure 1.1: Schematic of single-molecule junction.

Importantly, the anchoring groups ensure that the molecule is electronically well-coupled to both electrodes. Such devices are commonly referred to as single-molecule junctions [6–9].

Each component of the device can be selected to produce different effects. Naturally, the design of the molecular bridge has played the central role in the field of single-molecule electronics since the landmark paper by Aviram and Ratner in 1974 [10]. By carefully choosing the structural, chemical, and electronic properties [11, 12], single-molecular conductors [13–22], insulators [23–25], switches [26–35], diodes [36–40], and transistors [41–48] have been realized. Subtle quantum phenomena such as interference [49–56] and spin [57–64] have also been utilized to achieve novel functionality. Moreover, the choice of electrode [65–69] and even the solvent environment [40, 70, 71] can be used to improve device performance.

Transport through single-molecule junctions is largely described by off-resonant, coherent, and elastic electron tunneling. In this dissertation, I will primarily relax the last restriction and investigate inelastic electron tunneling, with special attention to electron-photon interactions. These phenomena are more commonly studied in single-molecule systems that are weakly electronically coupled to their environment but are poorly represented in their well-coupled counterparts. By investigating the different mechanisms by which the non-electronic environment can influence transport, this work advances our understanding of charge transport in nanoscale systems and paves the way towards single-molecule optoelectronics.

In the first section of this introduction, I will introduce the Landauer-Büttiker formalism, which models the standard case of coherent and elastic tunneling. In Section 1.2, I use the scattering matrix formalism to clarify the meaning of elastic and coherent tunneling before reviewing inelastic and incoherent transport in Section 1.3. Finally, I will describe the Scanning Tunneling Microscope Break-Junction (STM-BJ) technique, which provides a base for studying electron transport in single-molecule systems, before presenting an outline of the dissertation.

## 1.1 The Landauer-Büttiker Formalism

I reference [72] heavily throughout the introduction and refer to it as Cuevas and Scheer.

The Landauer-Büttiker formalism is the theoretical workhorse for modelling transport in single-molecule junctions [73, 74]. The most widely used form in the context of single-molecule junction measurements relates the junction current  $I$  to the junction bias  $V$ .

$$I(V) = \frac{2e}{h} \int_{-\infty}^{\infty} dE T(E) \left[ f_L \left( E - \frac{eV}{2} \right) - f_R \left( E + \frac{eV}{2} \right) \right] \quad (1.1)$$

$E$  is the energy of the electron,  $e$  is the elementary charge,  $h$  is Planck's constant,  $T(E)$  is the transmission function, and  $f(E)$  is the Fermi distribution. Eq 1.1 lends itself to the following interpretation from probability. At every energy, the electron has some probability of tunneling through the junction, and this probability is given by the transmission function. For an electron to tunnel from the left electrode at energy  $E$ , an electron must occupy one of the states at energy  $E$  in the left electrode, and the probability of this occurring is given by the Fermi distribution  $f_L(E)$ . The net current from left to right must also include currents moving from the right electrode to the left; this accounts for  $f_R(E)$ .<sup>1</sup> Finally, to obtain the total current, we must sum across all possible energies, each interval  $dE$  contributing a charge  $e$  to the current with a factor of 2 for the spin degeneracy. At this level of analysis, Planck's constant simply produces the correct units for current. Chapter 4.3 of Cuevas and Scheer provides a derivation consistent with this interpretation where Planck's constant arises more naturally.

All the information about the molecule and its interactions with the electrodes is contained in the transmission function. In Figure 1.2a, we graph the transmission function calculated for a molecule (1,4-diaminobenzene) coupled to two gold electrodes. Note that we specify the electrodes as well as the molecule; the transmission function involves the density of states of both. For gold electrodes, the density of states is relatively flat for energies above  $-2\text{ eV}$  and can be safely ignored in this energy range [75, 76]. In the transmission function, we observe a number of peaks or resonances. The location of each resonance in the transmission function corresponds to the energy alignment of a molecular orbital to the Fermi energy [77–80], and their widths correspond to how

---

<sup>1</sup>This heuristic description ignores that an empty state must be available in the opposing electrode, but the additional terms from including this cancel.

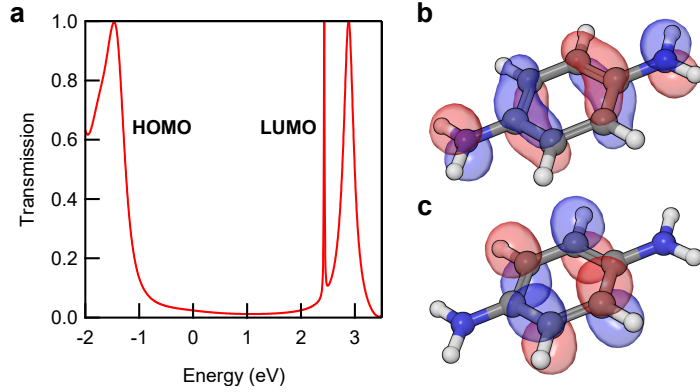


Figure 1.2: (a) Transmission function for 1,4-diaminobenzene single-molecule junction, computed with FHI-aims [82, 83]. Isosurfaces of (b) HOMO and (c) LUMO, calculated with Jaguar [84].

well each molecular orbital is coupled electronically to the electrodes [81].

For 1,4-diaminobenzene, we see that the highest occupied molecular orbital (HOMO) is better coupled to the electrodes than the lowest unoccupied molecular orbital (LUMO). This can be understood by looking at the molecular orbitals of the molecule in gas phase, i.e. without the electrodes. We calculate this using density functional theory (DFT) and show the isosurfaces of the HOMO and LUMO orbitals in Figure 1.2b,c. We observe that the HOMO has significant electron density on the anchoring amines, whereas the LUMO does not. For this reason, there is very little orbital overlap between the LUMO and the electrodes, resulting in weak electronic coupling. This explains the difference in coupling seen in the transmission function.

Throughout this dissertation, I will assume that only one of the frontier orbitals (HOMO or LUMO) contributes significantly to transport. This is typically justified when one of the frontier orbitals lies much closer to the Fermi energy than the other. More precisely, I will model the single-molecule junction as a single energy level coupled to the electrodes (Sections 5.3.3 and 8.1.1 of Cuevas and Scheer), commonly referred to as the single-level model [85]. In this model, the coupling is independent of energy (wide-band limit); this accounts for the flat density of states of gold. The transmission function for the single-level model is given by

$$T(E) = \frac{\Gamma_L \Gamma_R}{(E - \varepsilon)^2 + \left(\frac{\Gamma_L + \Gamma_R}{2}\right)^2} \quad (1.2)$$

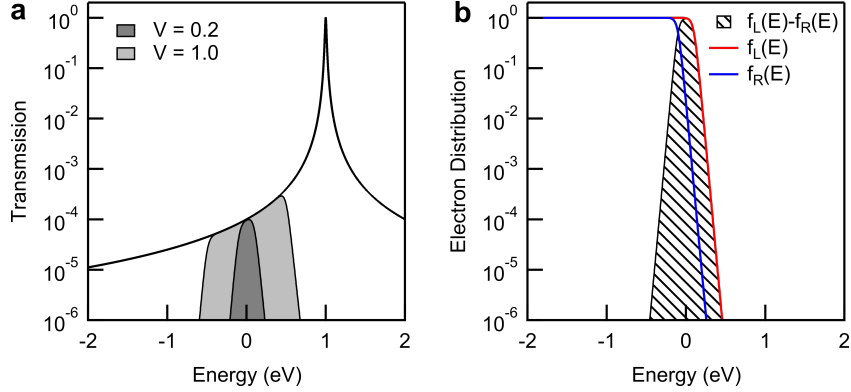


Figure 1.3: (a) Transmission function for the single-level model on a semi-log plot.  $\varepsilon = 1$  eV and  $\Gamma = 10$  meV. (b) Left and right Fermi distributions (red and blue, respectively) for a junction bias of 0.2 V. The difference is the shaded area.

Eq 1.2 is referred to as the Breit-Wigner or Lorentzian line shape [86, 87].  $\Gamma_L$  and  $\Gamma_R$  are the couplings to the left and right electrodes, respectively, and  $\varepsilon$  is the alignment of the orbital with respect to the Fermi energy. We will often assume symmetric coupling ( $\Gamma_L = \Gamma_R = \Gamma$ ), in which case Eq 1.2 can be simplified to

$$T(E) = \frac{\Gamma^2}{(E - \varepsilon)^2 + \Gamma^2} \quad (1.3)$$

The current as a function of junction bias can then be calculated using Eq 1.1 and either Eq 1.2 or 1.3.

Figure 1.3a shows the transmission function for reasonable values of  $\varepsilon$  and  $\Gamma$ . Unlike Figure 1.2a, we plot the transmission function on a semi-logarithmic scale to show the transmission probability decays monotonically with distance from the resonance ( $E = \varepsilon$ ). I plot the left and right Fermi distributions for a bias of 0.2 V, as well as their difference, in Figure 1.3b. The effect of the Fermi distributions is to select a range of energies between which the transmission function will be integrated. The current is then proportional to the area under the transmission function selected by this bias window (shaded regions of Fig 1.3a).

## 1.2 The Scattering Matrix

The previous section represents the minimum necessary theoretical background for this dissertation. In what follows, I will describe the scattering model of transport from which Eq 1.1 can be derived [88–90]. This will elucidate the meaning of elastic and coherent tunneling and clarify how they are integral to the Landauer-Büttiker formalism.

In the scattering model of transport, the details of the bridge between the two terminals is completely ignored, and we only consider how the bridge scatters incoming electronic states to outgoing electronic states. Following Section 4.7 of Cuevas and Scheer, let us say that the electronic states in each electrode are enumerated over two quantum numbers,  $n$  and  $k$ , where  $n$  enumerates the transverse modes and  $k$  enumerates the longitudinal modes. The total energy  $E$  is just  $E_n + E_k$ . However, because the electrodes are semi-infinite, the longitudinal modes are continuous instead of discrete. This means that for any transverse mode  $n$ , one can find a longitudinal mode  $k$  such that the total energy is  $E$ . Instead of writing the states as  $|n, k\rangle$ , we can write them as  $|n(E)\rangle$ , where we specify the transverse mode and the total energy of the electron. Furthermore, we know that the longitudinal modes are divided into incoming and outgoing modes, which we will call  $|a_n^{L/R}(E)\rangle$  and  $|b_n^{L/R}(E)\rangle$ , respectively. The superscript denotes whether the wavefunction belongs to the left or right lead. Figure 1.4 summarizes the notation.

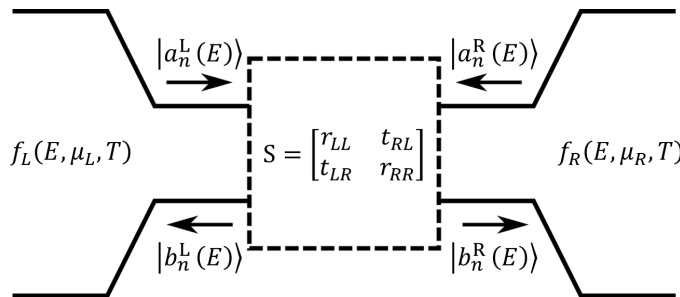


Figure 1.4: Schematic of scattering matrix formalism, adapted from Fig 4.10 in Cuevas and Scheer

$|a_n^{L/R}(E)\rangle$  and  $|b_n^{L/R}(E)\rangle$  form a basis, so an electron in the left/right electrode can written as

$$\psi^{L/R}(E) = \psi_a^{L/R}(E) + \psi_b^{L/R}(E) = \sum_n \alpha_n^{L/R} |a_n^{L/R}(E)\rangle + \sum_n \beta_n^{L/R} |b_n^{L/R}(E)\rangle \quad (1.4)$$

The scattering matix  $S(E)$  describing the transport bridge is defined as

$$\begin{bmatrix} \psi_b^L(E) \\ \psi_b^R(E) \end{bmatrix} = S(E) \begin{bmatrix} \psi_a^L(E) \\ \psi_a^R(E) \end{bmatrix} = \begin{bmatrix} r_{LL}(E) & t_{RL}(E) \\ t_{LR}(E) & r_{RR}(E) \end{bmatrix} \begin{bmatrix} \psi_a^L(E) \\ \psi_a^R(E) \end{bmatrix} \quad (1.5)$$

The left-most vector and the right-most vector are the outgoing and incoming waves, respectively.

In the basis of  $|a_n^{L/R}(E)\rangle$  and  $|b_n^{L/R}(E)\rangle$ , they are

$$\begin{bmatrix} \psi_b^L(E) \\ \psi_b^R(E) \end{bmatrix} = \begin{bmatrix} \beta_1^L \\ \vdots \\ \beta_N^L \\ \beta_1^R \\ \vdots \\ \beta_N^R \end{bmatrix} \quad \begin{bmatrix} \psi_a^L(E) \\ \psi_a^R(E) \end{bmatrix} = \begin{bmatrix} \alpha_1^L \\ \vdots \\ \alpha_N^L \\ \alpha_1^R \\ \vdots \\ \alpha_N^R \end{bmatrix} \quad (1.6)$$

Here, we assumed that the number of transverse modes in the both left and right electrodes is  $N$ .

Having set up the mathematical structure, let us step back and consider the physical interpretation. We have decomposed the wavefunction into left and right parts, and each of these are separated into incoming and outgoing waves. What we have not emphasized is that  $\psi^L(E)$  and  $\psi^R(E)$  are parts of a single-electron wavefunction. Formally,

$$\psi(E, \vec{r}) = \begin{cases} \psi^L(E), & \forall \vec{r} \in \{L\} \\ \text{unspecified}, & \forall \vec{r} \in \{\text{bridge}\} \\ \psi^R(E), & \forall \vec{r} \in \{R\} \end{cases} \quad (1.7)$$

where  $\vec{r}$  is the position. Although it may appear at first glance that there are multiple wavefunctions

in Eq 1.5, they are part of a single-electron wavefunction which extends across the entire system.

Realizing that there is only a single-electron wavefunction in the entirety of Eq 1.5 immediately implies elastic and coherent tunneling. After all, a single electron wavefunction has only one energy (elastic), is defined everywhere in space (spatial coherence), and has a global phase defined as  $e^{-iEt/\hbar}$  (temporal coherence). How are these ideas expressed in Eq 1.5? Eq 1.5 emphasizes elastic tunneling by specifying the same energy in all terms. Coherence is expressed in the following way: for any incoming wavefunction, the outgoing wavefunction is determined exactly by the scattering matrix. Note that although the energy of the wavefunction must be the same, the decomposition of the outgoing part of the wavefunction does not need to be (and generally is not) the same as that for the incoming part.

To more rigorously derive Eq 1.1 from the scattering matrix formalism requires a subtle shift from wavefunctions to operators (Section 4.7 of Cuevas and Scheer). However, the form of Eq 1.5 does not change and the conclusions from the preceding paragraph hold. The Landauer-Büttiker formalism is still a single-electron model because it assumes that, although there are multiple-electrons, they are non-interacting in the bridge and tunnel independently of one another. The picture of a stationary wavefunction extended throughout the entire system is less useful as the physics becomes more complex, but the definitions of elastic (energy conserving) and coherent (deterministic state evolution) transport will remain valid. Finally, I note briefly that the transmission function is related to the scattering matrix by the following equation [88].

$$T(E) = \text{Tr} \left[ t_{RL}^\dagger(E) t_{RL}(E) \right] \quad (1.8)$$

### 1.3 Inelastic Transport and Incoherence

Having defined elastic and coherent transport, we are now in a position to discuss inelastic and incoherent transport. In this section, I will limit myself to a conceptual description. Figure 1.5 depicts a simple model for inelastic transport in a single-molecule junction. The two electrodes are represented by Fermi distributions with chemical potentials separated by  $eV$ , and the molecule is

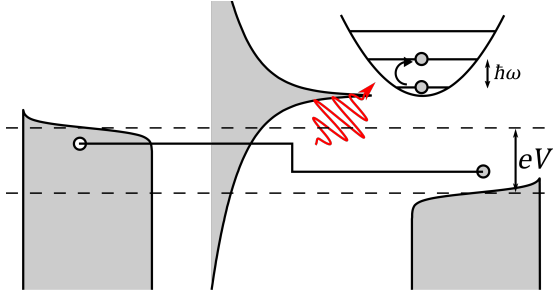


Figure 1.5: Schematic of inelastic transport via coupling to a single vibrational mode.

replaced with the transmission function for a single-level model. On the top-right corner, we show a harmonic potential for a single vibrational mode of the molecule, with multiple states separated by  $\hbar\omega$ , the energy quantum of the mode. The tunneling electron can excite the vibrational states by exchanging energy. At 0 Kelvin, only excitation of the vibrational states is allowed, but at finite temperature, vibrational states besides the ground state will be occupied, allowing for energy absorption as well.

The transport is clearly inelastic because the electron ends with a different energy than it started with, but is it incoherent? In principle, if the states of the phonons are known exactly, then the transport can still be coherent, since the evolution of both electron and phonon states can be specified precisely, at least in theory [91]. In practice, it is challenging to drive the vibrational modes of a molecule coherently and the coherence times are generally on the order of picoseconds or less [92–96]. At room temperature, the problem is exacerbated by the fact that the phonon system is best described as an ensemble of possible states characterized by the temperature; the exact microstate of the phonons is unknown [97]. In both these cases, the end result is that the outgoing electronic wavefunctions are not known exactly but only probabilistically. Therefore, inelastic transport by electron-phonon coupling is generally incoherent, although the degree of incoherence varies [98–101]. By contrast, lasers generate coherent photons and inelastic transport does not necessarily imply incoherence [102, 103].

For single-molecule studies where the molecule is poorly coupled to the leads, the discrete electronic states of the molecule are preserved, and inelastic effects due to coupling to vibrational modes and photons have more pronounced signatures [104–111]. In single-molecule junctions, by

contrast, inelastic and incoherent transport in single-molecule junctions has been chiefly explored in inelastic electron tunneling spectroscopy [98, 112–116] and temperature and length dependent tunneling experiments [117–120]. Only in the last decade have the effects of photons on transport in single-molecule junctions been observed [121–130]. It is the goal of this dissertation to extend our understanding of inelastic and (to a lesser extent) incoherent transport in single-molecule junctions.

Finally, as explored in depth in Section 1.2, the Landauer-Büttiker formalism is not equipped to handle inelastic and/or incoherent transport. For this, more advanced mathematical machinery is required, namely non-equilibrium Green's functions (NEGF). I will briefly recommend some resources. Chapter 5 of Cuevas and Scheer, Chapter 3 of Ref. [131], and Chapter 8 of Ref. [132] all provide an excellent introduction to Green's functions but are insufficient for understanding the literature on inelastic transport. For a better physical intuition, I recommend Refs. [133, 134]. Chapters 6–8 of Cuevas and Scheer and Chapter 8 of Ref. [131] covers all the basic terminology necessary for NEGF in the context of transport in single-molecule junctions. A more comprehensive treatment can be found in Refs. [135–137].

## 1.4 STM Break-Junction Technique

I will utilize the Scanning Tunneling Microscope Break-Junction (STM-BJ) technique to study inelastic transport in both tunnel junctions and single-molecule junctions [13, 138–140]. A diagram of the custom STM used throughout this dissertation is shown in Figure 1.6a and described in detail in Ref. [141]. A bias  $V_0$  with respect to the ground of the Keithley current amplifier (Keithley GND) is applied to the circuit. The circuit is comprised of a resistor  $R$  in series with the tunnel junction. Unless noted otherwise,  $R = 100 \text{ k}\Omega$ . We measure the voltage after the resistor  $V_m$  and the total current  $I$  simultaneously.  $V_m$  is measured with respect to Keithley GND, and the gain of the Keithley current amplifier  $g$  is set to 6 unless noted otherwise. The conductance  $G$  of the tunnel junction is then calculated from the measured voltage and current ( $G = I/V_m$ ).

The top and bottom electrodes are, respectively, a Au wire crimped with cutting pliers and a

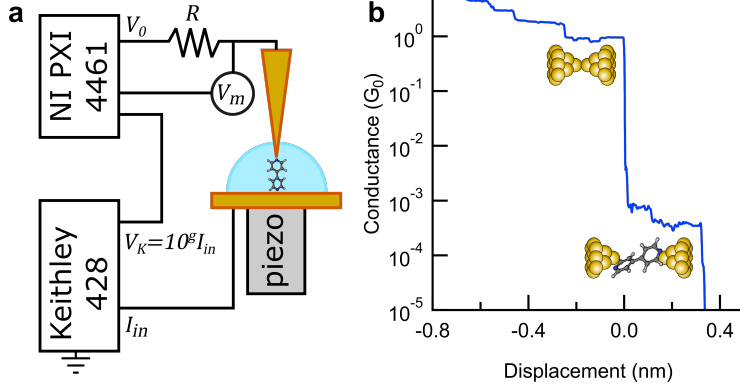


Figure 1.6: (a) Schematic of STM. (b) Single conductance trace of a single-molecule break-junction.

mica substrate with an approximately 100 nm Au layer thermally evaporated on top. The bottom electrode is mounted on a piezoelectric motor (piezo, for short) which provides sub-nanometer control of the substrate position. This is correlated with, but not exactly, the junction gap [66]. The molecules are typically introduced into the junction through a solution with concentration between 10-1000  $\mu\text{M}$ . All measurements in this dissertation are performed at room temperature and in ambient conditions. Throughout the dissertation, slight modifications will be made to the STM, but the basic design will remain unchanged.

The break-junction technique starts with the two electrodes in contact. As the substrate is pulled away from the tip electrode, we measure the conductance at a rate of 40,000 samples per second. Since we move the substrate at a constant speed of approximately 20 nm/s, we can graph the conductance as a function of displacement as shown in Figure 1.6b. A single such measurement is called a conductance trace. The conductance decreases as the substrate is withdrawn, eventually revealing discrete steps. These steps indicate that the conductance is limited by a nanoconstriction formed from a few Au atoms, each atom providing a single channel for transmission [138]. Each individual Au atom in the narrowest part of the junction adds an additional quantum of conductance,  $G_0 = 2e^2/h = 77.48 \mu\text{S}$ . Eventually, the two electrodes are connected by a single Au atom, and the junction has conductance of  $1G_0$ . As the electrodes are pulled further apart, the Au electrodes separate entirely, allowing a single molecule to bridge the gap. This is observed as a plateau below  $1G_0$  in the conductance trace, with different single-molecule junctions displaying

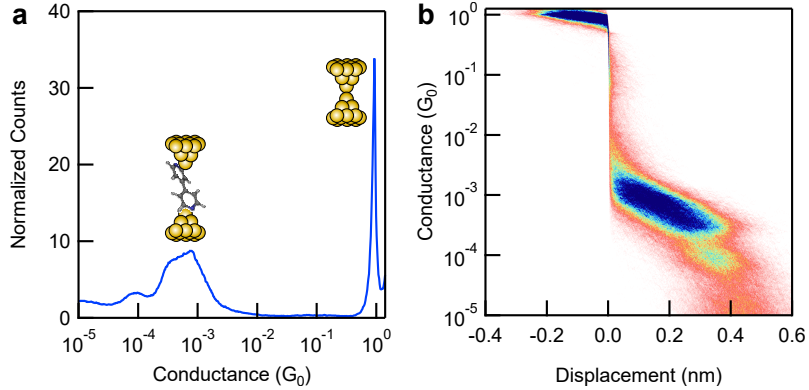


Figure 1.7: (a) 1D conductance histogram and (b) 2D conductance-displacement histogram of 4,4'-bipyridine.

different average conductances. The electrodes continue to be pulled apart until the molecule can no longer bridge the gap and the junction breaks entirely. A single conductance trace summarizes the break-junction technique.

The conductance of a single-molecule junction depends on a number of factors such as the exact binding geometry and the molecular conformation. To measure the variation in conductance, we repeat the measurement hundreds of times in quick succession and compile the results in a one-dimensional (1D) logarithmically-binned conductance histogram. We show one such histogram in Figure 1.7a. The sharp peak at  $1G_0$  represents the single Au atom contact. The molecule measured here (4,4'-bipyridine) shows two conductance peaks at approximately  $10^{-3}$  and  $10^{-4} G_0$  for different binding geometries [29].

Finally, multiple conductance traces can be summarized in the form of two-dimensional (2D) conductance-displacement histograms such as the one in Figure 1.7b [142]. To produce these histograms, the location where the single Au atom contact breaks is set to zero (see Fig 1.6b). The points are then binned according to both displacement relative to the breaking point (linearly binned) and the conductance (logarithmically binned). The 2D conductance-displacement histograms provides a lower bound on the length of the molecule and reveals any correlations between conductance and displacement.

In summary, the STM-BJ technique is a powerful method for simultaneously forming and probing single-molecule junctions. The above only represents one type of measurement, and I will

introduce other experimental designs throughout this dissertation.

## 1.5 Thesis Outline

The remainder of the dissertation is organized as follows:

**Chapter 2** studies the mechanism for electroluminescence in tunnel junctions operated at high voltage. Previous studies have shown that the photons emitted from tunnel junctions can have energy exceeding the classical limit. Various explanations for this phenomenon have been proposed in recent years, including the shape of the Fermi-distributions, multi-electron processes, and blackbody radiation. I measure the electroluminescence using the break-junction methodology and argue that multi-electron processes provide the most comprehensive explanation of the observed phenomena.

**Chapter 3** complements Chapter 2 in that I study light absorption instead of light emission. Specifically, I demonstrate that the conductance of single-molecule junctions can increase by up to 60% under illumination. Importantly, I argue that the mechanism for this enhancement is due to the excitation of non-equilibrium hot-electron distributions in the electrodes and not photon-assisted tunneling.

**Chapter 4** explores the mechanism for junction rupture near the resonant tunneling condition in single-molecule junctions. Surprisingly, we discover that some junctions survive and that these junctions display pronounced negative differential resistance and hysteresis. Existing theories for this phenomenon are not completely consistent with our findings, which suggest that new models are required to understand transport in single-molecule junctions near resonance. We speculate that such theories will likely involve a deeper understanding of the electron-phonon interactions near resonance and mechanisms for incoherent transport.

**Chapter 5** provides a summary and offers an outlook on future directions for this research.

## Chapter 2: Too Cool for Blackbody Radiation

### 2.1 Preface

This chapter is adapted from the manuscript entitled *Too Cool for Blackbody Radiation: Overbias Photon Emission in Ambient STM Due to Multi-Electron Processes*, by E-Dean Fung and Latha Venkataraman. I would like to thank Dimitri Basov and Nanfang Yu for the generous use of their equipment. I would also like to acknowledge Aaron Sternbach, Sajan Shrestha, and Adam Overvig for discussions on implementing photodetection; Arvind Narayanaswamy and Arvind Srinivasan for discussions on blackbody radiation; and Andrew Downes (University of Edinburgh) for clarification of his experimental results.

### 2.2 Introduction

Electroluminescence in tunnel junctions was first observed by Lambe and McCarthy in 1976 [143, 144]. More recently, light emission with photon energies exceeding the energy of tunneling electrons, so-called overbias emission, was observed, prompting a series of experimental and theoretical papers to explain the phenomena [145]. The candidate explanations include the shape of the Fermi distribution at elevated electron temperatures [145, 146], multi-electron processes [147–153], and blackbody radiation [154–158]. Multi-electron processes are particularly interesting from a technological standpoint because they offer a route to nanoscale electro-optical transducers with low operating voltage and broadband emission spectra [159]. However, photon emission from multi-electron processes has only been demonstrated at low temperatures, which limits its use in devices, and studies at room temperature indicate that overbias emission is due to blackbody radiation or the shape of the Fermi distribution.

In this study, we measure the light emission as a function of conductance in a custom scanning

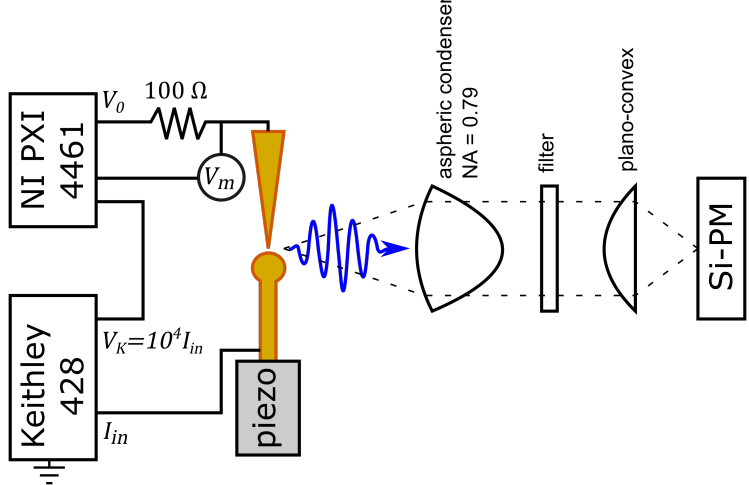


Figure 2.1: Schematic of STM modified for light detection.

tunneling microscope (STM) operating at room temperature and ambient conditions. We demonstrate that the overbias emission is due to a mixture of single- and multi-electron processes and that the phenomenon is remarkably robust to water in the tunnel junction. Finally, we show that these observations are incompatible with blackbody radiation and argue that multi-electron processes explain previous results that were attributed to blackbody radiation.

### 2.3 Experimental Methods

Previous measurements of overbias emission at room temperature characterized only a few tunnel junctions. Here, we apply the break-junction technique in a custom STM and simultaneously measure the light emission and conductance of thousands of junctions by repeatedly forming and breaking contact between two Au electrodes [140, 160]. The break-junction method complements previous experiments in that we sample a larger variety of electrode geometries.

Figure 2.1 is a schematic of the modified STM. The configuration of the STM in this chapter differs from the configuration presented in Section 1.4 in a number of ways. First, we use a  $100\ \Omega$  resistor instead of a  $100\text{ k}\Omega$  resistor in series with the tunnel junction and operate at gain 4. We use a smaller series resistor so that 99% of the applied bias drops across the junction, even for junction conductances of  $1G_0$ . A series resistor is still required to avoid overloading the current

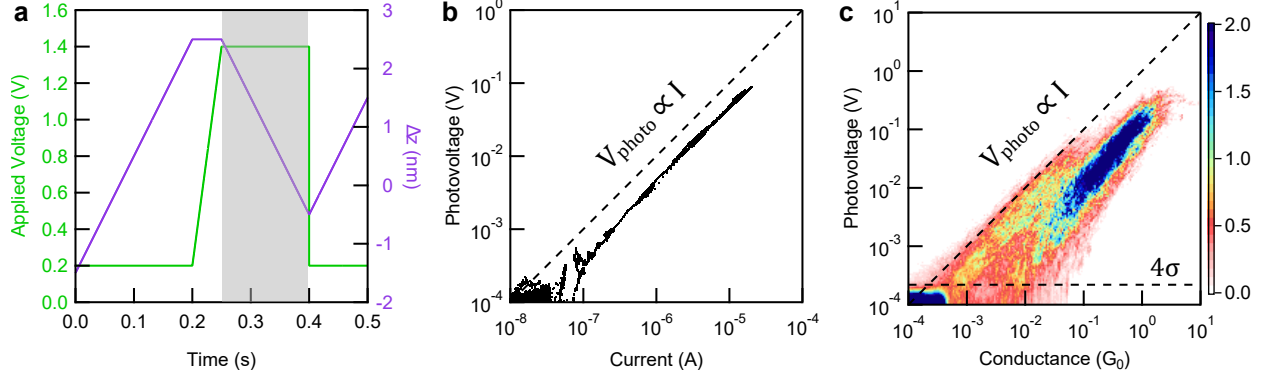


Figure 2.2: (a) Applied bias (green) and idealized junction gap (purple) as a function of time. (b) Example trace of photovoltage and current data from the high bias push section (highlighted area in (a)). (c) 2D photovoltage-conductance histogram of 1000 traces without data selection for the high bias push section. Horizontal dashed line indicates  $4\sigma$  of noise.

amplifier at gain 4. Second, we use a spherical Au single crystal formed by melting 0.25  $\mu\text{m}$  diameter Au wire as the bottom electrode. Finally, light from the junction is collected by a 0.79 NA aspheric condenser lens (Thorlabs) and focused onto a Silicon Photomultiplier (Excelitas) by a plano-convex lens. The spectral dependence of the emission is obtained by inserting bandpass filters into the optical path.

The break-junction measurements are carried out while controlling two parameters: the voltage applied to the circuit and the electrode separation, as illustrated in Figure 2.2a. The experiment starts by pulling the electrodes apart, which are initially in contact; this forms the tunnel junction. The voltage is then increased and the tips are pushed together, sometimes making contact again. Finally, the tips are pulled apart at a low voltage to reset the experiment. The electrode separation depicted in Figure 2.2a is the ideal case. The actual electrode separation deviates from junction to junction due to the instability of the junction at room temperature and high voltage.

During each measurement, we record the electroluminescence (measured as a photovoltage from the Silicon photomultiplier) and the current simultaneously, collected at an acquisition rate of 100 kHz. Figure 2.2b shows the measured photovoltage and current for a single tunnel junction collected during the segment when a high bias is applied (shaded area in Fig 2.2a). We apply an 101-point boxcar smoothing to both the photovoltage and current to help distinguish signal from noise. The experiment is repeated 1000 times, and we visualize the data in a 2D photovoltage-

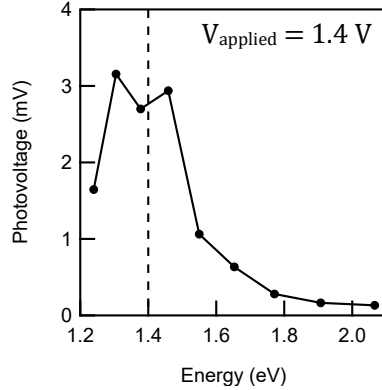


Figure 2.3: Spectrum collected using bandpass filters, representing emission of a junction with a bias of 1.4 V and conductance of  $\sim 1G_0$ . Threshold between underbias and overbias emission delineated by the vertical dashed line.

conductance histogram shown in Figure 2.2c. Figure 2.2c immediately reveals the presence of two types of junctions: junctions with higher photon emission efficiency but lower conductance ( $10^{-3}$ - $10^{-1} G_0$ ) and junctions with lower efficiency but higher conductance ( $10^{-2}$ - $10^0 G_0$ ). We hypothesize that the lower conducting tunnel junctions are pristine. As the distance between the electrodes decreases and the conductance increases, the electric field strength increases which draws in water from the environment [161, 162]. Boyle and coworkers showed that water in the junction decreases the light emission efficiency, consistent with what is observed here [163].

We repeat the experiment with bandpass filters of different wavelengths to collect the emission spectrum. The average photovoltage around  $1G_0$  is extracted from each dataset and plotted as a function of photon energy, shown in Figure 2.3. We clearly observe emission at photon energies below the energy supplied by the bias (underbias emission) and emission up to 0.4 eV above this classical cutoff energy (overbias emission).

## 2.4 Multi-Electron Processes

Having demonstrated the capability to measure overbias emission, we now review the three theories that can be used to understand the results. Figure 2.4a depicts a single electron tunneling inelastically through the junction, emitting a photon in the process. Such an event can produce some overbias emission because the thermal energy broadens the Fermi distributions of the two

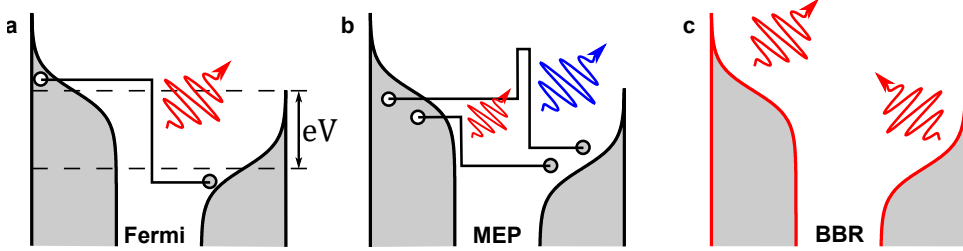


Figure 2.4: Illustration of mechanisms for overbias emission from (a) temperature-broadened Fermi distribution, (b) multi-electron processes, and (c) blackbody radiation.

electrodes. Figure 2.4b depicts a multi-electron process involving two electrons that interact to produce overbias emission. Finally, Figure 2.4c emphasizes that the tunneling electrons are not directly involved in the emission of blackbody radiation. They serve only to increase the effective electronic temperature of the electrodes.

Focusing first on single electron tunneling, a slightly more nuanced interpretation of emission from tunneling electrons views the STM tip as a plasmonic antenna [164, 165]. Driving the antenna requires a time-dependent forcing function, which is provided by quantum noise in the current. The energy-dependent probability density of emission  $P(E)$  takes the form

$$P_{1e}(E) = D(E)S(E) \quad (2.1)$$

$S(E)$  is the current noise power spectral density, which provides the driving force, and  $D(E)$  is the response of the plasmonic antenna. The subscript on  $P(E)$  emphasizes that this only accounts for single-electron processes. As has been discussed previously, it is the unsymmetrized noise and not the symmetrized noise which produces photon emission [166–168]. The canonical sources describing the frequency dependent current noise do not apply [169, 170], and instead the lowest-order current noise is given by [149, 171, 172]

$$S(E) = \sum_n \left[ 2\tau_n^2 B(E) + \tau_n(1 - \tau_n) \sum_{\pm} B(E \pm eV) \right] \quad (2.2)$$

where  $B(E) = E / [e^{E/k_B T} - 1]$  and  $\tau_n$  is the transmission coefficient for each transport channel enumerated by  $n$ . The transport channels are assumed to be non-interacting and energy-

independent. The effect of the Fermi-distributions of the electrodes is encoded in  $B(E)$ , so Eq 2.1 includes the effect depicted in Figure 2.4a. Here, we have normalized the units in  $D(E)$  and  $S(E)$  to the quantum of conductance (see Section 2.7.2).

Eq 2.1 only accounts for emission from a single electron. A closed-form solution for the two-electron emission at finite temperatures was derived by Xu *et al.* [147, 148, 153]. Below, we present an extension of their low temperature approximation, which we show is in excellent quantitative agreement with the full theory (see Fig 2.11).

$$P_{2e}(E) = D(E) \int_0^{\infty} d\varepsilon D(\varepsilon)S(\varepsilon)S(E - \varepsilon)H(E - \varepsilon) \quad (2.3)$$

Eq 2.3 models the multi-electron process illustrated in Figure 2.4b.  $\varepsilon$  is the photon energy emitted by the first electron. Interaction with a second electron with energy  $E - \varepsilon$  produces a photon with overall energy  $E$ . The limits of integration and the Heaviside step function  $H(E)$  guarantee that only photon emission processes are considered and not photon absorption.

In Figure 2.5a, we calculate the theoretical room temperature spectrum using Eq 2.1-2.3. The theoretical spectrum, which we denote  $p(E)$ , is related to  $P(E)$  by the equation  $p(E) = Q(E)P(E)$ , where  $Q(E)$  models the quantum efficiency of the detector. To produce Figure 2.5a, we use a single electronic channel with a transmission coefficient of 0.1, an applied bias of 1.4 V, and a featureless electromagnetic environment (i.e. no plasmonic wavelength dependent enhancements, with  $D(E) = 0.1 \text{ eV}^{-2}$ ). At room temperature,  $p_{1e}$  extends approximately 0.2 eV above the classical cutoff due to the broadened Fermi-distributions. The vertical line in Figure 2.5a delineates the underbias emission from the overbias emission. This is conceptually distinct from  $p_{1e}$  and  $p_{2e}$ , which are defined by the number of electrons contributing to the emission of a single photon. Figure 2.5a emphasizes that  $p_{1e}$  and  $p_{2e}$  each generate both underbias and overbias emission.

We can integrate the theoretical spectra  $p_{1e}$  and  $p_{2e}$  over the underbias and overbias regimes. By performing this integration numerically for different junction conductances, we obtain Figure 2.5b. The single-electron (1e) emission increases linearly with conductance for both underbias and overbias emission when  $G \ll G_0$ . As the conductance approaches  $G_0$ , the emission becomes

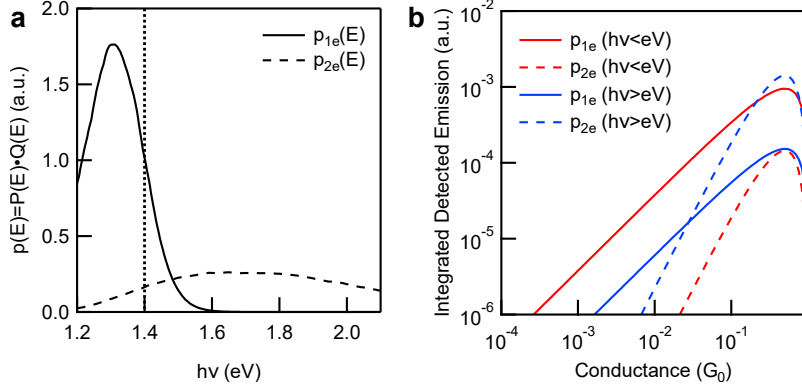


Figure 2.5: (a) Calculated spectrum ( $p(E) = Q(E)P(E)$ ), where  $Q(E)$  is the quantum efficiency of the detector) for an applied bias of 1.4 V (vertical dotted line). One-electron (1e) and two-electron (2e) contributions in solid and dashed lines, respectively. Parameters:  $D(E) = 0.1 \text{ eV}^{-2}$ ,  $\tau = 0.1$ ,  $T = 300 \text{ K}$ ,  $V_{\text{applied}} = 1.4 \text{ V}$ . (b) 1e (solid) and 2e (dashed) calculated spectrum as a function of conductance (obtained by varying  $\tau$ ), integrated over underbias (red) and overbias (blue) photon energies.

sublinear and eventually decreases with increasing conductance. This implies that single-electron emission cannot produce a superlinear dependence of emission on conductance even including the shape of the Fermi-distribution at room temperature. The two-electron (2e) emission, by contrast, increases quadratically for low conductances. If we describe the emission by the power law  $p \propto G^\beta$ , then a superlinear relation ( $\beta > 1$ ) is a strong indication of multi-electron processes.

The superlinear dependence of overbias emission on conductance was first observed by Schull and coworkers at low temperature, but the effect has not been reproduced at room temperature [150]. By using longpass and shortpass filters, we investigate this phenomenon at room temperature for the underbias and overbias emission, respectively. Figure 2.6a,b shows the 2D photovoltage-conductance histograms for experiments performed with longpass and shortpass filters, respectively. With a shortpass filter, the photovoltage only exceeds noise when the conductance is above  $10^{-2}G_0$ . In this conductance range, only tunnel junctions with water are present. We clearly observe a superlinear dependence on conductance in Figure 2.6b. More quantitatively, the underbias emission is close to linear ( $V_{\text{photo}} \propto G^{1.05}$ ), whereas the overbias emission follows a superlinear relation ( $V_{\text{photo}} \propto G^{1.35}$ ).

To explain the deviation from  $\beta = 2$  predicted by the 2e emission model, we calculate the

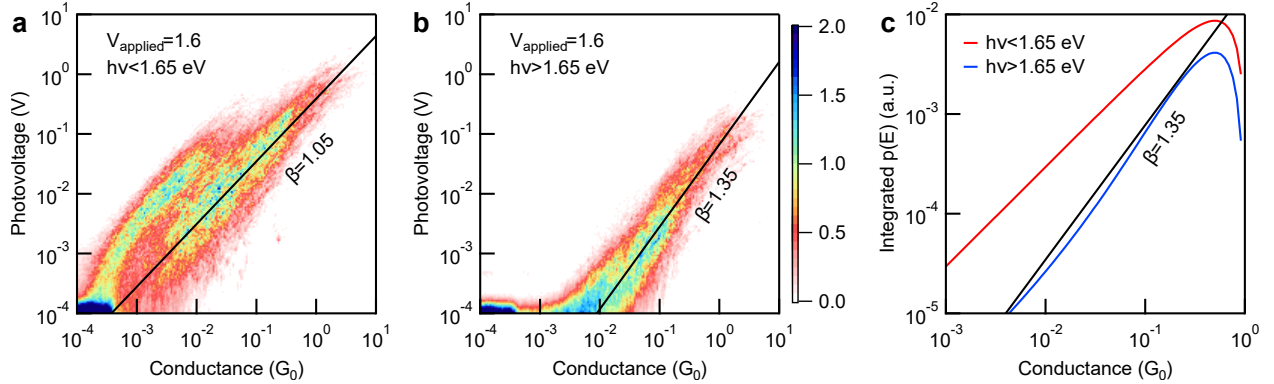


Figure 2.6: 2D photovoltage-conductance histograms of the (a) underbias and (b) overbias emission with the mean fitted power law overlaid in black. (c) Integrated spectrum calculated as a function of conductance, simulating (a) and (b). Parameters:  $D(E) = 0.1 \text{ eV}^{-2}$ ,  $T = 500 \text{ K}$ ,  $V_{\text{applied}} = 1.6 \text{ V}$ .

total spectrum as a function of conductance and integrate over the underbias and overbias regimes without separating the 1e and 2e contributions. The results are shown in Figure 2.6c, where the blue curve reproduces the  $\beta = 1.35$  observed in the overbias emission. Although 2e emission predicts  $\beta = 2$ , the 1e emission contributes significantly to the overbias emission at room temperature, which decreases  $\beta$  (see Fig 2.5a). Importantly, to obtain  $\beta = 1.35$ , we had to assume an electronic temperature increase to 500 K. This temperature increase of 200 K is also consistent with the  $\beta = 1.7$  measured by Schull *et al.* (see Fig 2.14b) [150]. Importantly, the mixing between 1e and 2e emission also explains the slightly superlinear dependence of underbias emission, which has been consistently observed in previous experiments [146, 150].

## 2.5 Blackbody Radiation

Thus far, we have only considered overbias light emission from single- and multi-electron processes. However, we claim that these phenomena are incompatible with the theory of overbias emission from blackbody radiation, which we now summarize. The dependence of blackbody radiation on electrical power was obtained in previous works by introducing the Tomchuk and

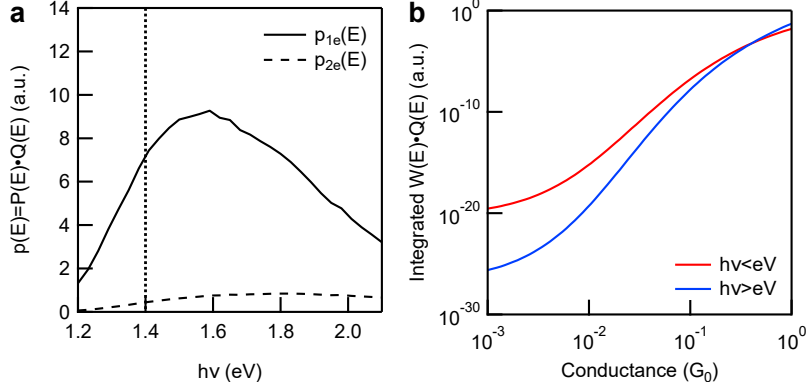


Figure 2.7: (a) Same as Fig 2.5a except with  $T = 2000$  K. (b) Theoretical blackbody radiation integrated over the underbias (red) and overbias (blue) regimes as a function of conductance, analogous to Fig 2.6c. We use Eq 2.5 instead of the approximation and use the vacuum density of photon states. Theoretical blackbody radiation includes the quantum efficiency of a detector. We use  $\alpha = 10^{-17}$  eV s.

Fedorovich model relating electrical power and the electronic temperature [173].

$$(k_B T_e)^2 - (k_B T_L)^2 = \alpha IV \quad (2.4)$$

Here,  $T_e$  is the electronic temperature,  $T_L$  is the temperature of the lattice, and  $\alpha$  depends on material properties of the metal electrodes [155]. The radiated power from blackbody radiation  $W_{BBR}$  as a function of photon energy is given by [97]

$$W_{BBR}(E) \propto \rho(E)B(E, T_e) \quad (2.5)$$

where  $\rho(E)$  is the local density of photon states. This accounts for the localized surface plasmon resonances similar to  $D(E)$  in Eq 2.1 and 2.3. In the limit that  $T_e \gg T_L$  and  $E \gg k_B T_e$ , Eq 2.5 can be approximated as  $\ln(W_{BBR}(E)) \propto (-\alpha IV)^{-0.5}$ , which gives the dependence on electrical power.

The approximate form of Eq 2.5 was observed independently by three groups, from which electronic temperatures of at least 2000 K were inferred [154–156]. In Figure 2.7a, we plot the effect of such high electronic temperatures on emission from multi-electron processes (compare with Fig 2.5a). At these temperatures, the 1e emission  $p_{1e}$  effectively dominates at all wavelengths

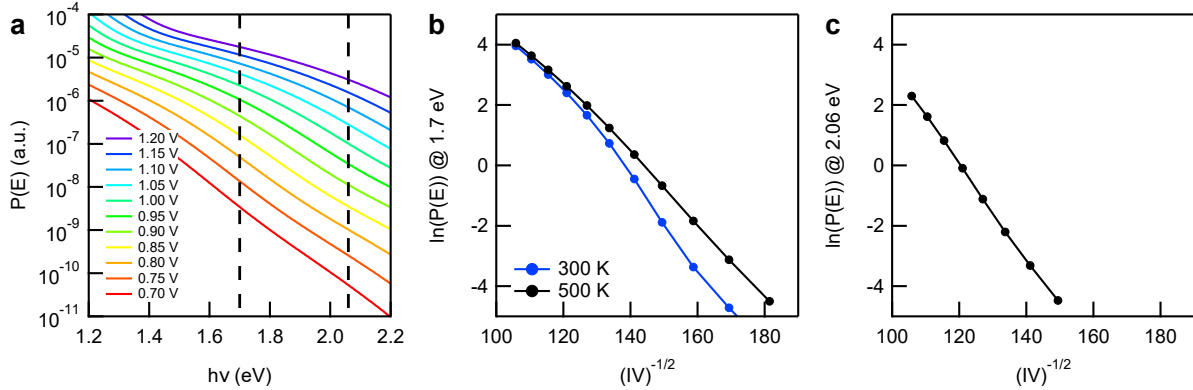


Figure 2.8: (a) Calculated total emission spectra  $P(E) = P_{1e} + P_{2e} + P_{3e}$  for different applied voltage. Parameters:  $D(E) = 0.1 \text{ eV}^{-2}$ ,  $\tau = 0.8$ ,  $T = 500 \text{ K}$ . Vertical dashed lines at  $\hbar\omega = 1.7$  and  $2.06 \text{ eV}$  correspond to data used to produce (b) and (c), respectively. (b) also includes the same calculation but at room temperature in blue. Note the vertical axis is the natural log. All curves in (b) and (c) are vertically shifted by the same amount to mimic values in Fig 4 of Ref. [155].

due to the substantial broadening of the Fermi-distributions, and the superlinear dependence on conductance from 2e emission disappears. Furthermore, blackbody radiation cannot explain the observed conductance dependence. In Figure 2.7b, we calculate the spectrum from blackbody radiation (i.e.  $Q(E)W(E)$ ) as a function of conductance integrated over the underbias and overbias regimes (compare with Fig 2.6c). Although blackbody radiation does predict superlinear dependence, the power law predicted is far too extreme to be reconciled with our data. In addition, it predicts superlinear dependence in both the underbias and overbias emission, contradicting our results. Together, parts a and b of Figure 2.7 demonstrate the observed superlinear conductance dependence in emission is only explained by multi-electron processes, and that this explanation is not compatible with the temperatures required by blackbody radiation.

By contrast, the predictions of blackbody radiation can be explained by emission from multi-electron processes. Specifically, we reproduce results in Refs. [155] and [154] that show  $\ln(W) \propto (IV)^{-0.5}$ . In Figure 2.8a, we plot the total emission probability density  $P(E)$  including emission up to three-electron processes for a range of biases, using parameters corresponding to Ref. [155]. The different spectra are roughly evenly spaced on a semi-log plot. By taking values at two different photon energies, we reproduce Figure 4 of Ref. [155] in Figure 2.8b,c. Note that without assuming a temperature increase of 200 K, the trend deviates from  $\ln(W) \propto (IV)^{-0.5}$ .

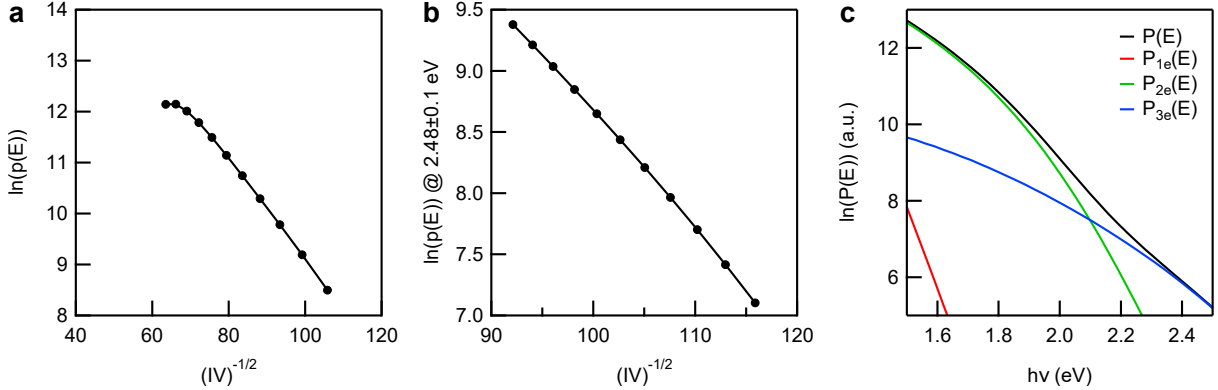


Figure 2.9: (a) Spectrum  $p(E)$  integrated across all wavelengths for voltages between 1.2 and 2.0 V, plotted against  $(IV)^{-0.5}$ . Compare with Fig 2b of Ref. [154]. Parameters:  $D(E) = 0.1 \text{ eV}^{-2}$ ,  $\tau = 0.7-0.95$ ,  $T = 500 \text{ K}$ . (b) Spectrum  $p(E)$  integrated between 2.38-2.58 eV for voltages between 1.55 and 1.95 V, plotted against  $(IV)^{-0.5}$ . Compare with Fig 7.13 of Ref. [175]. Parameters:  $D(E) = 0.1 \text{ eV}^{-2}$ ,  $\tau = 0.4$ ,  $T = 500 \text{ K}$ . (c) Total emission (black) as a function of photon energy, with contributions from 1e, 2e, and 3e processes in red, green, and blue, respectively. Compare with Fig 3 of Ref. [154]. Parameters:  $D(E) = 0.1 \text{ eV}^{-2}$ ,  $\tau = 1.3$ ,  $T = 500 \text{ K}$ ,  $V_{\text{applied}} = 1.0 \text{ V}$ . All curves vertically shifted to mimic published results.

Next, we reproduce Figure 2b from Ref. [154], which we will refer to as Downes 2002. This calculation is slightly more involved. First, Figure 2b in Downes 2002 is the detected photon rate, not the emitted photon rate [174]. Second, the detected photons are over a broad range of frequencies, dictated by the quantum efficiency of the detector used. This is provided in Figure 4.9 of Ref. [175]. Third, close inspection of Figure 2a in Downes 2002 shows that the conductance and the applied voltage are correlated. At room temperature, the large electric fields can cause the Au atoms to shift closer together, increasing the conductance. By assuming a linear relationship between conductance and voltage, we qualitatively reproduce Figure 2b in Downes 2002 in Figure 2.9a using the multi-electron process model.

Downes *et al.* also repeated the measurement with a bandpass filter. This is provided in Figure 7.13 of Ref. [175]. Assuming a fixed conductance of  $0.4G_0$  is sufficient to reproduce the trend. Figure 2.9b shows the results from our calculation, in excellent agreement with their measurement.

At fixed bias, the emission predicted by blackbody radiation is approximately exponential for  $E \gg k_B T$ , as depicted in Figure 3 of Downes 2002. This, too, can be reproduced by emission from multi-electron processes. In Figure 2.9c, we calculate the emission spectra at fixed bias using

the parameters in Ref. [154]. If we assume again an elevated electronic temperature of 500 K, the total emission spectra is roughly exponential. These comparisons indicate that the results of Refs. [155] and [154] can be explained without having to invoke extreme electronic temperatures.

## 2.6 Conclusions

In summary, we experimentally demonstrate, for the first time, the superlinear dependence of overbias emission on conductance predicted by multi-electron processes at room temperature and ambient conditions. Although the power law for different multi-electron processes has been described before, we highlight that the mixing of processes of different order in both the underbias and overbias emission must be considered to explain both our data and past experiments. In particular, the power law of the overbias emission implies an increase of electronic temperature of approximately 200 K. We argue that blackbody radiation cannot account for the observed power law dependence, whereas multi-electron processes can produce blackbody-like phenomena at room temperature. This strongly refutes the claim of ultra-high electronic temperatures in tunnel junctions driven at high voltage. Finally, although the emission efficiency is relatively low for free-space photons, it was shown that the efficiency of generating surface plasmons is on the order of  $\sim 10\%$  [159]. Thus, this work provides a route for electrically generating high-energy surface plasmons beyond the classical limit.

## 2.7 Supplementary Information

### 2.7.1 Data Analysis Methods

Before any analysis, we subtract the average background signal in the photovoltage and apply an 101 point boxcar smoothing (rolling average) to help distinguish signal from noise. The width of the moving average is justified by considering the length and time scales of the relevant physics. We are interested in the dependence on the log-conductance, which depends linearly on the displacement. We are only interested in angstrom-scale displacements as opposed to sub-angstrom

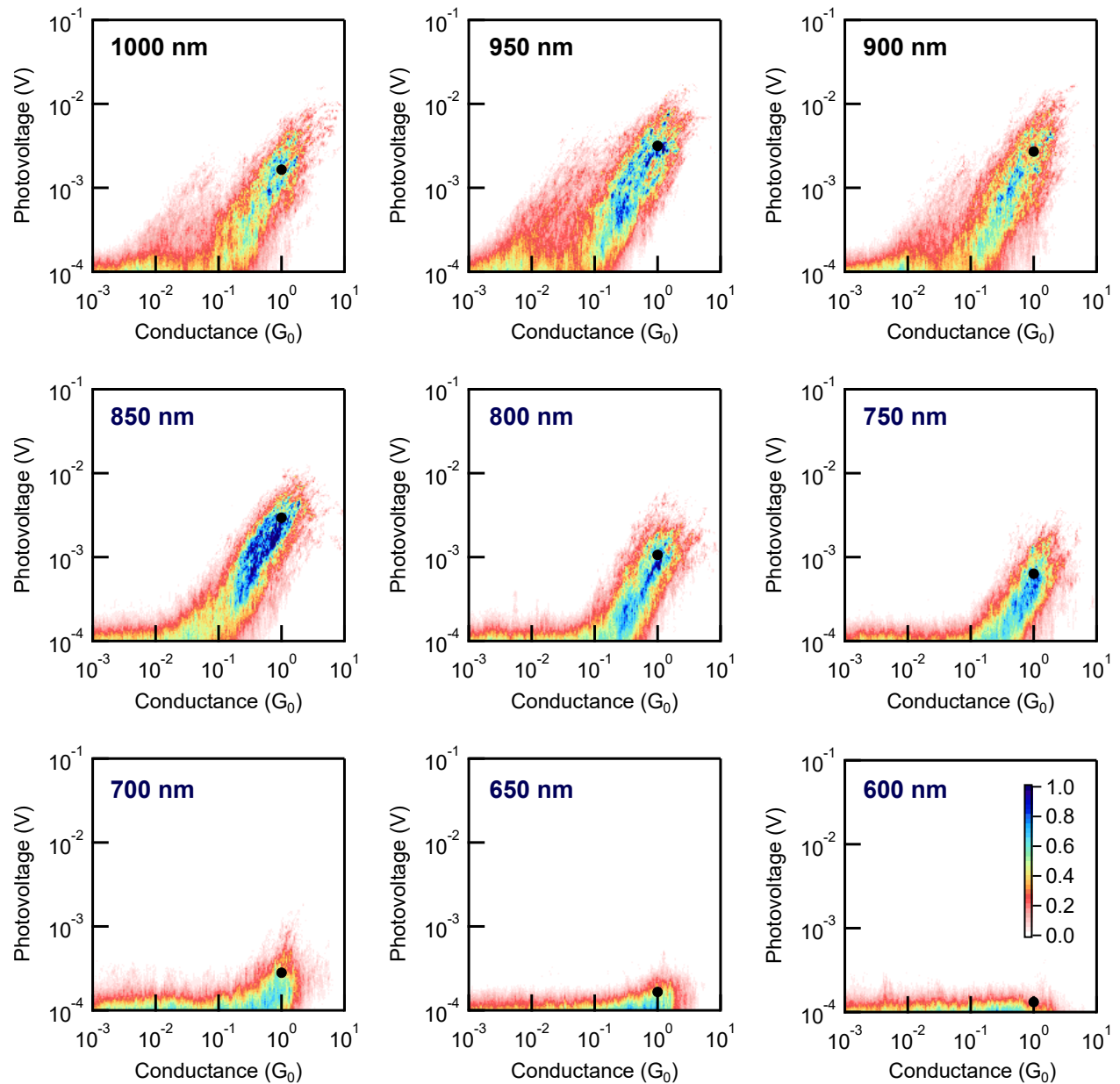


Figure 2.10: 2D photovoltage-conductance histograms for measurements performed with different bandpass filters. The black dots in each histogram correspond to the points in Figure 2.3.

thermal fluctuations. Our push rate is approximately 20 nm/s. With an acquisition rate of 100 kHz, this angstrom-scale displacement correspond to 500 points. The width of our moving average is well within this limit.

The 2D photovoltage-conductance histograms are constructed from the smoothed data during the segment when a high bias is applied (shaded region in Fig 2.2a). Some traces will not display electroluminescence in this region because either the efficiency or conductance is low. Unless noted otherwise, the 2D histograms are constructed without selection.

Depending on the experiment, there are between 15,000 to 30,000 points during the high bias hold. Hence, a  $4\sigma$  event, corresponding to approximately 1 in 30,000 events, is a reasonable threshold to separate signal from noise.

The spectrum in Figure 2.3 was produced by collecting 1000 traces at each wavelength window (600-1000 nm, 50 nm spacing, 10 nm FWHM). For each trace, we calculate the mean photovoltage of the points that are (A)  $4\sigma$  above noise and (B) between  $0.9G_0$  and  $1.1G_0$ . Finally, we average the mean photovoltage of each trace, ignoring traces that do not show any signal, to generate a representative photovoltage at each wavelength.

Figure 2.10 shows the 2D photovoltage-conductance histograms for the nine different wavelengths measured. The black dot in each histogram is the representative photovoltage extracted by the algorithm above and depicted in Figure 2.3.

### 2.7.2 Coulomb Blockade Model

This section is organized as follows: We begin by simply restating our model to emphasize the physical units. We then relate it to the models developed by Tobiska and coworkers [172] and Xu and coworkers [147, 148], which we will refer to as the Tobiska model and Xu model, respectively. Finally, we will compare our model numerically to the Xu model.

The emission probability density,  $P(E)$ , is the probability of emitting a photon with energy in the interval  $[E, E + dE]$  and has units of inverse energy ( $\text{eV}^{-1}$ ). This is the sum of single and multi-electron processes:

$$P(E) = P_{1e}(E) + P_{2e}(E) + P_{3e}(E) \quad (2.6a)$$

$$P_{1e} = G_0 \tilde{D}(E) \tilde{S}(E) \quad (2.6b)$$

$$P_{2e} = G_0^2 \tilde{D}(E) \int_0^\infty d\varepsilon \tilde{D}(\varepsilon) \tilde{S}(\varepsilon) \cdot \tilde{S}(E - \varepsilon) H(E - \varepsilon) \quad (2.6c)$$

$$P_{3e} = G_0^3 \tilde{D}(E) \int_0^\infty d\varepsilon \tilde{D}(\varepsilon) \tilde{S}(\varepsilon) \int_0^\infty d\varepsilon' \tilde{D}(\varepsilon') \tilde{S}(\varepsilon') \cdot \tilde{S}(E - \varepsilon - \varepsilon') H(E - \varepsilon - \varepsilon') \quad (2.6d)$$

We use the tilde to denote the non-normalized versions of  $D(E)$  and  $S(E)$ , which are:

$$\tilde{S}(E) = G_0 \sum_n \left[ 2\tau_n^2 B(E) + \tau_n(1 - \tau_n) \sum_{\pm} B(E \pm eV) \right] \quad (2.7a)$$

$$\tilde{D}(E) = \frac{|\tilde{Z}(E)|^2}{E^2} \quad (2.7b)$$

$\tilde{Z}(E)$  is the complex impedance of the electromagnetic environment. This is typically modelled with an effective RLC circuit. To obtain the normalized version, we absorb two factors of  $G_0$  into  $\tilde{D}(E)$ . The normalized  $D(E)$  is then defined as

$$D(E) = G_0^2 \tilde{D}(E) = \frac{|Z(E)|^2}{E^2} \quad (2.8)$$

where  $Z(E)$  is now the impedance normalized to the quantum of resistance i.e  $Z(E) \equiv G_0 \tilde{Z}(E)$ .

The Tobiska model [172] and Xu model [147, 148] have an additional prefactor of  $\frac{|\mathcal{T}|^2}{h} \alpha^2$ , where  $\mathcal{T}$  is the coupling between the two states of a quantum dot and  $\alpha$  is the dimensionless coupling between the RLC circuit and the detector. This gives the emission rate with units of  $\text{s}^{-1}$ . We do not use a two-state quantum dot as a detector, so more generally, one can replace the constant  $\mathcal{T}$  with  $\mathcal{T}(E)$ . We replace the entire prefactor  $\frac{|\mathcal{T}|^2}{h} \alpha^2$  with  $Q(E)$ , for simplicity.

Both Tobiska and Xu provide a low temperature approximation for the two-electron process. However, this approximation is only valid between  $1eV_{\text{applied}}$  and  $2eV_{\text{applied}}$ , i.e. the energy range where the two-electron emission dominates. As explained in Section 2.4 and discussed in Ref.

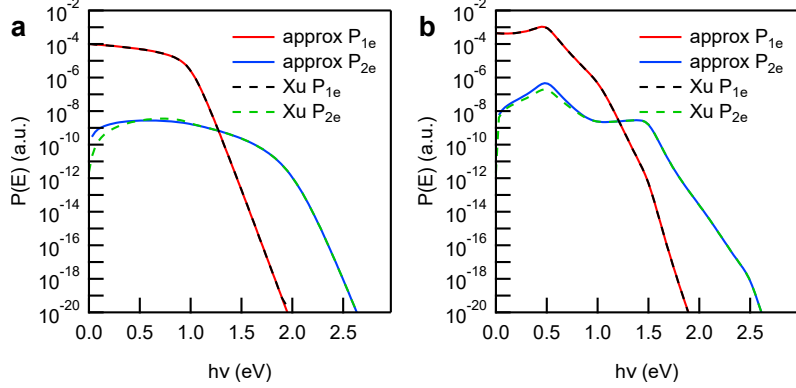


Figure 2.11:  $P_{1e}$  and  $P_{2e}$  calculated from our approximate model (red and blue, respectively) and the Xu model (black and green, respectively). (a) Using a featureless  $D(E) = 0.1 \text{ eV}^{-2}$ . (b) Using three resonances as described in the Xu model, with resonances at 0.5 eV, 1.5 eV and 2.5 eV and an effective broadening  $\eta$  of 0.2 eV for all three resonances. Other parameters:  $\tau = 10^{-3}$ ,  $T = 300 \text{ K}$ ,  $V_{\text{applied}} = 1.0 \text{ V}$ .

[148], there is significant mixing between processes of different orders at room temperature, which this approximation cannot capture. Rewriting the low temperature approximation using our notation and including the three-electron process from Peters *et al.*, we obtain [153]:

$$P_{1e} = G_0 D(E) S(E) \quad (2.9a)$$

$$P_{2e} = G_0^2 D(E) \int_{E-eV}^{eV} d\varepsilon D(\varepsilon) s(\varepsilon) \cdot s(E-\varepsilon) \quad (2.9b)$$

$$P_{3e} = G_0^3 D(E) \int_{E-2eV}^{eV} d\varepsilon D(\varepsilon) s(\varepsilon) \int_{E-eV-\varepsilon}^{eV} d\varepsilon' D(\varepsilon') s(\varepsilon') \cdot s(E-\varepsilon-\varepsilon') \quad (2.9c)$$

Note that the current noise in the two- and three-electron process is not the full expression, but  $s(E) = (eV - E) \sum_n \tau_n (1 - \tau_n)$ .

An analytical expression for the two-electron process at finite temperature was developed by Xu *et al.* However, we required in this work the three-electron process for comparison with the blackbody work. To achieve this, we simply extended the low temperature approximations above by using the full current noise expression, adjusting the limits of integration, and including a Heaviside function. This can be extended to  $n$  electrons: Each additional electron introduces an additional operator  $\int d\varepsilon_i D(\varepsilon_i) S(\varepsilon_i)$ , and the final electron energy becomes  $E - \sum_i \varepsilon_i$ . This last electron directly emits a total energy  $E$ , which is why the final factor of  $D(E)$  is outside the

integral.

In Figure 2.11, we compare our extended numerical approximation to the full analytical expression developed by Xu and coworkers. In Figure 2.11a, we simply use a featureless  $D(E) = 0.1 \text{ eV}^{-2}$ . Since the complex and real parts of  $Z$  enter into the Xu model, we plot the result when  $Z(E)$  is purely imaginary to correspond to the off-resonant case when a featureless  $D(E)$  is a reasonable approximation. Our model is in excellent agreement with the Xu model, with some deviation below 1.0 eV. We also compare the two models for a  $D(E)$  with three resonances at 0.5, 1.5 and 2.5 eV. Again, we observe deviations below 1.0 eV. Since these calculations were done with a junction bias of 1 V, this simply means that our approximation is not valid in the underbias emission regime. But as the two-electron process only produces a small correction to the overall emission, our approximation should be sufficient for the purposes of this work.

### 2.7.3 Variability in $\beta$

To characterize the variability between tunnel junctions, we fit the data from junctions that show clear emission to a power law, i.e.  $V_{\text{photo}} \propto G^\beta$ . As explained in Section 2.3, there are two types of junctions measured: higher efficiency junctions that we hypothesize are pristine tunnel junctions, and lower efficiency but higher conducting junctions that we hypothesize contain a water bridge. Only the second junction is visible with a lowpass filter. Since there is some overlap between the conductances of the two types of junctions (see Fig 2.2c), we only fit points with conductances between 0.1 and  $10G_0$ . This means we only consider water tunnel junctions. We also ignore points  $4\sigma$  below noise when fitting.

Figure 2.12a shows histograms of the fitted  $\beta$  values for the data presented in Figure 2.6a,b. Surprisingly, there is considerable variability in  $\beta$  for both the underbias and overbias emission. To demonstrate the repeatability of the superlinear relation between emission and conductance in the overbias regime, we repeat the experiment with two different tips at two different biases (Fig 2.12b,c). The shift in mean fitted  $\beta$  between the underbias and overbias emission is comparable in all cases. The inability to obtain a  $\beta$  approaching 2 even when the shortpass filter cutoff energy is

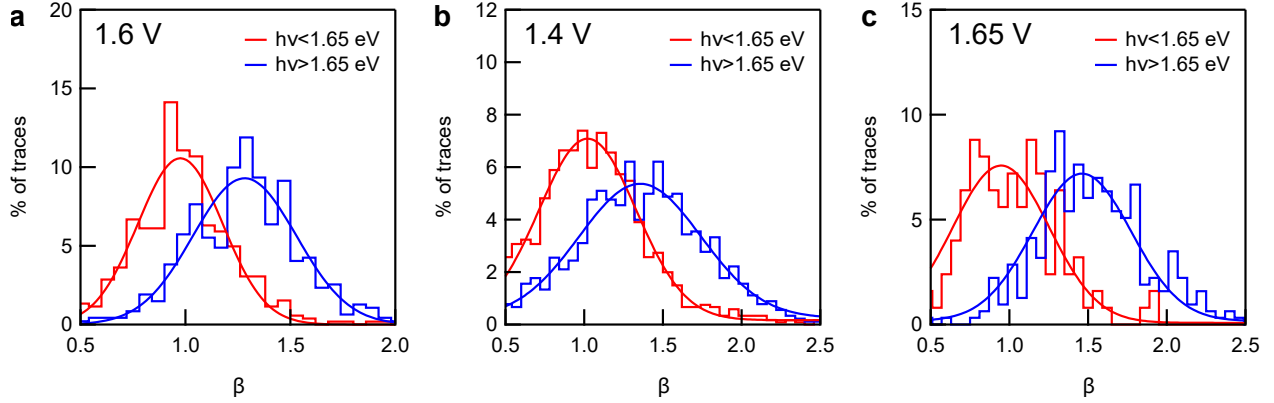


Figure 2.12: Histograms of fitted  $\beta$  for three separate tips with applied bias of (a) 1.6, (b) 1.4, and (c) 1.65 V.

higher than the energy supplied bias the bias is likely a limitation of the sensitivity of the detector.

To show that this variance is not due to the water in the junction, we perform experiments with a  $2\text{k}\Omega$  resistor in series with the tunnel junction. This lowers the bias across the tunnel junction at high conductance where water tunnel junctions are prevalent. Figure 2.13a shows the 2D photovoltage-conductance histogram of this experiment, with light emission detected only for pristine tunnel junctions. Figure 2.13b is the corresponding histogram for the fitted  $\beta$ . We observe a similar variance as with experiments performed with a  $100\Omega$  resistor. This means that the variance is not a feature of the water tunnel junctions.

We also argue that this variance is not a result of error in the fitting. Figure 2.13c,d shows two traces with the corresponding fit in red. Although the fit was obtained from the smoothed data, we show the raw data (offset by the background noise) to demonstrate that the slope is preserved under smoothing.

We hypothesize that the changes in tip geometry from junction to junction explains this variance. In the tunneling regime, the field enhancement decreases and the surface plasmon modes blue-shift as the junction gap decreases [176–179]. These two trends have opposing effects: a decrease in field enhancement decreases  $\beta$ , whereas a blue-shift in the surface plasmon modes, which for cut-tips will lie in the near-infrared, could increase  $\beta$ . In addition, the charge transfer plasmons are extremely important in the tunneling regime and are quite sensitive to the local ge-

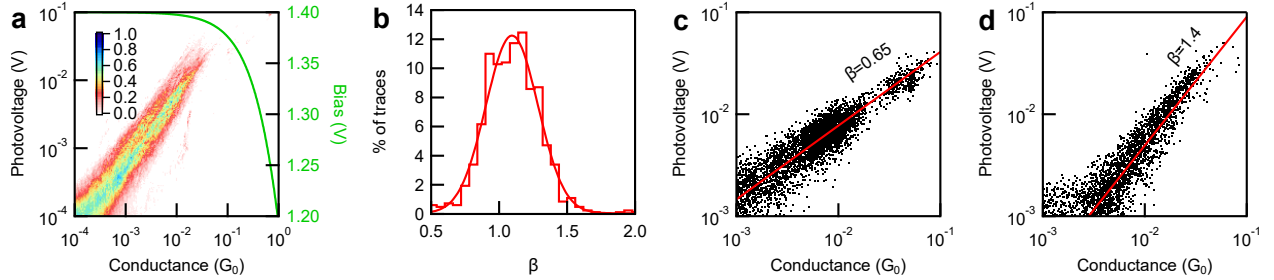


Figure 2.13: (a) 2D photovoltage-conductance histogram for experiment performed with  $2\text{ k}\Omega$  resistor and without any optical filter. Theoretical junction bias overlaid in green. Note that the second lobe corresponding to water tunnel junctions seen in Figure 2.2c is absent here. This is because at conductances above  $10^{-2}G_0$ , the applied bias begins to drop across the series resistor instead of the tunnel junction. This suppresses the current, along with the light emission. (b) Histogram of  $\beta$  values extracted from traces in (a). Traces with (c) sublinear and (d) superlinear  $\beta$ , plotted without smoothing.

ometry [180, 181]. The break-junction methodology samples many tip geometries that may result in superlinear or sublinear  $\beta$ . In Eq 2.1-2.3, these effects can be modeled by a  $D(E)$  that depends on the transmission coefficient  $\tau$  (see end of Section 2.7.4).

#### 2.7.4 The Role of $D(E)$

We will limit our discussion to featureless  $D(E)$ , i.e. independent of photon energy. First, we justify our choice of  $D(E) = 0.1 \text{ eV}^{-2}$ . When  $D(E)$  is constant, its role is primarily to regulate the relative intensities of the different orders of multi-electron emission. Specifically, larger  $D(E)$  results in a larger two-electron emission relative to the one-electron emission. The relative strengths of emission of different orders was measured by Peters and coworkers and is provided in Figure 3a of Ref. [153]. We qualitatively reproduce their experiment in Figure 2.14a using our chosen parameter of  $D(E) = 0.1 \text{ eV}^{-2}$ .

Next, we justify the chosen temperature increase of 200 K. The calculation in Figure 2.14a is not very sensitive to temperature; a lower temperature will provide similar agreement. However, the  $\beta$  of 1.7 reported in Ref. [150] requires a fairly substantial temperature increase. Assuming  $D(E) = 0.1 \text{ eV}^{-2}$ ,  $\Delta T$  should be approximately 200 K to fit both the  $\beta$  value reported in Ref. [150] and the  $\beta$  measured in this work. Figure 2.14b is the calculated conductance dependence for

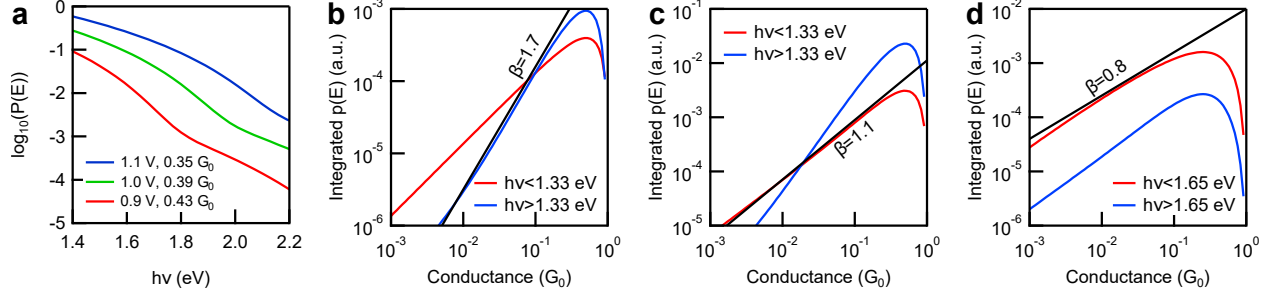


Figure 2.14: (a) Normalized emission spectra simulating Fig 3a in Ref. [153]. Parameters:  $D(E) = 0.1 \text{ eV}^{-2}$ ,  $T = 200 \text{ K}$ . (b) Integrated  $p(E)$  showing  $\beta = 1.7$  in overbias emission. Parameters:  $D(E) = 0.1 \text{ eV}^{-2}$ ,  $T = 200 \text{ K}$ ,  $V_{\text{applied}} = 1.33 \text{ V}$ . (c) Same parameters as (b) except  $D(E) = 0.5 \text{ eV}^{-2}$ , showing slightly superlinear dependence of underbias emission. (d) Same parameters as Fig 2.6c except with conductance dependent  $D(E)$ , resulting in consistent sublinear trend.

parameters in Ref. [150].

A different choice of  $D(E)$  will require a different temperature in order to produce the correct  $\beta$  in the overbias emission. Specifically, as  $D(E)$  increases, so does the required temperature. One might be concerned that this makes it impossible to estimate the temperature without a precise measure of  $D(E)$ . Worse, if  $D(E)$  is arbitrarily large, the temperature can also be arbitrarily large and the argument that blackbody radiation and multi-electron processes are incompatible would no longer hold.

However,  $D(E)$  cannot consistently exceed  $\sim \tau^{-1}$  across all wavelengths, otherwise the theory will predict more two-electron emission than one-electron emission. Since we sample conductance around  $0.1G_0$ ,  $D(E)$  should be less than  $10 \text{ eV}^{-2}$ .

A tighter bound is obtained by observing that although the underbias emission does display some superlinear dependence, it is only around  $\beta = 1.1$  on average. The superlinear dependence of underbias emission is not very sensitive to temperature (unlike the overbias emission), so we can use this value to estimate  $D(E)$  independent of temperature. We find a  $D(E) \approx 0.5 \text{ eV}^{-2}$  corresponds well to a  $\beta = 1.1$  in the underbias emission. Figure 2.14c shows the result for a calculation using the parameters in Ref. [150]. The main result of this analysis is that  $D(E)$  is somewhere between  $0.1$  and  $0.5 \text{ eV}^{-2}$ . Temperatures of  $2000 \text{ K}$  are inconsistent with this range of  $D(E)$ .

We use  $D(E) = 0.1 \text{ eV}^{-2}$  because a lower value fits a wider range of experiments. An elevated  $D(E)$  in the NIR is easily explained by the presence of surface plasmon resonances in the NIR. In other words, it is sufficient to assume that  $D(E) \approx 0.5 \text{ eV}^{-2}$  for photon energies in the underbias regime to obtain  $\beta = 1.1$  for underbias emission. We need not assume  $D(E) \approx 0.5 \text{ eV}^{-2}$  across the entire spectrum.

Finally, we hypothesize that the variance in  $\beta$  is best explained by the gap dependence of the surface plasmon resonances, which causes a correlation between conductance and  $D(E)$ . To demonstrate this, we model the decrease in electric field enhancement with a simple quadratic function  $D(E, \tau) = \frac{1}{160} \log(\tau)[\log(\tau) + 8]$ . The resulting sublinear conductance dependence is plotted in Figure 2.14d. Superlinear conductance in both the underbias emission and overbias emission can be explained with a  $D(E)$  that increases as a function of conductance or simply a larger value for  $D(E)$ .

## Chapter 3: Too Hot for Photon-Assisted Transport

### 3.1 Preface

This chapter is adapted from the manuscript entitled *Too Hot for Photon-Assisted Transport: Hot-Electrons Dominate Conductance Enhancement in Illuminated Single-Molecule Junctions*, by E-Dean Fung, Olgun Adak, Giacomo Lovat, Diego Scarabelli, and Latha Venkataraman [182]. Olgun initiated the project, designed most of the experimental apparatus, and performed the preliminary experiments [183]. Giacomo Lovat performed the temperature dependence measurements, and Diego nanofabricated devices for launching surface plasmon polaritons. I would also like to thank Markus Raschke and Vasily Kravtsov for sharing their expertise on nano-plasmonics.

### 3.2 Introduction

The ability to control charge transport across single-molecule devices using light would provide an important breakthrough towards the expansion of functionality at the nanometer scale [9, 35, 184, 185]. Theoretical studies have predicted that the conductance of a single molecule could be enhanced upon illumination via a mechanism commonly referred to as photon-assisted transport (PAT) [186–189]. PAT was first observed in superconductors under microwave radiation [190, 191], but the photon flux necessary to observe PAT in single-molecule junctions is often much larger than what can be achieved using traditional diffraction-limited optics. However, with recent advances in photonics, electromagnetic fields can be concentrated into sub-diffraction-limited volumes by coupling the fields to the localized surface plasmons resonances of metal nanostructures, making it possible to observe light-enhanced charge transport through molecular systems [192–197].

Several pioneering experiments have attributed optically induced current enhancements in tun-

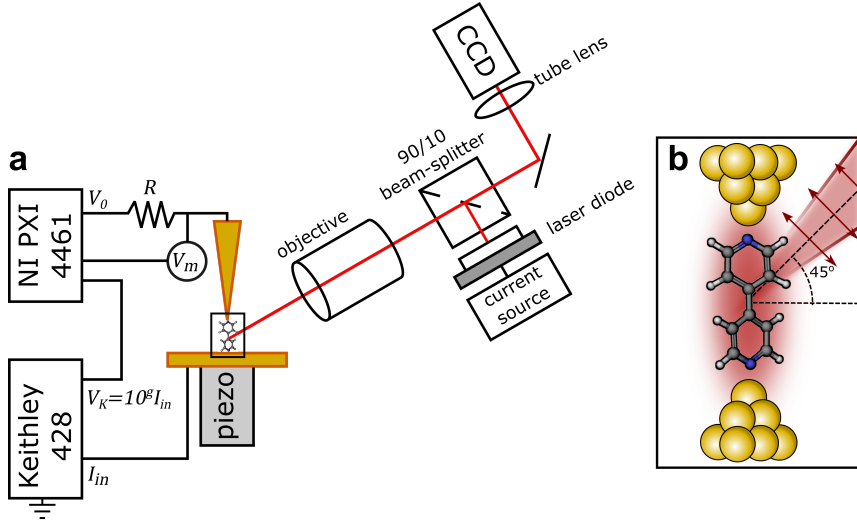


Figure 3.1: (a) Schematic of STM modified for illuminated break-junction measurements. (b) Diagram of illuminated single-molecule junction.

nel junctions [198–202], gold point-contacts [76, 203, 204], and, more recently, molecular junctions to PAT [121–123]. However, theoretical [205–208] and experimental [124, 209–211] studies have shown that the same localized surface plasmons that confine light around nanostructures also give rise to populations of hot-electrons. Despite strong interest in both phenomena, there has been little discussion of the relationship between PAT and hot-electron transport [212], and it is often assumed that all observed optical signatures are due to one effect or the other. Furthermore, studies of PAT in single-molecule systems either have stringent fabrication requirements [123] or do not reliably couple light into the junction [122].

Previous works have shown that scanning tunneling microscopes can be used to effectively couple photons into single-molecule junctions [213, 214]. In this study, we utilize a similar system which permits polarization-dependent measurement of light-induced conductance enhancement over thousands of junctions. By taking advantage of detailed knowledge of the transport properties of 4,4'-bipyridine (BP) in an Au-molecule-Au junction [29, 183], we experimentally probe the relationship between the molecular junction and light-induced enhancement. We then use a Landauer-like model to show that PAT and hot-electron transport have equivalent steady-state current signatures. A straightforward calculation shows that hot-electron transport constitutes the

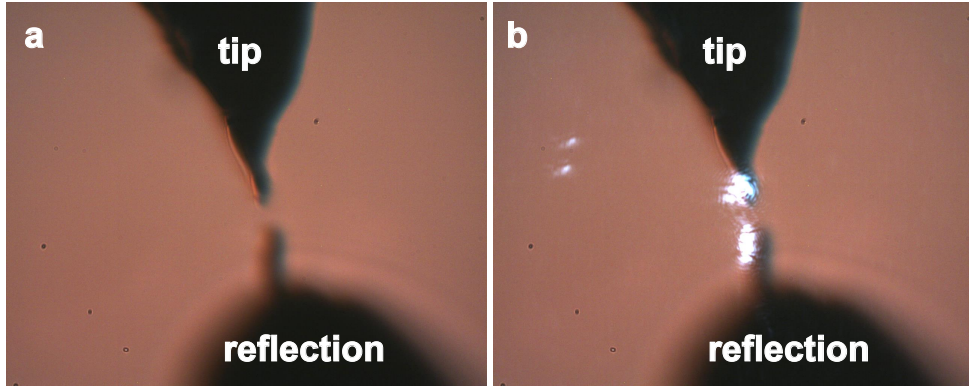


Figure 3.2: Optical image of STM tip (a) without and (b) with illumination.

majority of light-induced enhancement in conductance, which we validate experimentally.

### 3.3 Experimental Methods

Figure 3.1a shows a schematic of the modified STM. We illuminated the junction by focusing a 980 nm continuous-wave laser (Thorlabs, Inc.) at the junction using a 50x microscope objective with numerical aperture 0.42 and a working distance of 17 mm (Mitutoyo). The same objective is used to image the tip and align the laser, as shown in Figure 3.2. The beam was angled at  $(45 \pm 2)^\circ$  with respect to the substrate and polarized parallel to the plane of incidence, as shown in Figure 3.1b. We operate the laser diode at around 100 mW and estimate the peak intensity at the junction to be  $2000 - 6000 \text{ kW cm}^{-2}$ .

To more efficiently couple light into the junction, the measurements are performed without solvent by thermally sublimating BP onto the substrate. After depositing BP onto the substrate, we heated the substrate to  $100^\circ\text{C}$  for approximately 5 minutes to decrease the density of BP on the surface. This additional procedure reduces the probability of forming multi-molecule junctions. Aside from these adjustments, the experiments are performed as described in Section 1.4.

### 3.4 Experimental Results

We conducted STM-BJ measurements on BP with and without laser illumination at a bias of 180 mV. In order to account for any potential time dependence, we switched the laser on or off

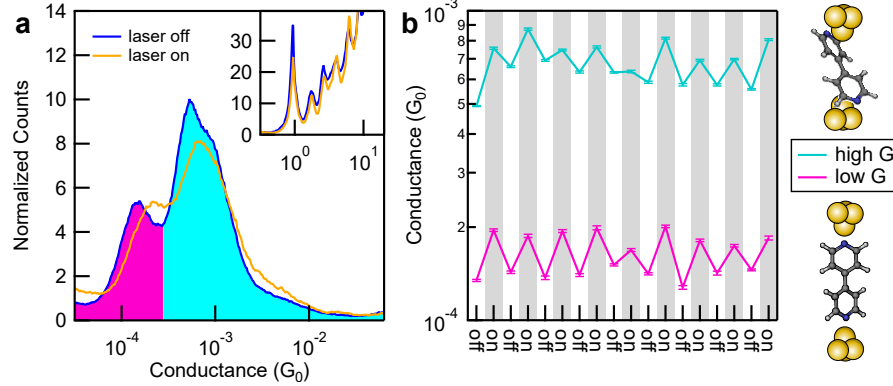


Figure 3.3: (a) 1D conductance histograms of BP junctions at 180 mV bias for dark (laser off) and illuminated (laser on) junctions. Inset shows the high-conductance region for the same histograms. The high (low) conductance peak is shaded in teal (magenta). (b) A series of conductance measurements where the laser is successively turned on and off. Each point represents peak positions in a conductance histogram constructed from 500 traces. Error bars represent the standard error of the fit. Binding geometry of high- and low-conductance configurations are depicted on the right.

every 500 measurements. The experiment was paused for 10 minutes every time the laser was switched on (off) to allow the tip to expand (contract) and reach steady-state temperature. We combined nine sets of 500 traces to create the 1D conductance histograms shown in Figure 3.3a. Each histogram was created from 4500 conductance-displacement traces collected without data selection. Both histograms show the two conductance peaks—one high and one low—characteristic of Au-BP-Au junctions. It is immediately apparent that the conductance peaks for junctions under illumination (orange) are shifted with respect to those of junctions without illumination (blue). By fitting each histogram in Figure 3.3a with a double Lorentzian curve, we extracted the most probable conductance of a BP junction in either a high-conducting (teal-filled) or low-conducting (magenta-filled) configuration. Comparing the most probable conductance of dark and illuminated junctions, we obtain a 27% and 33% enhancement in conductance for high- and low-conductance peaks, respectively.

Figure 3.3b shows the evolution of the high and low peak-conductance values at 180 mV bias as the laser is switched on and off, each point representing the fitted peaks in a conductance histogram created from 500 individual traces. The conductance is clearly modulated by near-infrared illumination. The observed conductance enhancement and switching behavior is reproducible with

Table 3.1: Measured peak-conductance values and calculated on-off ratios.

Trial	high G, laser off ( $G_0$ )	low G, laser off ( $G_0$ )	high G, laser on ( $G_0$ )	low G, laser on ( $G_0$ )	on-off ratio, high G	on-off ratio, low G
1	5.63E-4	1.27E-4	7.16E-4	1.89E-4	1.27	1.33
2	5.86E-4	1.52E-4	7.60E-4	2.12E-4	1.29	1.39
3	5.52E-4	1.21E-4	7.17E-4	1.74 E-4	1.29	1.44
4	6.29E-4	1.42E-4	6.87E-4	1.83E-4	1.09	1.29
5	5.53E-4	1.19E-4	6.12E-4	1.45E-4	1.11	1.22

multiple tip and sample pairs, although the actual conductance enhancement varies between experiments because of variations in tip shape and alignment. Across all experiments, however, the enhancement observed in low-conducting peaks is always higher than that observed in high-conducting peaks. We summarize these results in Table 3.1.

Before considering any conductance enhancement mechanisms unique to light, we must rule out mechanisms pertaining to thermal effects under illumination which might explain the enhanced conductance. We first consider the impact of an increase in the electrode equilibrium temperature due to laser heating. To estimate the electrode temperature under illumination, we performed STM-BJ measurements on BP junctions while heating the substrate up to 110 °C using a resistive heating element [215]. The 1D conductance histograms are shown in Figure 3.4a,c. Above 110 °C, we did not observe clear conductance peaks, since BP desorbs from the substrate at that temperature. This places an upper bound on the temperature in the illuminated junctions. Additionally, heating decreases the height of the conductance peak at  $1G_0$ , similar to what we observe under illumination (see inset of Fig 3.3a). This is a result of increased mechanical instability of the Au point-contact [216, 217]. Using the average number of points around the  $1G_0$  peak in a single trace as a rough gauge of temperature, we estimate that the junction is heated to about 45 °C under illumination (Fig 3.4b). More importantly, we find that the conductance does not change with temperature (Fig 3.4c,d). We conclude, therefore, that the increase in temperature cannot account for the conductance enhancement observed under illumination.

Second, we briefly consider the impact of a temperature differential between the two electrodes,

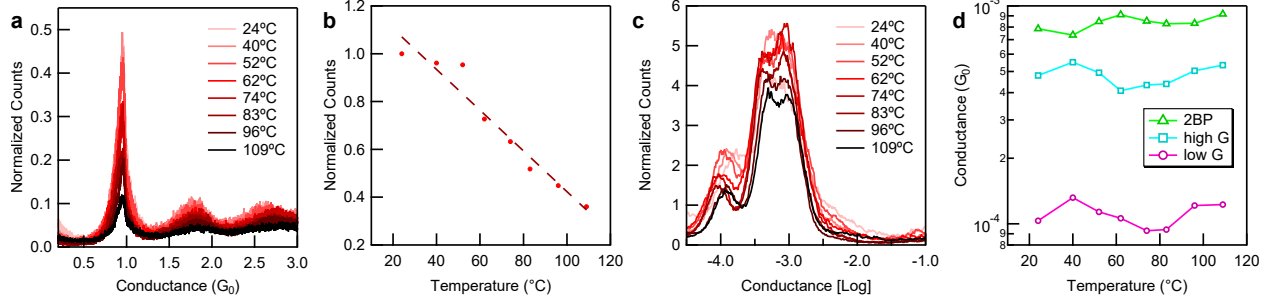


Figure 3.4: (a) Linearly-binned conductance histogram for atomic point-contacts measured in the presence of BP at a range of temperatures. (b) Number of points around  $1G_0$  peak normalized by the number of points at room temperature as a function of temperature. (c) Conductance histogram of the same data showing the molecular peaks at a range of temperatures. (d) Extracted peak-conductance values as a function of temperature.

either due to the spatial profile of the beam cross-section or to geometric differences between the tip and substrate that may give rise to thermoelectric current. Thermopower measurements of BP at temperature gradients of up to  $27^\circ\text{C}$  produce around  $20\text{ pA}$  of thermoelectric current [215]. This is approximately 100 times smaller than the typical currents in BP junctions under  $180\text{ mV}$  bias. As a result, the contribution of thermal gradients to the current enhancement seen in Figure 3.3a can safely be neglected.

Next, we explore the impact of electrode separation on the measured conductance enhancement by creating 2D conductance-displacement histograms of the data presented in Figure 3.3a. These are shown in parts a and b of Figure 3.5 for dark and illuminated junctions, respectively. In both histograms, we again see the two characteristic conductances, with the low-conductance geometry only occurring after the junction has been extended by around  $2\text{ \AA}$ . When the laser is on, we make two observations. First, the high-conductance plateaus are, on average shorter by almost  $0.5\text{ \AA}$ , and there are more junctions which form low-conductance traces, as indicated by the color scale. Second, the junctions break to noise much sooner, as evidenced by the early onset of the noise floor. We attribute these phenomena to the aforementioned decrease in junction lifetimes owing to the elevated temperature.

Since the conductance of BP is inversely proportional to electrode separation, it is important to check that the shifts upon illumination are not due to selection bias against more extended (less

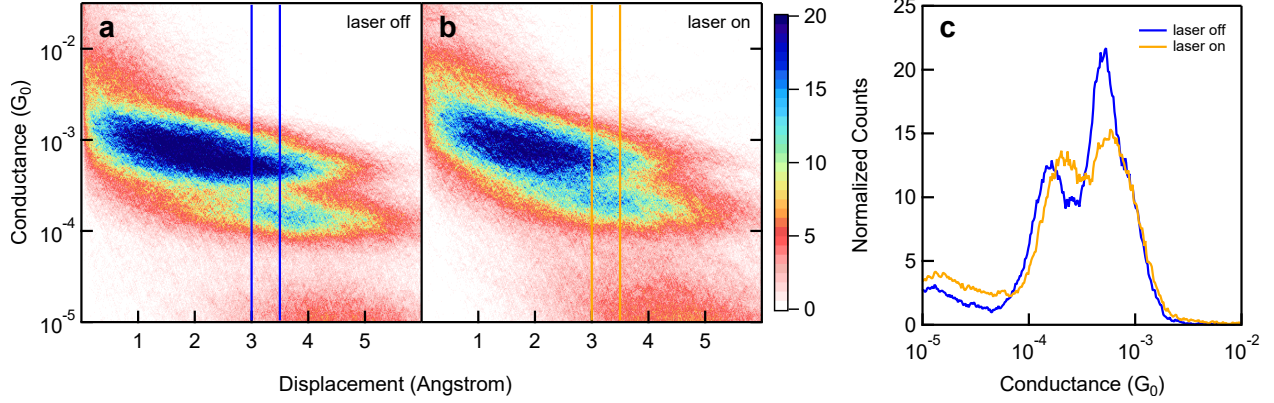


Figure 3.5: 2D conductance-displacement histograms of BP measured (a) without and (b) with illumination. Vertical lines delimit the range of displacement values used to construct (c), a 1D conductance histogram, normalized to the total number of points collected in the range of selected displacement values. The shift in Figure 3.3a is preserved under this analysis.

conducting) junctions. To this end, we constructed conductance histograms shown in Figure 3.5c by considering only data points which are measured at a junction separation between  $3\text{ \AA}$  and  $3.5\text{ \AA}$  (data between vertical lines in Fig 3.5a,b). The histograms in Figure 3.5c are normalized to the total number of points falling within the specified range. Fitting these histograms to double Lorentzian functions returns an enhancement in conductance of 14% and 34% for high- and low-conductance peaks, respectively, accentuating the difference in enhancement between the different binding geometries of BP. This rules out the possibility that the observed enhancement in illuminated junctions is merely due to selection bias against low-conducting junctions.

### 3.5 Theoretical Discussion

We now turn to an explanation of the conductance enhancement seen in Figure 3.3 in terms of the Landauer-Büttiker formalism. As presented in Section 1.1, current through a junction under an externally applied bias voltage without illumination is written as [1, 85]

$$I_D(V) = \frac{2e}{h} \int_{-\infty}^{\infty} dE T(E) \left[ f_L \left( E - \frac{eV}{2} \right) - f_R \left( E + \frac{eV}{2} \right) \right] \quad (3.1)$$

where  $I_D$  denotes the dark current.

For junctions under illumination, we must consider two main changes to Eq 3.1. First, electronic states in the molecule interact with the electromagnetic field, resulting in a modified transmission function  $T'(E)$ . The time-averaged current through the junction is obtained by substituting Eq 3.2 into Eq 3.1, where  $V_{\text{opt}}$  is the amplitude of the AC voltage generated across the junction by the light,  $J_n$  denotes the  $n^{\text{th}}$  order Bessel function of the first kind, and  $\hbar\omega$  is the photon energy [186, 188].

$$T'(E) = \sum_{n=-\infty}^{\infty} J_n^2 \left( \frac{eV_{\text{opt}}}{\hbar\omega} \right) T(E + n\hbar\omega) \quad (3.2)$$

The modified transmission function is simply a sum of the original transmission function shifted by integer multiples of  $\hbar\omega$ . The square of the Bessel function gives the probability of absorbing or emitting  $n$  photons, and the transmission function in each term of the sum is shifted to account for the new energy of the tunneling electron. When the field intensity is small such that  $eV_{\text{opt}} \ll \hbar\omega$ , multiple-photon absorption and emission processes ( $|n| > 1$ ) can be neglected. The modified transmission function can then be expanded to second order in  $eV_{\text{opt}}/\hbar\omega$  and rewritten as the original transmission function plus a term proportional to the light intensity.

$$T'(E) \approx T(E) + \frac{1}{4} \left( \frac{eV_{\text{opt}}}{\hbar\omega} \right)^2 \left[ T(E + \hbar\omega) + T(E - \hbar\omega) - 2T(E) \right] \quad (3.3)$$

The modification of the transmission function represents the photon-assisted transport (PAT) discussed in the introduction and can be traced back to the work of Tien and Gordon [191]. The Tien-Gordon model assumes that PAT is an adiabatic process and that the interaction between the electrons and the electromagnetic field occurs only in the bridge and not in the leads [184, 186, 218]. Since the HOMO-LUMO gap of BP is much larger than the photon energy and the frequency used in this experiment is smaller than the plasma frequency of gold, we expect this model to qualitatively capture the steady-state behavior of PAT [219, 220].

The second modification to the transport model under illumination pertains to the electron distributions in the leads. As noted before, the steady-state temperature in the leads is raised under

illumination, which changes the Fermi distribution slightly. More importantly, electrons in the leads can absorb photons, which results in transient non-equilibrium electron distributions which decay via electron-electron interactions and electron-phonon coupling [221, 222]. The time required for these so-called hot-electron distributions to thermalize into equilibrium Fermi distributions is around 500 fs [223, 224], at least an order of magnitude longer than the charge transfer time across a pyridine/gold interface [225]. We argue, therefore, that the Fermi distributions in Eq 3.1 should be replaced with the non-equilibrium hot-electron distribution  $f_{\text{hot}}$  given in Eq 3.4, where  $f'$  denotes the equilibrium Fermi distribution for a slightly elevated temperature and  $\Delta\rho_0$  is a constant proportional to the intensity of the illumination [224]. Like  $T'(E)$  for PAT,  $f_{\text{hot}}$  is the original Fermi-distribution plus a term proportional to the light intensity, such that  $f_{\text{hot}}$  reduces to the Fermi-distribution in the limit that the light intensity goes to zero. This substitution is similar to those performed in recent works [124, 210].

$$f_{\text{hot}} = f'(E) + \Delta\rho_0(V_{\text{opt}}^2) \left\{ [1 - f'(E)] f'(E - \hbar\omega) - f'(E) [1 - f'(E + \hbar\omega)] \right\} \quad (3.4)$$

In order to understand how PAT and hot-electron distributions enhance the current in BP, we consider the two mechanisms separately. Based on theoretical and experimental work, the transmission function for BP junctions is well approximated by the single-level model [226].

$$T(E) = \frac{\Gamma^2}{(E - \varepsilon)^2 + \Gamma^2} \quad (3.5)$$

The transmission function for high-conducting BP junctions is given by the teal curve in Figure 3.6a. If we approximate the Fermi distribution with a step function, the additional current due to PAT alone is proportional to the blue area less twice the red area. It is apparent from Figure 3.6a that for a given applied bias, the current increase from PAT is maximum when  $\hbar\omega = \varepsilon$ . For the high-conducting configuration of BP junctions,  $\varepsilon$  is measured to be 1.2 eV, justifying our choice of wavelength, which has photon energy 1.27 eV [183].

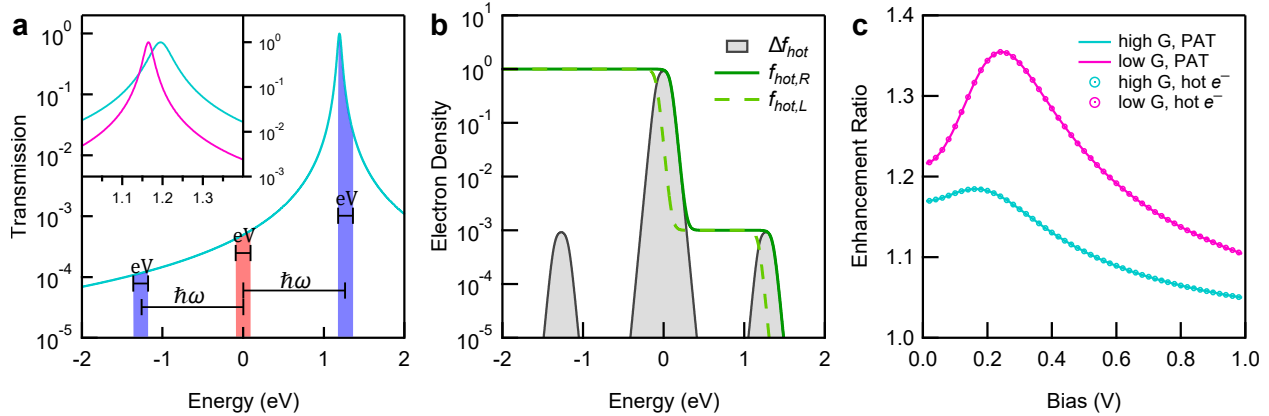


Figure 3.6: (a) Calculated transmission function of the high-conducting configuration of BP on a semi-log plot. The additional current from photon-assisted tunneling is proportional to the blue area less twice the red area. The inset compares the transmission functions of high-conducting (teal) and low-conducting (magenta) BP junctions. (b) The computed hot-electron distribution for the right (solid-green) and left (dashed-green) electrodes, for  $\Delta\rho_0 = 10^{-3}$  and junction bias of 180 mV. The difference is the shaded area. (c) Calculated enhancement ratios as a function of bias using the transmission function of high-conducting (teal) and low-conducting (magenta) BP junctions. Solid curves were calculated using only photon-assisted tunneling; circular markers were calculated using only hot electron distributions. These curves cannot be distinguished.

Now we determine the effect of the hot-electron distribution without PAT. Figure 3.6b provides the calculated hot-electron distribution for the left and right electrodes, assuming  $\Delta\rho_0 = 10^{-3}$  and a junction bias of 180 mV. Taking the difference reveals that the overall effect of the hot-electron distribution is to sample the transmission function above and below the Fermi level in much the same manner as PAT. Indeed, if  $\Delta\rho_0 = (eV_{\text{opt}}/2\hbar\omega)^2$ , we expect the current enhancement arising purely from the hot electrons to be indistinguishable from current enhancement due to PAT.

To show this explicitly, we computed the current enhancement ratio  $I_{\text{opt}}/I_D$  as a function of bias for both high- and low-conducting junctions (Fig 3.6c), where the current in illuminated junctions  $I_{\text{opt}}$  is calculated in two ways. We first assumed that the enhancement is due purely to PAT, substituting Eq 3.3 into Eq 3.1 and using equilibrium Fermi distributions at an elevated temperature. A  $V_{\text{opt}}$  of 50 mV returns values consistent with our experiment. The computed enhancement ratio is higher for low-conducting junctions than for high-conducting junctions at all biases, completely consistent with our experimental results. This is predominantly a consequence of the smaller coupling,  $\Gamma$ , in low-conducting junctions (see Fig 3.9d). Second, we computed the enhancement ratio

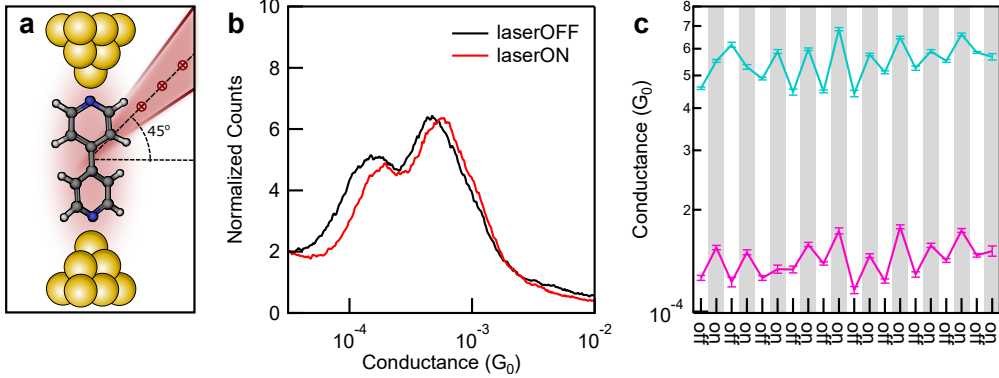


Figure 3.7: (a) Diagram of an illuminated a BP junction where polarization excludes PAT (direction of polarization is into/out of the plane). (b) 1D conductance histograms for experiment performed at 300 mV bias where the polarization excludes PAT. (c) The extracted peak-conductance values of (b) over time.

using only hot-electron distributions, substituting the Fermi distributions in Eq 3.1 with Eq 3.4 without changing the transmission function to calculate  $I_{\text{opt}}$ . For a direct comparison with PAT, we chose  $\Delta\rho_0 = (eV_{\text{opt}}/2\hbar\omega)^2$ . As demonstrated by the circular markers in Figure 3.6c, the effect of hot electrons on transport is indistinguishable from the time-averaged effects of PAT. Thus, measurements of time-averaged transport under illumination cannot be used to distinguish between hot-electron transfer and PAT. A formal argument is provided in Section 3.7.3. It is necessary, therefore, to estimate the relative contributions of PAT and hot-electron distributions.

To this end, we estimated  $\Delta\rho_0$  in terms of the absorption coefficient  $\alpha$ , the hot-electron relaxation time  $\tau$ , the density of states  $g$ , the electron-phonon mean free path  $\lambda$ , and the electrode separation distance  $d$  in Eq 3.6 below (derivation in Section 3.7.4).  $c$ ,  $\epsilon_0$ , and  $e$  are speed of light, free space permittivity, and elementary charge, respectively. Plugging in values from previous experiments into Eq 3.6 shows that the effect of hot-electron distributions is more than 100 times that of PAT [223, 227–230].

$$\Delta\rho_0 = \frac{\alpha\tau c\epsilon_0}{2g\lambda e^2 d^2} \left( \frac{eV_{\text{opt}}}{\hbar\omega} \right)^2 \approx 36 \left( \frac{eV_{\text{opt}}}{\hbar\omega} \right)^2 \quad (3.6)$$

To test if this is indeed an accurate estimate for  $\Delta\rho_0$ , we carried out the same experiments but with the laser polarization rotated to be orthogonal to the junction axis (parallel to the substrate),

as depicted in Figure 3.7a. In Figure 3.7b, we show conductance histograms measured under this configuration where we clearly observe a conductance enhancement, albeit reduced. This is explained by a reduced plasmonic field enhancement, which is minimized when the polarization is perpendicular to the junction direction. Since the electric field must be parallel to the junction axis for photon-assisted transport to occur, the observed enhancement must be due to hot-electron distributions.

### 3.6 Conclusion

We have shown that the conductance of single-molecule junction can be enhanced under near-infrared radiation and find that the enhancement is predominantly due to hot-electron transport. Furthermore, the different binding geometries of 4,4'-bipyridine also reveal how subtle changes in the transmission function affect hot-electron transport, establishing some basic rules for designing organic photo-switches. We have shown experimentally that the coupling of the molecule to the electrodes controls the optical on-off ratio, and theory predicts that low-voltage devices will be very sensitive to photon energy. These ideas pave the way towards tailored molecular-scale optoelectronic devices.

### 3.7 Supplementary Information

#### 3.7.1 Additional Data

Table 3.2 summarizes the results from all experiments performed with the polarization perpendicular to the junction axis (see Fig 3.7a). The performance varies widely from experiment to experiment. Some experiments show no appreciable enhancement, whereas others show more enhancement than expected from calculations (see Fig 3.9a). We attribute this variability to inconsistent field enhancement in the junction. We also note that propagating surface plasmons may play a larger role at this polarization.

Table 3.2: Measured peak-conductance values and calculated on-off ratios for polarization perpendicular to the plane of incidence

Trial	high G, laser off ( $G_0$ )	low G, laser off ( $G_0$ )	high G, laser on ( $G_0$ )	low G, laser on ( $G_0$ )	on-off ratio, high G	on-off ratio, low G
1	5.58E-4	1.20E-4	5.92E-4	1.26E-4	1.06	1.04
2	5.57E-4	1.18E-4	6.50E-4	1.42E-4	1.17	1.20
3	4.96E-4	1.33E-4	5.86E-4	1.51E-4	1.18	1.14
4	6.30E-4	1.53E-4	5.91E-4	1.56E-4	0.94	1.01
5	6.31E-4	1.22E-4	6.13E-4	1.23E-4	0.97	1.00
6	4.83E-4	1.18E-4	5.04E-4	1.25E-4	1.04	1.06
7	5.25E-4	1.32E-4	6.24E-4	1.61E-4	1.19	1.22
8	5.32E-4	1.29E-4	6.01E-4	1.58E-4	1.13	1.23

### 3.7.2 Theory for Non-Equilibrium Electron Distributions

The hot-electron distribution  $f_{\text{hot}}$  can be decomposed into an equilibrium part, and a non-equilibrium part.

$$f_{\text{hot}}(E) = f_{\text{eq}}(E) + f_{\text{neq}}(E) \quad (3.7)$$

A number of theoretical explorations of  $f_{\text{neq}}$  have been made in recent years. We begin with the work of Govorov and coworkers [205]. The non-equilibrium electron distribution is further decomposed into two parts shown in Figure 3.8a: a flat region for energies in the range  $[-\hbar\omega, +\hbar\omega]$  due to localized surface plasmons (LSPs) and a triangular region for energies in the range  $[-\hbar v_F q_n, +\hbar v_F q_n]$  due to propagating surface plasmons (PSPs).  $E_F$  and  $v_F$  are the Fermi energy and Fermi velocity, respectively,  $\hbar\omega$  is the photon energy, and  $q_n$  is a wavevector for propagating plasmons.  $f_{\text{neq}}$  must be anti-symmetric to conserve charge.

We neglect the contributions due to PSPs since the effect is only significant close to the Fermi energy. Changes in the electron distribution in this area do not significantly impact the electron transport of BP because the transmission function for BP is nearly flat around the Fermi energy. We confirm this in Figure 3.8b. There is a 5% increase in enhancement across all biases due to the PSPs, which is small compared to the effect of LSPs. In this calculation, we assumed a PSP energy

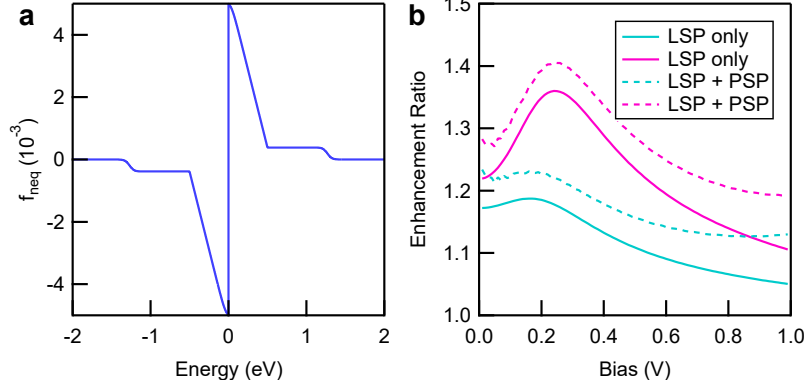


Figure 3.8: (a) Non-equilibrium hot-electron distribution due to localized and propagating surface plasmons. (b) Enhancement ratio vs bias curves assuming only localized surface plasmons (LSP) and including both LSPs and propagating surface plasmons (PSP). Parameters corresponding to high-conductance and low-conductance BP geometries plotted in teal and magenta, respectively.

of 0.5 eV and an amplitude of 0.1 (parameter  $A$  in Eq 5 of Ref. [205]).

Turning to the work of Kornbluth *et al.* [206], we find an expression for the flat region.

$$f_{\text{neq}}(E) = \Delta\rho_0 \tanh\left(\frac{E}{2k_B T}\right) \frac{\cosh\left(\frac{\hbar\omega}{k_B T}\right) - 1}{\cosh\left(\frac{\hbar\omega}{k_B T}\right) + \cosh\left(\frac{E}{k_B T}\right)} \quad (3.8)$$

The non-equilibrium part of Eq 3.4 can be rewritten as

$$f_{\text{neq}}(E) = \Delta\rho_0 \tanh\left(\frac{E}{2k_B T}\right) \frac{\frac{1}{2} \left(e^{\frac{\hbar\omega}{k_B T}} - 1\right)}{\cosh\left(\frac{\hbar\omega}{k_B T}\right) + \cosh\left(\frac{E}{k_B T}\right)} \quad (3.9)$$

For  $\hbar\omega \gg k_B T$ , Eq 3.8 is closely approximated by Eq 3.9.

### 3.7.3 Equivalence of Photon-Assisted Tunneling and Hot-Electron Transport

The non-equilibrium part of Eq 3.4 is

$$f_{\text{neq}}(E) \propto [1 - f(E)] f(E - \hbar\omega) - f(E) [1 - f(E + \hbar\omega)] \quad (3.10)$$

Using the relation (Eq 54 of Ref. [231])

$$f(E) \left[ 1 - f(E + x) \right] = \frac{f(E) - f(E + x)}{1 - e^{-\frac{x}{k_B T}}} \quad (3.11)$$

we obtain

$$f_{\text{neq}}(E) \propto \frac{1}{1 - e^{-\frac{\hbar\omega}{k_B T}}} \left[ f(E - \hbar\omega) - 2f(E) + f(E + \hbar\omega) \right] \quad (3.12)$$

For  $\hbar\omega \gg k_B T$

$$f_{\text{neq}}(E) \propto \left[ f(E - \hbar\omega) - 2f(E) + f(E + \hbar\omega) \right] \quad (3.13)$$

As shown in Figure 3.6a, this is precisely the effect of PAT.

### 3.7.4 Derivation for $\Delta\rho_0$

For a field intensity  $I$ , the number of photons absorbed per unit volume, is:

$$n_{\text{photon}} = \frac{\alpha\tau I}{\lambda\hbar\omega} \quad (3.14)$$

We estimate the absorption coefficient  $\alpha$  using the complex index of refraction provided in the work of Olmon *et al.*, assuming the relevant length scale is given by the electron-phonon mean free path  $\lambda$  [230, 232]. For  $\hbar\omega = 1.27$  eV,  $\alpha$  is approximately 38%. We take  $\tau = 500$  fs and  $\lambda = 30$  nm [223, 224, 227, 228].

Assuming that the absorption spectrum is flat (a reasonable assumption for Au near the Fermi energy),  $\Delta\rho_0$  is simply given by

$$\Delta\rho_0 = \frac{n_{\text{photon}}}{g\hbar\omega} = \frac{\alpha\tau}{g\lambda(\hbar\omega)^2} \cdot I = \frac{\alpha\tau}{g\lambda(\hbar\omega)^2} \cdot \frac{c\epsilon_0}{2} |E|^2 = \frac{\alpha\tau c\epsilon_0}{2g\lambda e^2 d^2} \left( \frac{eV_{\text{opt}}}{\hbar\omega} \right)^2 \quad (3.15)$$

The density of states  $g$  is calculated assuming a free electron model [229]. We take  $d = 3$  Å and  $g = 1.6 \times 10^{22}$  eV<sup>-1</sup> cm<sup>-3</sup>.

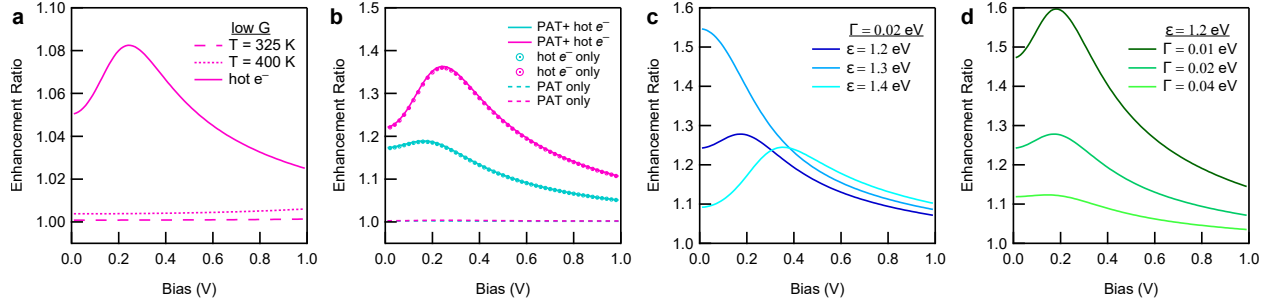


Figure 3.9: (a) The calculated enhancement ratio as a function of bias assuming only Fermi-distributions at two temperatures (dashed curves). The solid line is the enhancement ratio assuming hot-electron distributions with no field enhancement at a temperature of 325 K. All calculations are performed using parameters for low-conducting junctions. (b) The enhancement ratio as a function of bias, with  $V_{\text{opt}} = 4.5$  mV using full theory (solid line), only hot electron distributions (circular markers), and only PAT (dashed line). Parameters corresponding to high-conductance and low-conductance BP geometries plotted in teal and magenta, respectively. (c) and (d) are the calculated enhancement ratio vs bias curves while varying  $\varepsilon$  and  $\Gamma$ , respectively.

### 3.7.5 Additional Calculations

Figure 3.9a reiterates that the conductance enhancement observed cannot be due to a change in the steady-state temperature at the junction. Even at temperatures where BP desorbs from the substrate, the expected conductance enhancement is less than 1%. Without assuming any field enhancement and only using hot-electron distributions (solid line), the conductance enhancement for the low-conducting configuration is still around 10 times larger than the enhancement possible with just equilibrium Fermi distributions.

Figure 3.9b shows that the majority of enhancement is due to hot-electron tunneling; the contribution of PAT to the enhancement is minimal. The  $V_{\text{opt}}$  required to achieve this enhancement is on the order of 4.5 mV, which corresponds to a field enhancement of 2.3 if we assume a local intensity of  $5770 \text{ kW cm}^{-2}$ . This is likely an overestimate of the intensity. For more conservative estimates of the intensity, the field enhancement factor is on the order of 10.

To understand how the enhancement depends on the transmission function, we calculate the enhancement while varying the alignment parameter  $\varepsilon$  and the coupling parameter  $\Gamma$ , as shown in Figure 3.9c,d. The photon energy is fixed at 1.27 eV. As  $\varepsilon$  approaches the photon energy, the peak enhancement occurs at lower and lower bias. The value of the peak enhancement also increases

dramatically. Decreasing  $\Gamma$  leaves the peak location the same but increases the enhancement ratio across all biases.

## Chapter 4: Breaking Down Resonance

### 4.1 Preface

This chapter is adapted from the manuscript entitled *Breaking Down Resonance: Nonlinear Transport and the Breakdown of Coherent Tunneling Models in Single Molecule Junctions*, by E-Dean Fung, David Gelbwaser, Jeffrey Taylor, Jonathon Low, Jianlong Xia, Iryna Davydenko, Luis Campos, Seth Marder, Uri Peskin, and Latha Venkataraman [233]. Brian Capozzi and Jeffrey Taylor performed the initial measurements which inspired this work [234]. Jianlong Xia synthesized TDO4, which was purified by Jonathon Low. Iryna Davydenko synthesized squaraine. David Gelbwaser and Uri Peskin helped investigate possible theoretical explanations.

### 4.2 Introduction

Single-molecule devices enable exploration of charge transport at the sub-nanometer scale, potentially unveiling functionality with no solid-state analogues. Two-electrode systems where the molecule is chemically bound to both electrodes via anchoring groups are particularly interesting for their simplicity. Most studies on such systems thus far have focused on the low bias and non-resonant tunneling regime, leveraging chemical principles to modify the electronic structure and control transport behavior [11]. By contrast, two-electrode experiments on charge transport in the resonant tunneling regime, where the molecular orbital that dominates transport lies close to or within the transport window, are limited, in part because of the high biases typically required to achieve resonance but also because resonant electrons can tunnel inelastically and stimulate junction rupture [235–242]. Despite this challenge, transport in the resonant tunneling regime remains attractive due to the presence of strong electron-electron and electron-phonon interactions which are expected to produce nonlinear effects beyond the realm of Landauer-Büttiker theory of

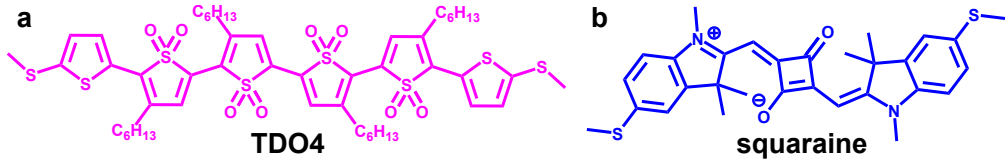


Figure 4.1: Molecular structure of (a) TDO4 (majority electron transport) and (b) squaraine (majority hole transport). The terminal methyl-sulfide groups serve as linkers to bind to the Au electrodes.

elastic scattering.

A number of pioneering studies have successfully demonstrated resonant-tunneling in single-molecule devices [36, 243, 244], and two nonlinear phenomena have consistently emerged: Negative Differential Resistance [245–250] (NDR) and hysteresis [26, 28, 32, 33, 251]. Although each of these phenomena has been observed in a variety of different molecules, the molecules frequently have highly-localized molecular orbitals, and the experiments are often performed at low temperature, which limits their application to devices. A variety of mechanisms have been proposed to explain the presence of NDR and hysteresis in single-molecule devices. The two theories with arguably the greatest generality are the blocking-state model [252–254] and the polaron model [255, 256], although other explanations for NDR and hysteresis in molecular devices exist [245].

In this work, we report both abrupt NDR and hysteresis in two molecular backbones: an oligomer of an electron-deficient thiophene-1,1-dioxide unit (TDO4) and a squaraine-based derivative with structures shown in Figure 4.1. We carry out measurements in both non-polar and polar solvent environments. The two molecules complement one another in that electrons dominate transport in TDO4, whereas holes dominate transport in squaraine. Fitting thousands of individual single-molecule junction current-voltage ( $I$ - $V$ ) traces to a single-level model within the Landauer-Büttiker formalism, we show that the mechanism for NDR must be induced by charging and that the hysteresis is characterized by a shift in level alignment with little modification to the level broadening. By changing the speed at which the experiment is performed, we find that the charging mechanism is stochastic in nature and can be reversed by decreasing the bias. We explicitly rule out current formulations of the blocking-state model and the polaron model as explanations for our experimental observations and suggest that a full model requires a more detailed account

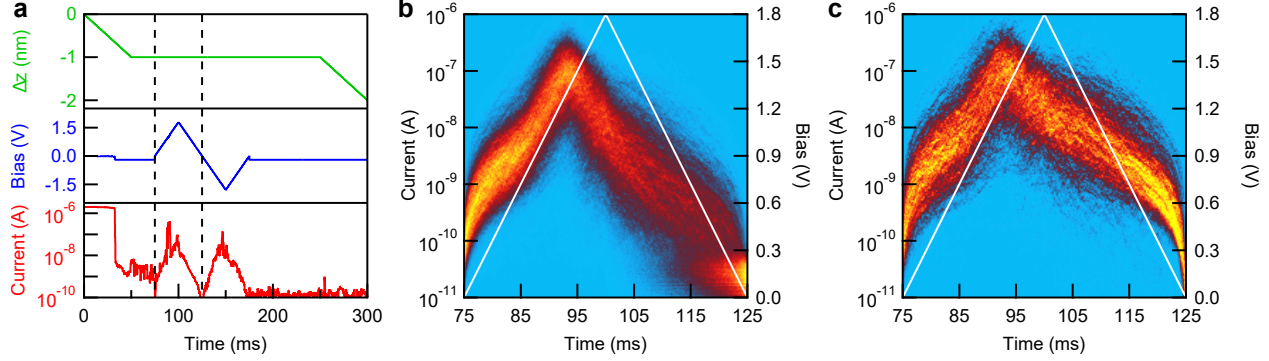


Figure 4.2: (a) Sample current and voltage ( $I$ - $V$ ) trace of a TDO4 junction measured in TCB. Displacement trace shown in green. Vertical lines delineate data used to produce (b) and (c). (b) 2D current-time histogram of over 3000 selected traces showing junction rupture at around 1.5 V for most traces. (c) 2D current-time histogram of over 500 selected traces demonstrating reproducible NDR and hysteresis. The applied bias overlaid in white.

of inelastic charge hopping and the time-scale of intra-molecule reorganization.

### 4.3 Current-Voltage Measurements

We used the STM-BJ technique described in Section 1.4. To explore transport in the resonant tunneling regime, we modified the STM-BJ technique to obtain an  $I$ - $V$  curve of each molecular junction. As described previously, the molecular junction is held for 100 ms, during which time the current is measured as the voltage is ramped up and down [6, 257]. An example current and voltage trace, along with the displacement of the substrate over time, is shown in Figure 4.2a. Thousands of traces are typically collected and analyzed.

The result from an  $I$ - $V$  experiment for junctions of TDO4 in a solution of 1,2,4-Trichlorobenzene (TCB) is shown as a 2D current-time histogram in Figure 4.2b, where we have selected those traces with molecular signatures and show only half of the voltage ramp. The voltage was ramped from 0 to 1.8 V and back down over the course of 50 ms. During the ramp up, the current follows a curve characteristic of single-level charge transport up to approximately 1.5 V, after which many junctions rupture as indicated by the decrease in color intensity. In Figure 4.2c, we select the  $\sim$ 500 traces that do not rupture. In these traces, the current decreases after 1.5 V, even as the bias is increased further. In other words, the junctions display NDR-like behavior. Furthermore, the current

displays hysteresis, following a different path during the ramp down compared to the ramp up. We also collected analogous data for squaraine, shown in Figure 4.10e, with very similar results.

#### 4.4 Curve-Fitting

To acquire a more detailed account of the underlying mechanism for the observed NDR and hysteresis, we performed nonlinear least-squares fitting to the  $I$ - $V$  data using the Landauer-Büttiker formalism described in Section 1.1. We reproduce the formula for the current in Eq 4.1. Although this level of theory cannot capture NDR and hysteresis, it is a reasonable approximation when the transport is dominated by coherent single-electron tunneling. Our experimental results suggest that this is indeed the case for small biases, before the NDR feature appears.

$$I(V) = \frac{2e}{h} \int_{-\infty}^{\infty} dE T(E) \left[ f_L \left( E - \frac{eV}{2} \right) - f_R \left( E + \frac{eV}{2} \right) \right] \quad (4.1)$$

In the simplest case, a single molecular orbital dominates transport in the junction. We have shown in previous work that in the case of TDO4, this is the Lowest Unoccupied Molecular Orbital (LUMO) [40, 258], and the same reasoning is applied to squaraine to infer that the Highest Occupied Molecular Orbital (HOMO) dominates transport (Fig 4.10i). This is also confirmed by Density Functional Theory (DFT)-based transport calculations (Section 4.8.6). For this reason, we say that electrons (holes) dominate transport in TDO4 (squaraine) or, equivalently, that TDO4 is LUMO-conducting and squaraine is HOMO-conducting. The transmission function can then be approximated using the single-level model introduced in Section 1.1.

$$T(E) = \frac{\Gamma^2}{(E - \varepsilon)^2 + \Gamma^2} \quad (4.2)$$

In fitting  $I$ - $V$  data to the coherent transport model, we use the Fermi-Dirac distribution at room-temperature instead of taking the low temperature approximation. This is necessary in order to capture the more gradual increase in current near resonance at room temperature. To compensate for the increase in computational complexity, we only fit 200 points per junction, which is 20% of

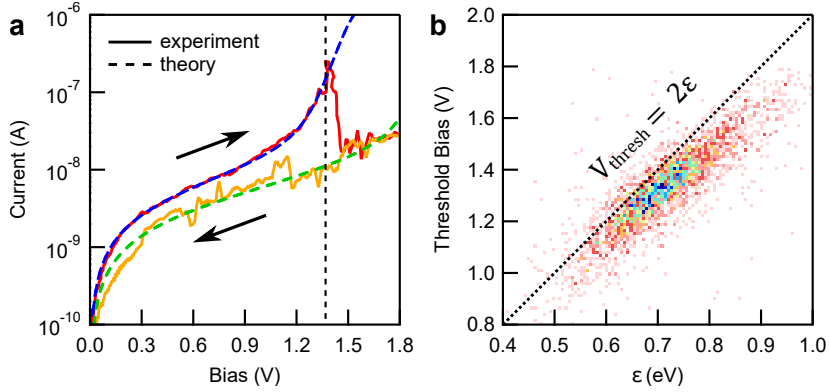


Figure 4.3: Analysis of TDO4 junctions measured in TCB. (a) Sample  $I$ - $V$  trace with forward bias sweep in red and backward bias sweep in orange. Fits to single-level model within the Landauer-Büttiker formalism overlaid in dashed blue and green for forward and backward bias sweeps, respectively. The threshold bias as determined by locating the maximum current is indicated by the vertical dashed line. The black arrows indicate the sweep direction. (b) Threshold bias and level alignment ( $\varepsilon$ ) correlation histogram for traces that either rupture or sustain (i.e. data in Fig 4.2b). Dotted line represents bias at which the transport level enters the bias window.

the total data available. We also fit  $\log_{10}(I)$  instead of  $I$  as a function of bias to give points at all biases equal weight, since the current spans over three orders of magnitude. The fitting algorithm is described in full in Section 4.8.4.

An exemplary  $I$ - $V$  trace is shown in solid colors on a semi-log plot in Figure 4.3a, where the ramp up is drawn in red and the ramp down is drawn in orange. The NDR feature, seen during the ramp up, is abrupt, which is not obvious in Figure 4.2c. We identify the threshold bias at which NDR occurs (dashed vertical line in Fig 4.3a) by selecting the point of maximum current. By fitting the curve up to the threshold bias to the coherent transport model given in Eq 4.1, we extract  $\varepsilon$  and  $\Gamma$ . We plot the threshold bias against the fitted  $\varepsilon$  in the 2D correlation histogram shown in Figure 4.3b for the junctions contained in Figure 4.2b (i.e. including those junctions that rupture). Not only is there a strong correlation between the threshold bias and  $\varepsilon$ , but, with few exceptions, the threshold bias is always just below  $2\varepsilon$ . The significance of this becomes clear upon closer inspection of Eq 4.1. Because the bias window opens symmetrically about the Fermi energy, in the limit of  $T = 0$ ,  $V = 2\varepsilon$  is the condition necessary for achieving resonant transport. From the strong correlation between threshold bias and  $\varepsilon$ , we infer that charging the molecular orbital that

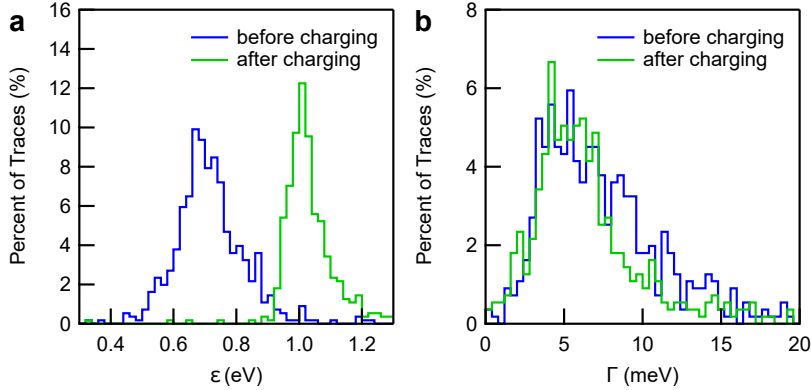


Figure 4.4: Histograms of fitted (a) level alignment  $\varepsilon$  and (d) level broadening  $\Gamma$ , with the results before and after charging shown in blue and green, respectively.

dominates transport induces the NDR. In the case of TDO4, this corresponds to the molecule being reduced, whereas for squaraine, it is oxidized.

Upon charging, the junctions either rupture or sustain, and we find that approximately 20% of junctions found in Figure 4.2b sustain. From these junctions, we can extract a peak-to-valley ratio for each trace, which is around 10 for most junctions but can be as high as 200 (Fig 4.9b). In addition, we also fit the  $I$ - $V$  on the return bias sweep to the single-level coherent transport model. We emphasize that this fitting assumes coherence and, therefore, only represents models where coherent tunneling is preserved upon charging. The fitted values for  $\varepsilon$  and  $\Gamma$  before and after charging are summarized in the histograms in Figure 4.4. The mean value of  $\varepsilon$  increases by around 0.3 eV, whereas any change in  $\Gamma$  is negligible. Both the NDR and hysteresis, therefore, clearly result from an increase in  $\varepsilon$ , at least within a coherent tunneling model. The same qualitative behavior is observed for squaraine in TCB, as shown in Figure 4.10g,h.

To test if the solvent environment alters these results, we repeated the experiment in propylene carbonate (PC). As described in previous work, STM-BJ measurements performed in polar solvents like PC utilize a tip coated with an insulating layer in order to reduce capacitive and Faradaic background currents [259]. Because the surface area of the tip is much smaller than the surface area of the substrate, the density of the electric double layer is asymmetric, resulting in junctions that rectify according to the dominant transport orbital. More explicitly, in the limit that the electric double layer is much denser at the tip than at the substrate, the voltage drops almost entirely across

the tip-molecule interface. We model this effect as a linear dependence of  $\varepsilon$  on the applied bias, i.e. we replace  $\varepsilon$  in Eq 4.2 with  $\varepsilon(V) = \varepsilon_0 + \alpha eV$ . The effect of the solvent is parameterized by  $\alpha$ , which ranges from 0 (in the case of a non-polar solvent) to 0.5 (for the case where the molecular orbital is completely pinned to the substrate). Although we had previously concluded that  $\alpha$  was 0.5 [40], this conclusion was derived from a zero-temperature approximation. The present work shows that  $\alpha$  can vary from junction to junction when considering that measurements are at 300 K and is therefore used as a third fitting parameter. We extract  $\varepsilon$  and  $\Gamma$  before and after charging for TDO4 and squaraine in PC as shown in Figures 4.10a-d and 4.10i-l, respectively. Again,  $\varepsilon$  increases upon charging, accompanied by a small change in  $\Gamma$ . Furthermore, the peak-to-valley ratio is even higher in PC than in TCB and is easily on the order of 100.

## 4.5 Charging Dynamics

We obtain greater insight into the mechanism for charging by changing the bias ramp speed. We repeat the experiment depicted in Figure 4.2a, changing only the duration over which the bias is ramped. The result for squaraine in PC is shown in Figure 4.5a. At slow speeds, the threshold bias is consistently around  $0.5 \pm 0.1$  V. The large spread of values accounts for variations in  $\varepsilon$ . As the speed increases, the threshold bias increases logarithmically with ramp speed. We infer from this trend that the charging event is stochastic in nature. Assuming that the probability of charging the molecule increases the closer the bias is to the resonant tunneling condition, only at sufficiently slow ramp speeds is there enough time for the molecule to charge at lower bias.

We then repeated the same experiment in TCB. To compare the two experiments, we calculate the “normalized” threshold bias rather than the actual threshold bias. To normalize, we divide the measured threshold bias by the bias at which the resonance of the transmission function is expected to enter the bias window, given by Eq 4.3.

$$V_{\text{resonance}} = \frac{\varepsilon}{\alpha + \frac{1}{2}} \quad (4.3)$$

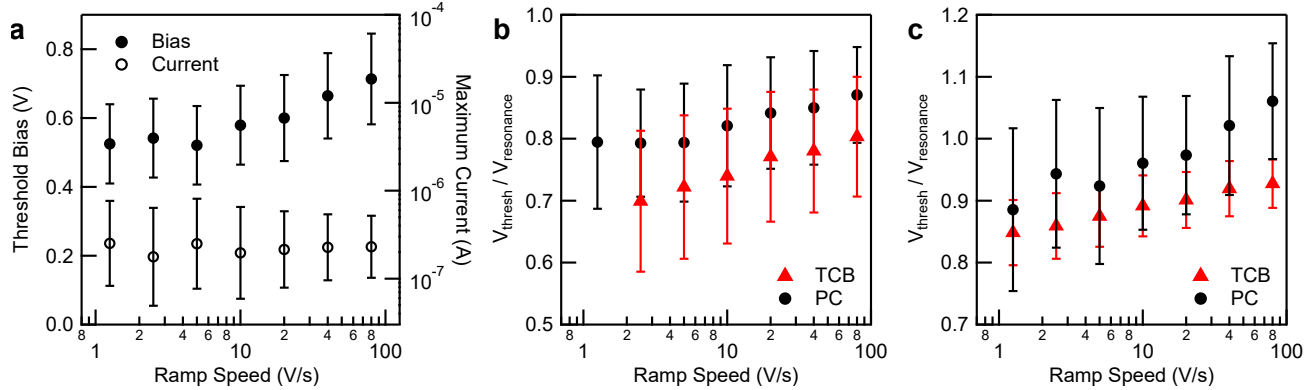


Figure 4.5: (a) Threshold bias as a function of ramp speed for squaraine junctions measured in PC. Error bars depict the standard deviation of threshold bias values. Normalized threshold bias as function of ramp speed for (b) squaraine and (c) TDO4 junctions measured in non-polar (TCB) and polar (PC) solvents.

Note that this normalization is performed for each trace based on the fitted values of  $\varepsilon$  and  $\alpha$ .  $\alpha$  is fixed at 0 for junctions in non-polar solvent. The dependence of the normalized threshold bias on the bias ramp speed for squaraine in both solvents is shown in Figure 4.5b. In both solvents, the threshold bias increases logarithmically with the bias ramp speed. The same behavior is observed for TDO4 (Fig 4.5c).

Finally, we investigate whether the shift in level alignment, which we attribute to a charging event, can be reversed by discharging the molecule. We begin by simply adding a second  $I$ - $V$  sweep following the first, and we find that most junctions (collected in Fig 4.6a) display a second NDR feature, thus ruling out any irreversible chemical reactions. To explore the kinetics further, we designed a modified STM-BJ experiment as depicted for squaraine junctions in PC in Figure 4.6b. The experiment starts with a ramp up to 1 V in order to charge the molecule, with the ramp speed fixed at 20 V/s. The bias is then ramped down to some hold bias over the course of 50 ms. This bias is then maintained for some time before the bias is again ramped up to 1 V. Since we know that the ramp speed can affect the charging statistics, this second ramp is also performed at 20 V/s. Lastly, the bias is ramped down to 0 V, also at a 20 V/s rate. By varying the hold bias and hold time, we control the likelihood that the molecule reverts to the neutral state.

The experiments are analyzed as follows: first, we select for traces that sustain a molecular

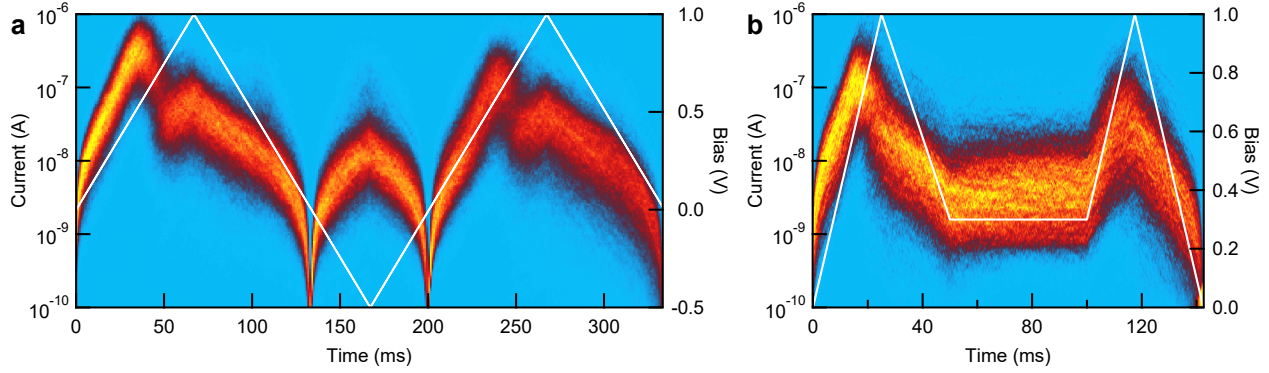


Figure 4.6: (a) 2D current-time histogram of over 2000 selected traces from experiment with two sequential bias sweeps, overlaid in white, from  $-0.5$  to  $1.0$  V. NDR and hysteresis are repeated in second bias sweep, indicating that the molecule discharges. (b) 2D current-time histogram of custom experiment testing stability of charged state. Applied bias overlaid in white. Both measurements are of squaraine junctions in PC.

junction to the end of the bias hold (100 ms in Fig 4.6b). Next, we select those traces which display hysteresis after the first ramp. Such traces also typically display NDR. Of these traces, we select those that display a second hysteresis feature after the second ramp to 1 V. Because a second hysteresis feature is only expected of those molecules that return to the neutral state, we infer that these junctions have reversed their charge state during the hold. In this way, we measured the percent of junctions that discharge as a function of hold bias and hold time.

Figure 4.7 shows the dependence of the reversibility on the hold bias and the hold time. In Figure 4.7a, the hold time is kept fixed at 100 ms as the hold bias is varied. As the hold bias increases, the number of junctions which reverse decreases, suggesting that the charged state can be sustained under a high bias. Below a hold bias of around 0.4 V, the reversibility plateaus. This means that to discharge the molecule, the bias must be sufficiently far from the resonant tunneling condition, but the rate of discharge does not increase below a certain threshold bias. In Figure 4.7b, the hold bias is set to 0.3 V as the hold time is varied. This bias is deliberately chosen to be just below where the bias dependence becomes negligible. As the hold time increases, the percent of junctions which reverse increases logarithmically, indicating that discharging, like charging, is a stochastic process. Again, these results are reproduced for squaraine in TCB and for TDO4 (Fig 4.11).

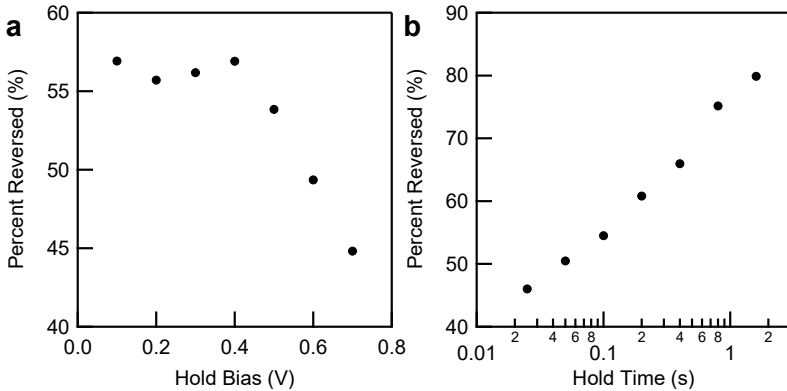


Figure 4.7: Percent of junctions reversed as a function of (a) hold bias and (b) hold time.

## 4.6 Theoretical Discussion

Before analyzing these results based on existing theories, we briefly summarize the key observations that must be explained. (A) Charging the molecular orbital which dominates transports results in an abrupt drop in current. (B) Many junctions are lost upon charging, indicating significant coupling to nuclear degrees of freedom. (C) Insofar as the charged system can be characterized by a single-level model within the Landauer-Büttiker formalism, the level of the charged system moves further away from Fermi, whereas the change in level broadening, if any, is small compared to variance. (D) Both charging and discharging are not driven solely by bias but occur stochastically, with 100 ms timescale kinetics.

We first consider applying the blocking-state model to our results [252–254]. This model, shown in Figure 4.8a, assumes that an electronic level which does not contribute significantly to transport (LUMO+1 in the Fig 4.8a) is occupied at high bias. Occupation of this higher level shifts the alignment of the transport level (LUMO in this case) away from the Fermi energy due to Coulomb interactions, which can be captured by a Hubbard-like parameter  $U$ . The condition for NDR in this model is that the higher level be weakly coupled to the electrodes compared to the coupling of the transport level. By contrast, in our experiments, we find that NDR occurs upon charging of the level that dominates transport (Fig 4.3b), not a second, weakly coupled orbital. Furthermore, DFT-based transport calculations of TDO4 junctions do not show higher-energy levels

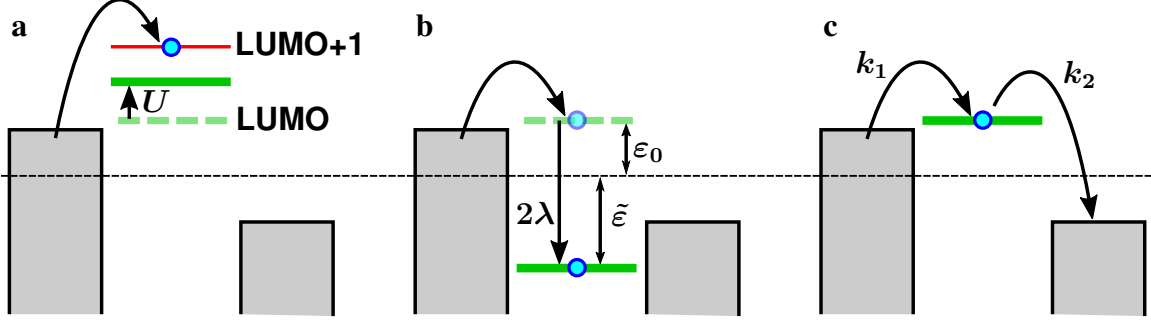


Figure 4.8: Models for simultaneous NDR and hysteresis represented as energy-level diagrams. Electrodes are drawn as a continuous density of states filled up to the chemical potential. Single-electron levels are drawn as horizontal lines, with dashed (solid) lines indicating the levels before (after) charging and vertical arrows indicating the level dynamics upon charging. Charging of the level suggested by arched arrows from the left electrode to the electronic level. All models are depicted for LUMO conducting systems. (a) Blocking-state model: LUMO+1 is poorly coupled to the electrodes, whereas LUMO is well coupled to the electrodes. Upon charging LUMO+1, LUMO shifts up by  $U$ , the Coulomb charging energy, resulting in a drop in current. (b) Polaron model: upon charging the LUMO, the charge on the molecule is stabilized by both nuclear motion and the solvent environment, parameterized by the reorganization energy  $\lambda$ . The level moves down such that the charged level is further from Fermi than the empty level, resulting in a drop in current.  $\varepsilon_0$  and  $\tilde{\varepsilon}$  are the level alignment before and after charging, respectively. (c) Sequential tunneling: due to strong interaction with molecular vibrations and the environment, electrons no longer tunnel elastically. In the context of Marcus charge transfer, sequential tunneling is modelled by the charge transfer rates  $k_1$  and  $k_2$  for transfer to and from the molecule, respectively. Charge transfer in the opposite direction is omitted for clarity.

with significantly weaker coupling as required by this model [40].

The second model we consider is the polaron mean-field model, advanced by Galperin and co-workers [255, 256], which is depicted in Figure 4.8b. According to this model, transport involves a single electronic level whose coupling to phonon modes stabilizes the charge on the molecule. In a non-polar solvent environment, where the bias falls symmetrically across the substrate- and tip-molecule interfaces, NDR occurs if the reorganization energy,  $\lambda$ , is greater than  $\varepsilon$  such that the charged level is further from the Fermi energy than the neutral level. In order to discharge the level, the bias polarity must be either increased further or reversed. In our measurements, however, we observe that the junction discharges even without further increasing or reversing the bias polarity. In a non-polar solvent, the polaron model is consistent with this result only if  $\lambda$  is smaller than  $\varepsilon$ , which is incompatible with NDR as the charged level would then be closer to the Fermi energy,

resulting in an increase in current upon charging.

We obtain further evidence against the polaron model by a more careful analysis of the data measured in the polar solvent. The fitting applied to measurements in PC summarized in Figure 4.10 implicitly assumed a blocking-state-like model. This is because the fitting applied there required that TDO4 (squaraine) remain LUMO (HOMO) conducting upon charging. In the polaron model, however, the observation of NDR implies that a LUMO-conducting molecule becomes HOMO-conducting upon charging and vice versa. After correcting the fitting to apply to the polaron model (Fig 4.17), the reorganization energy  $\lambda$  can be calculated using the relation  $2\lambda = |\tilde{\varepsilon} - \varepsilon_0|$ , where  $\varepsilon_0$  and  $\tilde{\varepsilon}$  are the level alignment before and after charging, respectively (Fig 4.8b). Surprisingly, the results from this calculation imply that  $\lambda$  is smaller in PC than in TCB despite PC being significantly more polar (Section 4.8.5). This is counterintuitive, since polar solvents are expected to better screen the charge and, consequently, result in a larger reorganization energy than non-polar solvents [260–262]. Since this result derives directly from imposing a simple polaron model, we conclude that this model, at least in its current formulation, cannot explain our experimental results.

In principle, the polaron model can be modified by introducing a second transport channel. The reorganization energy would then cause the frontier orbital to drop out of transport bias window, allowing the second channel to dominate transport. Although we cannot entirely rule out such a model, we suspect that such a model would be extremely sensitive to the exact reorganization energies and level alignment. Furthermore, such a model would violate the Aufbau principle, which is unlikely for conjugated organic molecules without highly localized molecular orbitals [253, 254] or radical character [263]. We also note briefly that there are a class of theories which explain NDR by biased-induced deformation of the molecular orbitals that, in turn, result in changes in the level broadening [234, 245, 264, 265]. Similarly, theories which implicate charge-induced conformational change [266, 267] also manifest as decreases in level broadening [268, 269]. However, bias-induced orbital deformation predicts more gradual NDR than is observed here, and curve-fitting does not show any consistent change in level broadening.

Instead, we interpret our observations as a transition from predominately coherent tunneling, as described by the Landauer-Büttiker model, to sequential tunneling where inelastic processes damp the current in the resonant tunneling regime. Theoretical work exploring this transition has shown that the introduction of incoherence decreases the transmission through a single level at resonance [100, 270, 271]. Our results demonstrate, however, that the transition from coherent to sequential tunneling is abrupt even at room temperature and that the relevant timescales are long, at least compared to the characteristic timescales of molecular motion. We propose that advances in theories incorporating Marcus charge transfer rates and its possible extensions, where the reorganization energy asymmetrically affects charge transfer to and from the molecule ( $k_1$  and  $k_2$ , respectively in Fig 4.8c), may account for this extraordinary result [272, 273]. We reemphasize that the  $I$ - $V$  curve-fitting during the reverse bias sweep using the Landauer-Büttiker formalism as performed in our analysis is only valid within the context of coherent tunneling and should only be used to evaluate models where this is applicable. Consequently, a model of incoherent tunneling will not be constrained to the interpretation presented in Figure 4.4 of level alignment shift, and a blocking-state or polaron-like model that relaxes the assumptions stated in the preceding paragraphs may still provide a good foundation for exploration [274]. This will be the subject of future investigations and is beyond the scope of this work.

## 4.7 Conclusion

To conclude, we have explored the rich phenomena that occur in the resonant tunneling regime. First, we have shown that the widely ignored junction rupture at high bias is not entirely impervious to study and is directly attributable to redox events. Furthermore, junctions that do not rupture display highly reproducible and pronounced NDR and hysteresis with kinetic timescales on the order of 100 ms. We argue that existing models cannot describe our results and suggest that a deeper understanding of the interplay between molecular reorganization rates and both coherent and incoherent tunneling is the key to resolving the mystery. Finally, this work opens the possibility of a new mode of operation of single-molecule devices at high bias to achieve highly nonlinear

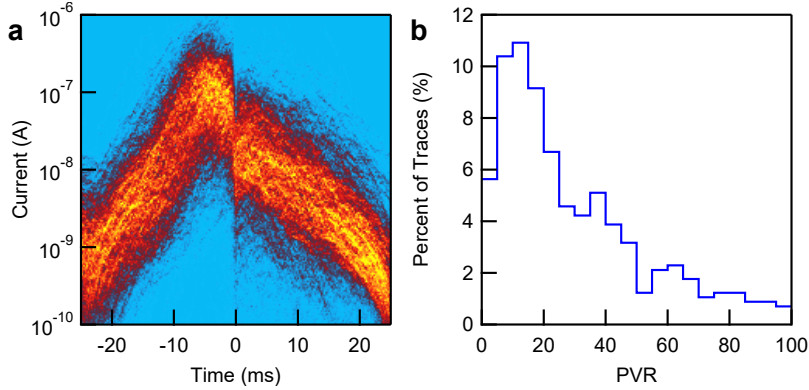


Figure 4.9: (a) Data presented in Figure 4.2c, with each trace offset horizontally such that the drop in current occurs at  $t = 0$ . (b) Histogram of the peak-to-valley ratio extracted from each trace.

behavior even at room temperature.

## 4.8 Supplementary Information

### 4.8.1 Additional Data

Most of the  $I$ - $V$  traces display abrupt NDR. However, this is not visible in Figure 4.2c as the location of the NDR is not the same in every  $I$ - $V$  curve. Figure 4.9a shows a 2D histogram where each  $I$ - $V$  trace is aligned relative to the time where the current is minimum after the threshold bias (which is the bias where the maximum current occurs). This figure demonstrates how sharp the current drops beyond the threshold bias. Although there are certainly some traces which display more gradual NDR, the current drops by a factor of 10 on a few millisecond time scale for most traces. The peak-to-valley current ratio of each trace is extracted from the data by taking the ratio of the current at the threshold bias (i.e. the maximum current in the trace) and the minimum current after the threshold bias. This is shown in Figure 4.9b.

Data collected from TDO4 junctions measured in PC and squaraine junctions measured in TCB and PC are summarized in Figure 4.10. For each measurement, we provide the 2D current-time histogram, the  $V_{\text{thresh}}-\varepsilon$  correlation histogram, and the histograms of the fitted  $\varepsilon$  and  $\Gamma$ . Only the  $V_{\text{thresh}}-\varepsilon$  correlation histograms contain data for junctions that rupture; the rest contain only data for junctions that sustain. For measurements in polar solvent, the correlation histograms include two

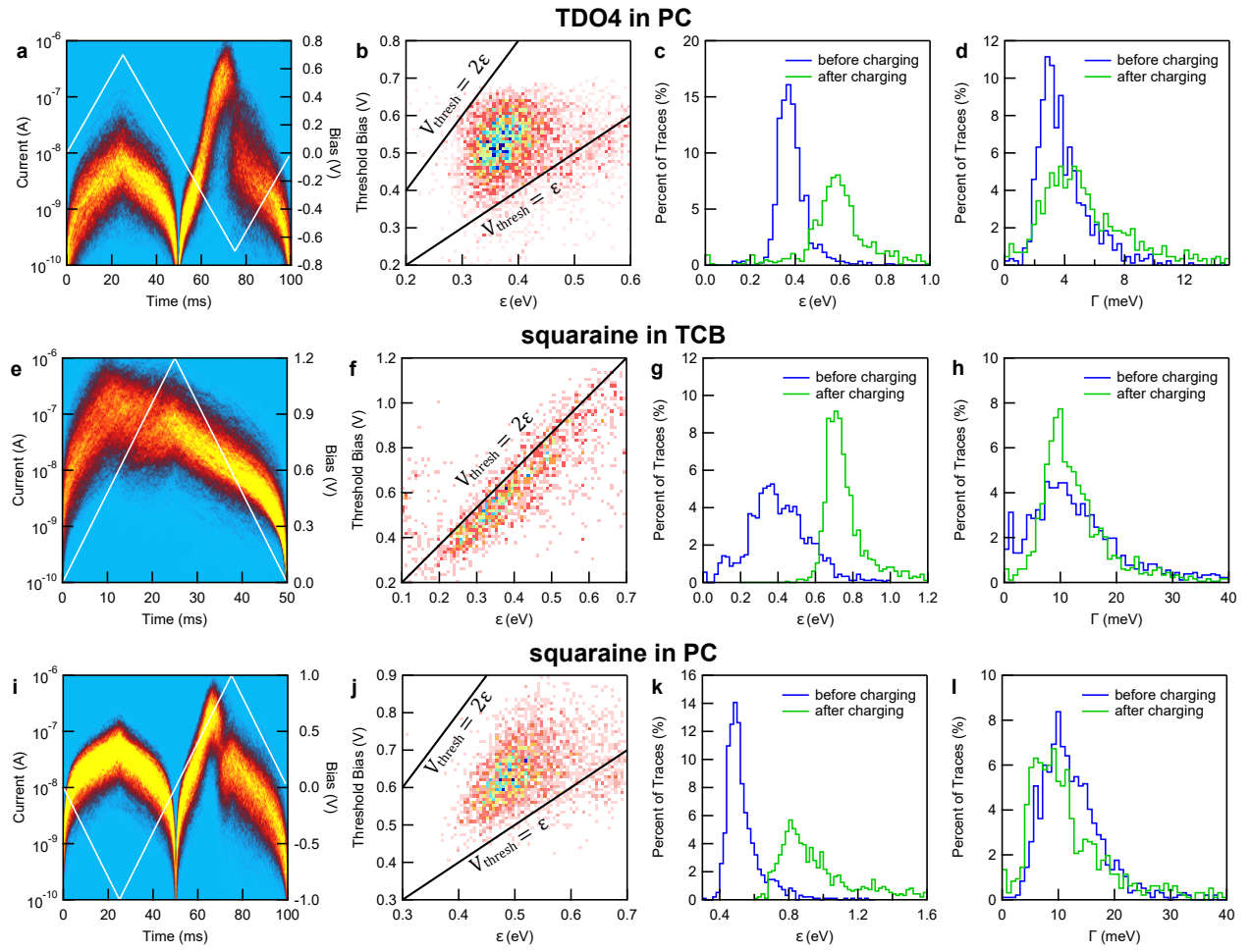


Figure 4.10: 2D current-time histograms (a, e, i),  $V_{\text{thresh}} - \epsilon$  correlation histograms (b, f, j),  $\epsilon$  histograms (c, g, k), and  $\Gamma$  histograms (d, h, l) for TDO4 junctions in PC (a, b, c, d), squaraine junctions in TCB (e, f, g, h), and squaraine junctions in PC (i, j, k, l).

diagonal lines that delineate the expected trend in a non-polar solvent ( $V_{\text{thresh}} = 2\epsilon$ ) or a perfectly effective polar-solvent where the level alignment is pinned to the substrate ( $V_{\text{thresh}} = \epsilon$ ). The data falls between the two lines. In addition, the 2D current-time histograms for measurements performed in polar solvent show both the positive and negative voltage ramps. The current is higher when the bias is positive (negative) for squaraine (TDO4) junctions, indicating that the HOMO (LUMO) orbital is closest to Fermi.

Figure 4.11 summarizes the results for the reversibility experiments for squaraine and TDO4 junctions in TCB and PC. Interestingly, the charged state of squaraine appears less stable in PC than in TCB as indicated by a higher reversibility in Figure 4.11a,b. We hypothesize that this is due

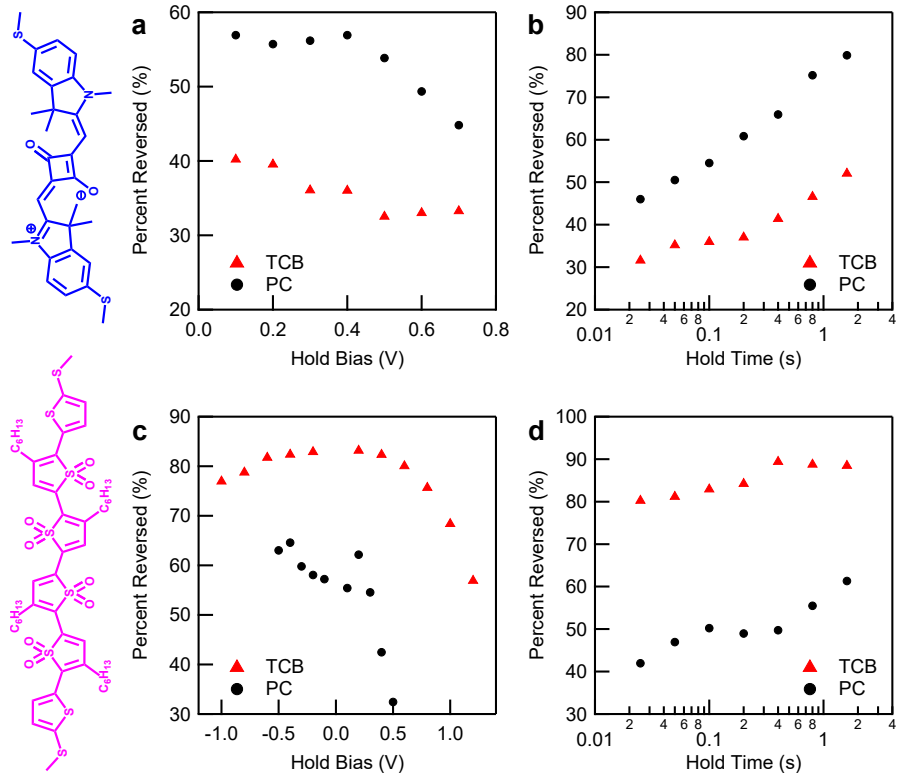


Figure 4.11: Percent reversed versus (a) hold bias and (b) hold time for squaraine junctions measured in TCB (red triangles) and PC (black circles). (c) and (d) are the corresponding experiments for TDO4 junctions.

the presence of water in PC which can protonate the molecule. Protonation serves as an additional driving force for discharging not present in TCB.

#### 4.8.2 Selection Algorithm for $I$ - $V$ Data

**Initial Selection:** Just before the  $I$ - $V$  ramp is performed (at 75 ms in Fig 4.12d), the bias is held fixed and the conductance is measured. If the conductance matches the expected conductance of the molecule, the trace is selected for further analysis. The results from this initial selection are displayed in Figure 4.12a.

**Hysteresis Test:** Due to the junction-to-junction variation in level alignment, not all junctions enter the resonant-tunneling regime within the maximum applied bias. Assuming that all junctions that enter the resonant-tunneling regime have a lower current during the return bias sweep due to junction rupture or hysteresis, we select traces that undergo charging by comparing the current

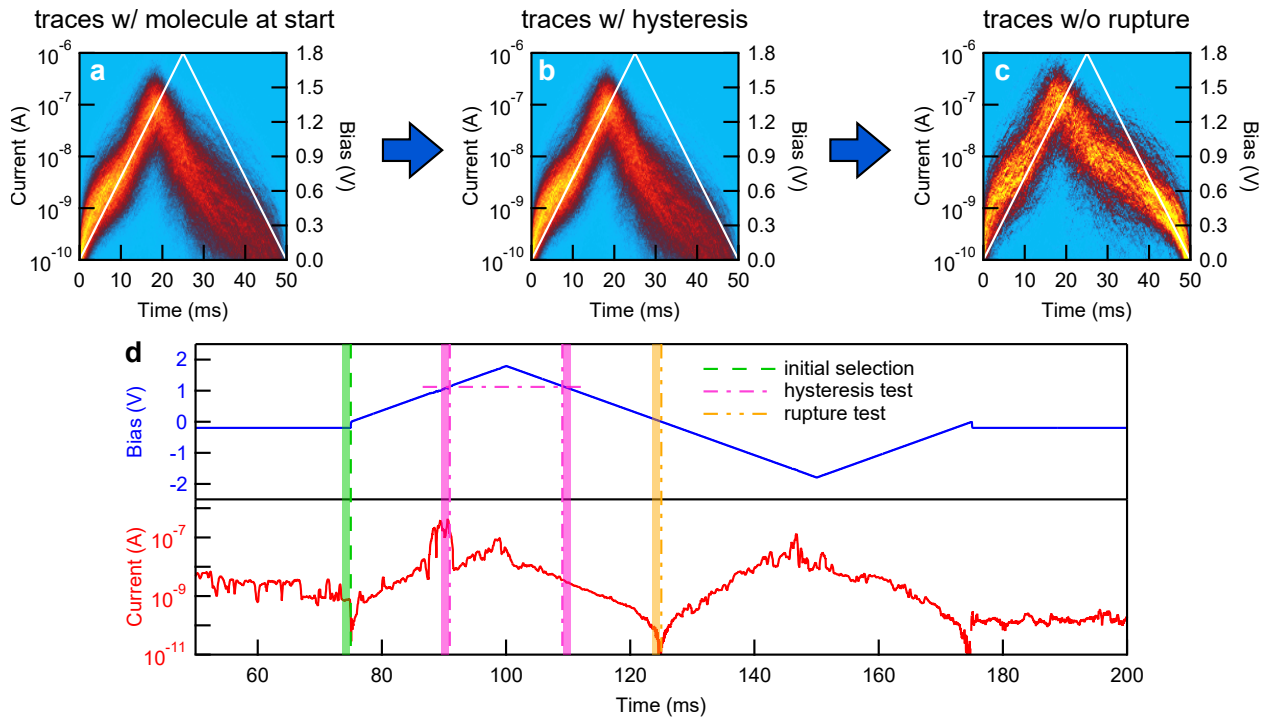


Figure 4.12: 2D current-time histograms after (a) initial selection, (b) hysteresis test, and (c) rupture test. (d) Example trace (same as Figure 4.3a), zoomed in to highlight features used in selection algorithms. Each algorithm looks for specific features in the current at different points in time in the trace, indicated by the vertical lines. The initial selection (green) checks for the presence of the molecule. The hysteresis test (magenta) checks that the molecule has been charged. The rupture test (orange) distinguishes junctions that rupture upon charging from junctions that sustain.

at the threshold bias during the ramp up and during the ramp down. Specifically, we compare the average current for 50 points before the threshold bias during the ramp up (increasing bias) to the 50 points after the threshold bias during the ramp down (decreasing bias). If the difference between the two currents is at least half a decade, the trace is labeled as having entered the resonant-tunneling regime. Recall that the threshold bias is approximated as the bias where the maximum current occurs. If the maximum bias is sufficiently large, most junctions will display hysteresis or junction rupture. The results after this selection are shown in Figure 4.12b.

**Rupture Test:** To distinguish those junctions which display true hysteresis from those that rupture, we consider the points at the very end of the downward ramp (at 125 ms in Fig 4.12d). Junctions that rupture have a current at the instrument noise even for biases as high as 0.1 V. At instrument noise, the polarity of the current will oscillate between positive and negative. By

Table 4.1: Number of traces after each selection algorithm

Molecule	Solvent	Total	Initial	w/ Hysteresis	w/o Rupture	Post-Fit
TDO4	TCB	5,000	3,378	3,030	568	461
TDO4	PC	50,000	7,829	5,721	1,310	843
squaraine	TCB	21,000	10,660	8,958	1,913	1,638
squaraine	PC	5,000	3,550	3,387	1,504	957

rejecting those traces where the current and bias have opposite polarity close to zero bias, we are left with the traces that show true hysteresis. The results from this final selection is shown in Figure 4.12c.

**Polar Solvent:** Fitting data collected in polar solvent requires acquiring data at both bias polarities. The initial selection algorithm is identical to that for experiments performed in non-polar solvent except one additional requirement. In addition to selecting for those traces that display the expected conductance before the voltage ramp, we reject those traces which fail the rupture test where the bias changes polarity (at 50 ms in Fig 4.10a). This is to reject traces that display strong capacitive back-current.

**Post-Fit Selection:** The majority of traces before charging can be characterized through non-linear least-squares regression, as described in Section 4.8.4. A fraction of traces will return unrealistic values for the level alignment and/or level broadening for the fitting after charging. This is due to false negatives from the rupture test, i.e. junctions that actually rupture but pass the rupture test. This problem is worse for experiments performed in polar solvent compared to those performed in non-polar solvent. We reject those traces where one of the fitting parameters equals the constraint. We also reject those traces with level alignment greater than 10 eV or level broadening greater than 1 eV. The histograms of the fitted values of level alignment and level broadening are constructed out of traces after this selection algorithm has been applied. Without this selection, the qualitative behavior of the histograms is the same.

The number of traces after each selection process is summarized in Table 4.1.

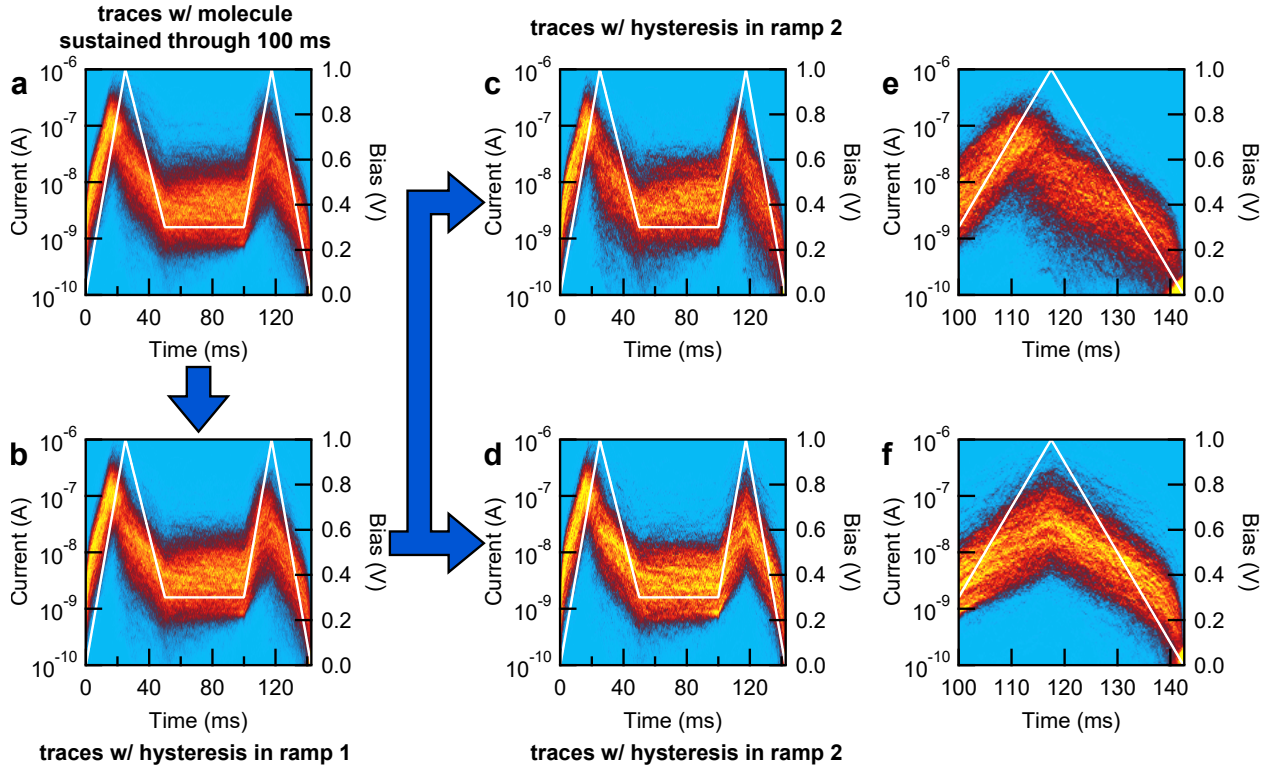


Figure 4.13: 2D current-time histograms after (a) initial selection and (b) hysteresis test in ramp 1. The traces which display hysteresis in ramp 2 (i.e. those traces that reverse) and the traces which do not display hysteresis in ramp 2 are compiled in (c) and (d), respectively. The same data is presented in (e) and (f) to highlight the efficacy of the hysteresis test.

#### 4.8.3 Reversibility Experiment

Figure 4.13 demonstrates the selection algorithm for the reversibility tests on squaraine in PC. The initial selection is the same except that the rupture test is applied just before the second ramp. In addition to the standard rupture test, we check that the current is greater than instrument noise. The hysteresis test for both ramps is the same as described in Section 4.8.2. The rupture test is not performed after the second ramp, since junctions that rupture due to charging still count as reversed. Figure 4.13e,f shows the same data as in Figure 4.13c,d but zoomed in to highlight the second ramp and demonstrate the efficacy of the hysteresis test.

#### 4.8.4 Curve Fitting

Before fitting, the data is processed as follows: First, the current and voltage trace is loaded and the appropriate  $I$ - $V$  data is extracted. For example, for experiments performed in non-polar solvent, only the initial ramp up to the threshold bias is required. For experiments performed in polar solvent, the middle ramp where the bias sweeps the entire range is selected, not including points past the threshold bias. If the data after charging is being fit, the entire reverse ramp is selected. The current data is converted to log(current) data by multiplying the sign of the voltage at each data point before applying the base 10 logarithmic function, i.e.  $\log_{10}(I) \equiv \log_{10}(I \cdot \text{sign}(V))$ . There may still be some points where the sign of current does not match the sign of the voltage; these points are removed. The remaining points are then smoothed using a boxcar smoothing algorithm (unweighted sliding-average) with a box width of 11 points. This step minimizes the number of outliers. Before fitting the data, the number of points is reduced to 200, with points being selected evenly from the remaining data. All fitting is performed using Levenberg-Marquardt least-squares method as implemented in Igor Pro Version 6.3.7.2.

Many works in the past that have performed  $I$ - $V$  fitting on room-temperature based single-molecule junction measurements do so within the 0 K approximation, where the Fermi-Dirac distributions are replaced with step functions [5, 40, 234, 275–278]. In the special case where the transmission function can be approximated with the single-level model, the current can be computed analytically without performing numerical integration (Eq 4.4 below). Although this is a reasonable approximation in the non-resonant tunneling regime, as the bias approaches  $2\varepsilon$ , the theoretical current deviates significantly from the low-temperature approximation, as demonstrated in Figure 4.14a. As a rule of thumb, if the bias exceeds  $\varepsilon$ , temperature must be taken into account and one must perform numerical integration. The requirement would be more stringent for experiments

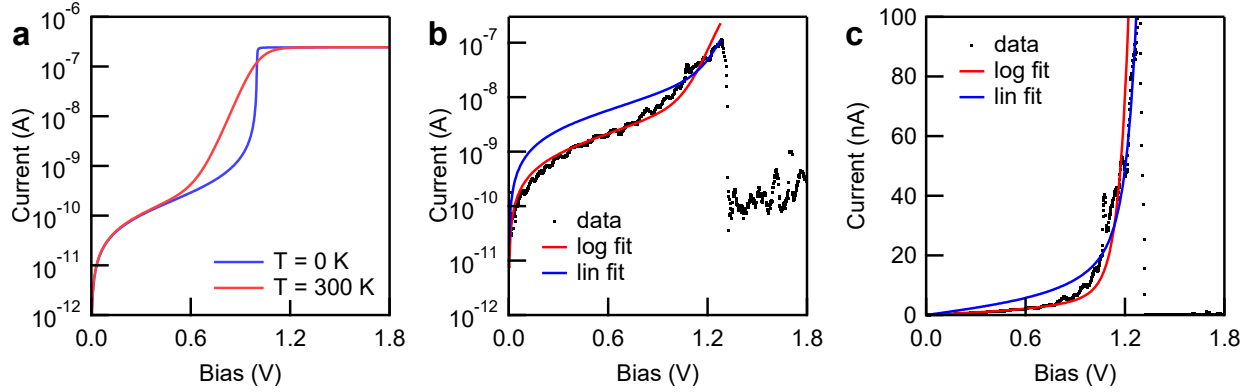


Figure 4.14: (a) Theoretical  $I$ - $V$  curves generated using Eq 4.4 (blue) and Eq 4.1 (red). Example  $I$ - $V$  data (black dots) with fits from logarithmically-scaled data (red) and linearly-scaled data (blue), displayed on a (b) semi-log plot and (c) linear plot.

performed in polar solvent.

$$\lim_{T \rightarrow 0} I(V) = \frac{2e}{h} \int_{-eV/2}^{eV/2} dE T(E) = \frac{2e\Gamma}{h} \left[ \tan^{-1} \left( \frac{V - 2\varepsilon}{2\Gamma} \right) + \tan^{-1} \left( \frac{V + 2\varepsilon}{2\Gamma} \right) \right] \quad (4.4)$$

In addition, since the current can span three orders of magnitude when approaching the resonant tunneling regime, all fitting is done on a logarithmic scale, as using a linear scale fit results in systematic errors at low bias. This is illustrated in Figure 4.14b,c.

The effect of polar solvent can be captured by a modified transmission function, given by Eq 4.5, where  $0 \leq \alpha \leq 0.5$ . The primary effect of the additional parameter is to introduce an asymmetry in the  $I$ - $V$  curve [40]. In order to perform fitting without fixing  $\alpha$ , data at both bias polarities must be collected. This is shown in Figure 4.10a,i. This asymmetry also allows us to determine whether the molecular orbital dominating transport is the HOMO or LUMO. If the current is higher at positive (negative) bias, the molecule is HOMO (LUMO) conducting.

$$T(E) = \frac{\Gamma^2}{(E - \varepsilon - \alpha eV)^2 + \Gamma^2} \quad (4.5)$$

When fitting the I-V curve after charging, only data at one bias polarity is available. In order

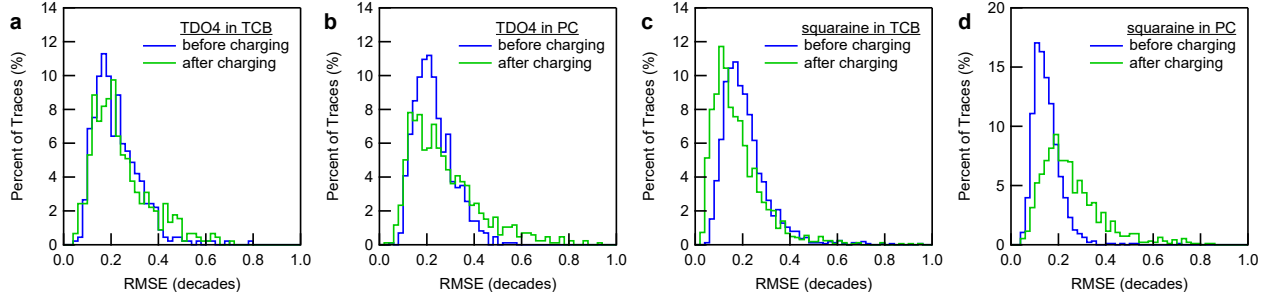


Figure 4.15: Histograms of RMSE for fitted curves of (a) TDO4 in TCB, (b) TDO4 in PC, (c) squaraine in TCB, and (d) squaraine in PC.

to fit this data, we fix  $\alpha$  to be the same as that determined before charging.

Applying fitting constraints improves the quality of fit for some junctions. For experiments performed in non-polar solvents, no constraints are necessary to obtain reasonable values for the level alignment and the level broadening. For convenience, we constrain the level alignment  $\varepsilon$  to be positive, since the model is symmetric with respect to the sign of  $\varepsilon$ . We also constrain the level broadening  $\Gamma$  to be greater than  $1\text{ }\mu\text{eV}$ . For experiments performed in polar solvent, in principle  $\alpha$  should be constrained between 0 and 0.5, whereas  $\varepsilon$  is completely unconstrained. Negative values of  $\varepsilon$  would correspond to HOMO conducting molecules, and positive values of  $\varepsilon$  would correspond to LUMO conducting molecules. In practice, it is more useful to constrain  $\varepsilon$  to be positive and constrain  $\alpha$  to lie between -0.5 and 0.5. Negative values of  $\alpha$  correspond to HOMO conducting molecules, and positive values of  $\alpha$  correspond to LUMO conducting molecules.

To quantify the goodness of fit, we show histograms of the root-mean-square error (RMSE) in Figure 4.15. Because the fitting is performed on a semi-log scale, the RMSE should be interpreted in decades. For all fits, the RMSE is around 0.2 decades. To give a qualitative sense of what this means, a trace with an RMSE of 0.2 is shown in Figure 4.16a. The fitted curve captures the main features of the data. We conclude that a RMSE of 0.2 decades is reasonable.

In order to assuage any concerns that the correlation between the threshold bias and the fitted values of the level alignment is artificial, we took the exemplary data depicted in Figure 4.3a and performed fitting for different values of the threshold bias. That is, we performed fitting for a progressively smaller range of biases to simulate if the junction had ruptured at a bias much lower

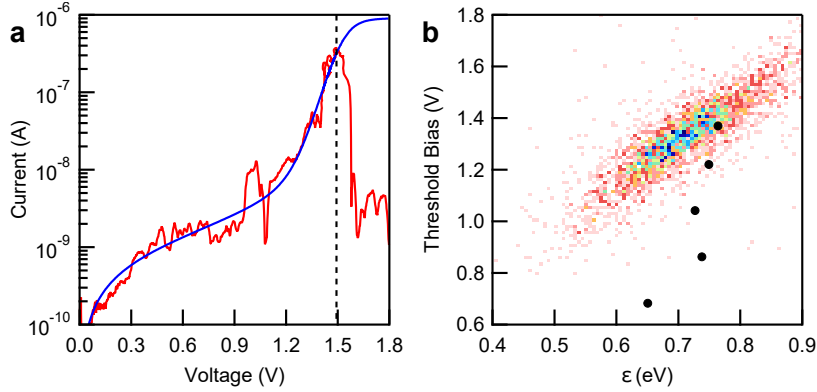


Figure 4.16: (a) Example  $I$ - $V$  data (red) with a fitted  $I$ - $V$  curve (blue) with RMSE of approximately 0.2 decades. (b) Figure 4.3b reproduced with fitted values of level alignment  $\varepsilon$  for five different artificial threshold bias values overlaid on top. The trend in the 2D-histogram is not reproduced by the dots, indicating that the correlation is not due to limitations of the fitting algorithm or model.

than  $2\varepsilon$ . The result is summarized in Figure 4.16b. Although the assumed threshold bias and the fitted values for level alignment are correlated, the correlation due to fitting is not remotely large enough to account for the correlation we see in Figure 4.3b. Incidentally, the fictional threshold bias is also weakly correlated with the fitted value for the level broadening, but there is no evidence of this correlation for the experimental values. We are confident, therefore, that our fitting algorithm returns reasonable values for  $\varepsilon$  even in the case of low threshold bias.

#### 4.8.5 Fitting the Polaron Model in Polar Solvent

The polaron model requires that LUMO conducting molecules become HOMO conducting upon charging in order to explain NDR. More succinctly, the level alignment  $\varepsilon$  changes sign. Figure 4.17 summarizes the resulting fit if we enforce this change in sign for both TDO4 and squaraine measured in PC. The reorganization energy is then given by the equation  $2\lambda = |\tilde{\varepsilon} - \varepsilon_0|$ , where  $\varepsilon_0$  and  $\tilde{\varepsilon}$  are the level alignment before and after charging, respectively. Since  $\varepsilon_0$  and  $\tilde{\varepsilon}$  have opposite signs in the polaron model, this can be rewritten as  $2\lambda = |\tilde{\varepsilon}| + |\varepsilon_0|$ . We can then use Figures 4.4a and 4.10g to estimate the reorganization energy in TCB and Figure 4.17a,c to estimate the reorganization energy in PC. These reorganization energies are summarized in Table 4.2. If we assume the polaron model, the fits imply that the reorganization energy is on average smaller in

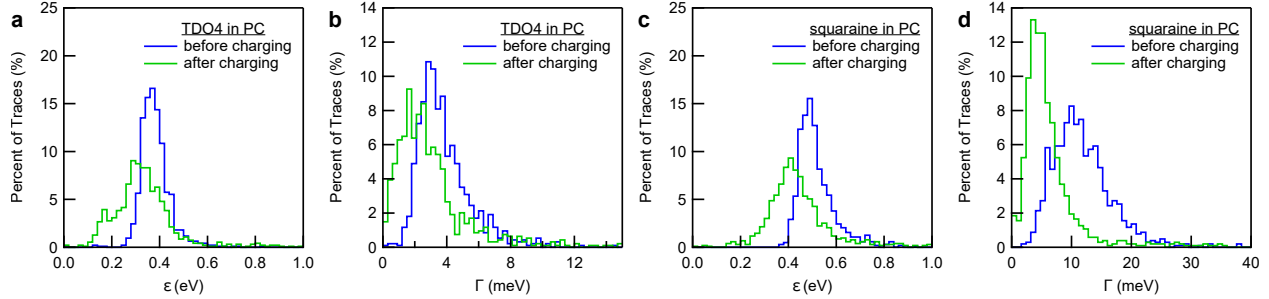


Figure 4.17: Fitted values of level alignment and level broadening before (blue) and after (green) charging for TDO4 in PC ((a) and (b)) and squaraine in PC ((c) and (d)), assuming that the sign of the level alignment changes upon charging. The sign of the level alignment has been suppressed for simplicity.

PC, the polar solvent with a dielectric constant of 66 [279] than in TCB, the non-polar solvent with a dielectric constant of 2.24 [280]. This is the opposite of what is expected from Marcus' theory of charge transfer, and the work of Dzhioev and Kosov predicts that the reorganization energy should be almost double in PC [260]. We therefore conclude that the polaron model, in its current form, cannot explain our experimental results.

We note that this analysis cannot be applied to measurements performed in non-polar solvent. This is because the  $I$ - $V$  curve for experiments performed in non-polar solvent is symmetric with respect to the sign of  $\varepsilon$ . Unlike measurements in polar solvents, therefore, measurements in non-polar solvents require no assumptions about the sign of  $\varepsilon$  in order to perform fitting, and fits apply equally to both the polaron model and the blocking-state model.

Table 4.2: Estimated reorganization energies

	$\lambda_{\text{TCB}}$ (eV)	$\lambda_{\text{PC}}$ (eV)
TDO4	1.7	0.7
squaraine	0.6	0.45

#### 4.8.6 Density Functional Theory-Based Transport Calculations of Squaraine

We compute the transmission function of squaraine using the AITRANSS implementation of the non-equilibrium Green's function formalism within density functional theory (DFT) [82, 83].

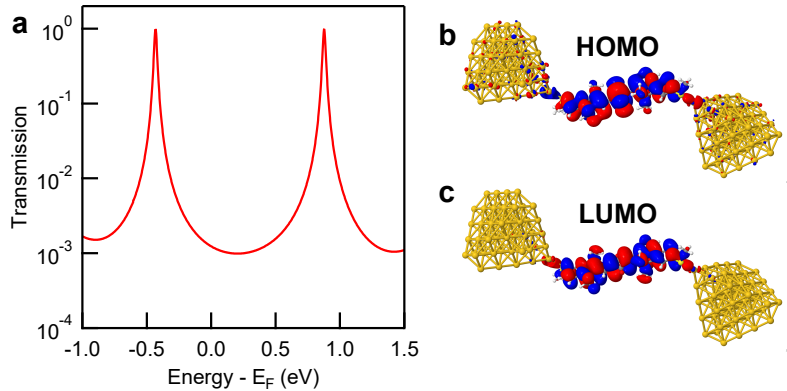


Figure 4.18: (a) Calculated transmission function of a squaraine junction. Isosurfaces of the orbitals of the Au-squaraine-Au system corresponding to the (b) HOMO and (c) LUMO resonance.

AITRANSS is built on the FHI-aims package which uses numerical atom-centered basis functions [281, 282], and we use the PBE exchange-correlation functional [283].

The resulting transmission function is given in Figure 4.18a, which confirms that the molecule is HOMO conducting. Exact level alignment may not match experiment due to limitations of DFT [284]. The Au-squaraine-Au geometry is reproduced in Figure 4.18b,c. Each electrode consists of a pyramidal cluster of 55 Au atoms, arranged in 6 layers in the (111) direction with closest interatomic distance of 2.88 Å. The orbitals corresponding to the HOMO resonance and the LUMO resonance are shown in Figure 4.18b,c.

## Conclusions and Outlook

In this dissertation, we have explored photon emission, photon absorption, and resonant tunneling in nanoscale junctions. In each case, two theories feature prominently in the literature and predict very similar phenomena. The goal of this dissertation has been to explore experimental methods for distinguishing different inelastic effects in nanoscale junctions.

We began with arguably the simplest system: the humble tunnel junction. Inspired by previous work, we measured the so-called overbias emission—photon emission with energies exceeding the classical limit—at room temperature and ambient conditions. The two theories for the overbias emission which we compared are emission from multi-electron processes and blackbody radiation. We demonstrated experimentally that the emission depends superlinearly on the conductance, even at room temperature, consistent with emission from multi-electron processes but not with blackbody radiation.

Second, we considered light absorption processes in single-molecule junctions and measured an enhanced conductance of single-molecule junctions under illumination. The two theories that could explain this effect are photon-assisted tunneling and non-equilibrium hot-electron distributions. We showed mathematically that the enhancement due to hot-electron distributions dominates when the electrodes strongly absorb the incident wavelength and when the lifetime of the electron on the molecule is short compared to the lifetime of the hot-electron distributions. We confirmed this experimentally by measuring an enhanced conductance when the light is polarized perpendicular to the plane of incidence, which is not expected for photon-assisted tunneling.

Finally, we explored in detail the highly non-linear behavior of single-molecule junctions near the resonant tunneling regime. First, we developed a curve-fitting algorithm of the room-temperature Landauer formalism. This allowed us to measure the strong correlation between the

junction bias at which single-molecule junctions rupture and the level-alignment  $\varepsilon$ , suggesting that junction rupture is stimulated by resonant tunneling. However, we also found that some junctions survive, and that these junctions display pronounced negative differential resistance and hysteresis, which we interpret as a charging effect. Additional measurements showed that the dynamics of charging and discharging are on the millisecond timescale. Surprisingly, the two most popular theories for explaining negative differential resistance and hysteresis, the blocking-state and polaron model, cannot explain all our observations.

In many ways, the work in this dissertation is only preliminary, and much work remains to explore the implications of inelastic transport on device applications. Understanding the mechanism for light emission in tunnel junctions is the first step towards studying light emission in single-molecule junctions. As demonstrated by Reecht *et al.* [127], this emission must be carefully considered when measuring light emission from single-molecule junctions. Although most of the literature has focused on the spectral features of light emission in nanoscopic junctions, our work suggests that the dependence of emission on conductance is a powerful tool for discriminating different mechanisms of light emission.

Establishing the mechanism for overbias light emission also suggests ways to develop devices leveraging the phenomenon. Since emission from multi-electron processes is driven by quantum noise, the emission is maximized when  $\tau = 0.5$ . However, electromigration will likely reduce the longevity of tunnel junctions with sub-nanometer junction gaps, especially when operated at high bias. Highly conducting single-molecule junctions are one possible method for producing a more stable junction.

The light absorption experiments require further experimental development. In this work, we have only illuminated the junction with a single wavelength, but more detailed experiments will require developing an experimental apparatus to modify the wavelength while maintaining the precise alignment necessary to increase the current. A continuously tunable laser may provide a method to measure the resonances of the transmission function. In principle, this method could probe resonances beyond the frontier orbitals. This would allow us to measure the changes in

alignment due to electronic coupling with the electrodes, which is a challenging theoretical problem [79].

Finally, our study of transport near the resonant tunneling regime proves that more work is necessary both experimentally and theoretically to advance our understanding of electron-phonon coupling in single-molecule junctions. The existing theories appear valid for molecules weakly electronically coupled to the electrodes but not for well-coupled molecules ( $\Gamma \gtrsim 1$  meV). Although we have observed many molecules that evince the same behavior described in Chapter 4, we have also observed some molecules that do not [234]. Clearly, charge transport in the resonant tunneling regime remains fertile ground for further research. By understanding more deeply the parameters controlling negative differential resistance, hysteresis, and electronically induced junction rupture, we envision a class of single-molecule devices that operate outside the coherent and non-resonant tunneling regimes.

## References

- [1] A. Nitzan and M. A. Ratner, “Electron Transport in Molecular Wire Junctions”, *Science* **300**, 1384–1389 (2003).
- [2] L. Venkataraman, J. E. Klare, C. Nuckolls, M. S. Hybertsen, and M. L. Steigerwald, “Dependence of single-molecule junction conductance on molecular conformation”, *Nature* **442**, 904–907 (2006).
- [3] P. D. Williams and M. G. Reuter, “Level Alignments and Coupling Strengths in Conductance Histograms: The Information Content of a Single Channel Peak”, *The Journal of Physical Chemistry C* **117**, 5937–5942 (2013).
- [4] E. Lörtscher, H. B. Weber, and H. Riel, “Statistical Approach to Investigating Transport through Single Molecules”, *Physical Review Letters* **98**, 176807 (2007).
- [5] R. Frisenda, M. L. Perrin, H. Valkenier, J. C. Hummelen, and H. S. J. van der Zant, “Statistical analysis of single-molecule breaking traces”, *physica status solidi (b)* **250**, 2431–2436 (2013).
- [6] M. A. Reed, C. Zhou, C. J. Muller, T. P. Burgin, and J. M. Tour, “Conductance of a Molecular Junction”, *Science* **278**, 252–254 (1997).
- [7] Y. Selzer and D. L. Allara, “Single-molecule electrical junctions”, *Annual Review of Physical Chemistry* **57**, 593–623 (2006).
- [8] N. J. Tao, “Electron transport in molecular junctions”, *Nature Nanotechnology* **1**, 173–181 (2006).
- [9] S. V. Aradhya and L. Venkataraman, “Single-molecule junctions beyond electronic transport”, *Nature Nanotechnology* **8**, 399–410 (2013).
- [10] A. Aviram and M. A. Ratner, “Molecular rectifiers”, *Chemical Physics Letters* **29**, 277–283 (1974).
- [11] T. A. Su, M. Neupane, M. L. Steigerwald, L. Venkataraman, and C. Nuckolls, “Chemical principles of single-molecule electronics”, *Nature Reviews Materials* **1**, 16002 (2016).
- [12] L. Sun, Y. A. Diaz-Fernandez, T. A. Gschneidtner, F. Westerlund, S. Lara-Avila, and K. Moth-Poulsen, “Single-molecule electronics: from chemical design to functional devices”, *Chemical Society Reviews* **43**, 7378–7411 (2014).

- [13] B. Xu and N. J. Tao, “Measurement of Single-Molecule Resistance by Repeated Formation of Molecular Junctions”, *Science* **301**, 1221–1223 (2003).
- [14] J. He, F. Chen, J. Li, O. F. Sankey, Y. Terazono, C. Herrero, D. Gust, T. A. Moore, A. L. Moore, and S. M. Lindsay, “Electronic Decay Constant of Carotenoid Polyenes from Single-Molecule Measurements”, *Journal of the American Chemical Society* **127**, 1384–1385 (2005).
- [15] L. Venkataraman, J. E. Klare, I. W. Tam, C. Nuckolls, M. S. Hybertsen, and M. L. Steigerwald, “Single-Molecule Circuits with Well-Defined Molecular Conductance”, *Nano Letters* **6**, 458–462 (2006).
- [16] R. S. Klausen, J. R. Widawsky, M. L. Steigerwald, L. Venkataraman, and C. Nuckolls, “Conductive Molecular Silicon”, *Journal of the American Chemical Society* **134**, 4541–4544 (2012).
- [17] M. Koch, F. Ample, C. Joachim, and L. Grill, “Voltage-dependent conductance of a single graphene nanoribbon”, *Nature Nanotechnology* **7**, 713–717 (2012).
- [18] P. Moreno-García, M. Gulcur, D. Z. Manrique, T. Pope, W. Hong, V. Kaliginedi, C. Huang, A. S. Batsanov, M. R. Bryce, C. Lambert, and T. Wandlowski, “Single-Molecule Conductance of Functionalized Oligoynes: Length Dependence and Junction Evolution”, *Journal of the American Chemical Society* **135**, 12228–12240 (2013).
- [19] B. Capozzi, E. J. Dell, T. C. Berkelbach, D. R. Reichman, L. Venkataraman, and L. M. Campos, “Length-Dependent Conductance of Oligothiophenes”, *Journal of the American Chemical Society* **136**, 10486–10492 (2014).
- [20] S. Gunasekaran, D. Hernangómez-Pérez, I. Davydenko, S. Marder, F. Evers, and L. Venkataraman, “Near Length-Independent Conductance in Polymethine Molecular Wires”, *Nano Letters* **18**, 6387–6391 (2018).
- [21] Y. Zang, S. Ray, E.-D. Fung, A. Borges, M. H. Garner, M. L. Steigerwald, G. C. Solomon, S. Patil, and L. Venkataraman, “Resonant Transport in Single Diketopyrrolopyrrole Junctions”, *Journal of the American Chemical Society* **140**, 13167–13170 (2018).
- [22] K. Michaeli, D. N. Beratan, D. H. Waldeck, and R. Naaman, “Voltage-induced long-range coherent electron transfer through organic molecules”, *Proceedings of the National Academy of Sciences* **116**, 5931–5936 (2019).
- [23] M. H. Garner, H. Li, Y. Chen, T. A. Su, Z. Shangguan, D. W. Paley, T. Liu, F. Ng, H. Li, S. Xiao, C. Nuckolls, L. Venkataraman, and G. C. Solomon, “Comprehensive suppression of single-molecule conductance using destructive  $\sigma$ -interference”, *Nature* **558**, 415–419 (2018).

- [24] H. Li, M. H. Garner, T. A. Su, A. Jensen, M. S. Inkpen, M. L. Steigerwald, L. Venkataraman, G. C. Solomon, and C. Nuckolls, “Extreme Conductance Suppression in Molecular Siloxanes”, *Journal of the American Chemical Society* **139**, 10212–10215 (2017).
- [25] M. H. Garner, H. Li, M. Neupane, Q. Zou, T. Liu, T. A. Su, Z. Shangguan, D. W. Paley, F. Ng, S. Xiao, C. Nuckolls, L. Venkataraman, and G. C. Solomon, “Permethylated Introduces Destructive Quantum Interference in Saturated Silanes”, *Journal of the American Chemical Society* **141**, 15471–15476 (2019).
- [26] A. S. Blum, J. G. Kushmerick, D. P. Long, C. H. Patterson, J. C. Yang, J. C. Henderson, Y. Yao, J. M. Tour, R. Shashidhar, and B. R. Ratna, “Molecularly inherent voltage-controlled conductance switching”, *Nature Materials* **4**, 167–172 (2005).
- [27] F. Chen, J. He, C. Nuckolls, T. Roberts, J. E. Klare, and S. Lindsay, “A Molecular Switch Based on Potential-Induced Changes of Oxidation State”, *Nano Letters* **5**, 503–506 (2005).
- [28] E. Lörtscher, J. W. Ciszek, J. Tour, and H. Riel, “Reversible and Controllable Switching of a Single-Molecule Junction”, *Small* **2**, 973–977 (2006).
- [29] S. Y. Quek, M. Kamenetska, M. L. Steigerwald, H. J. Choi, S. G. Louie, M. S. Hybertsen, J. B. Neaton, and L. Venkataraman, “Mechanically controlled binary conductance switching of a single-molecule junction”, *Nature Nanotechnology* **4**, 230–234 (2009).
- [30] C. Schirm, M. Matt, F. Pauly, J. C. Cuevas, P. Nielaba, and E. Scheer, “A current-driven single-atom memory”, *Nature Nanotechnology* **8**, 645–648 (2013).
- [31] T. A. Su, H. Li, M. L. Steigerwald, L. Venkataraman, and C. Nuckolls, “Stereoelectronic switching in single-molecule junctions”, *Nature Chemistry* **7**, 215–220 (2015).
- [32] F. Schwarz, M. Koch, G. Kastlunger, H. Berke, R. Stadler, K. Venkatesan, and E. Lörtscher, “Charge Transport and Conductance Switching of Redox-Active Azulene Derivatives”, *Angewandte Chemie International Edition* **55**, 11781–11786 (2016).
- [33] F. Schwarz, G. Kastlunger, F. Lissel, C. Egler-Lucas, S. N. Semenov, K. Venkatesan, H. Berke, R. Stadler, and E. Lörtscher, “Field-induced conductance switching by charge-state alternation in organometallic single-molecule junctions”, *Nature Nanotechnology* **11**, 170–176 (2016).
- [34] X. Yin, Y. Zang, L. Zhu, J. Z. Low, Z.-F. Liu, J. Cui, J. B. Neaton, L. Venkataraman, and L. M. Campos, “A reversible single-molecule switch based on activated antiaromaticity”, *Science Advances* **3**, eaao2615 (2017).
- [35] J. L. Zhang, J. Q. Zhong, J. D. Lin, W. P. Hu, K. Wu, G. Q. Xu, A. T. S. Wee, and W. Chen, “Towards single molecule switches”, *Science* **44**, 2998–3022 (2015).

- [36] M. Elbing, R. Ochs, M. Koentopp, M. Fischer, C. von Hänisch, F. Weigend, F. Evers, H. B. Weber, and M. Mayor, “A single-molecule diode”, *Proceedings of the National Academy of Sciences* **102**, 8815–8820 (2005).
- [37] E. Lörtscher, B. Gotsmann, Y. Lee, L. Yu, C. Rettner, and H. Riel, “Transport Properties of a Single-Molecule Diode”, *ACS Nano* **6**, 4931–4939 (2012).
- [38] M. L. Perrin, E. Galan, R. Eelkema, F. Grozema, J. M. Thijssen, and H. S. J. van der Zant, “Single-Molecule Resonant Tunneling Diode”, *The Journal of Physical Chemistry C* **119**, 5697–5702 (2015).
- [39] A. Batra, P. Darancet, Q. Chen, J. S. Meisner, J. R. Widawsky, J. B. Neaton, C. Nuckolls, and L. Venkataraman, “Tuning Rectification in Single-Molecular Diodes”, *Nano Letters* **13**, 6233–6237 (2013).
- [40] B. Capozzi, J. Xia, O. Adak, E. J. Dell, Z.-F. Liu, J. C. Taylor, J. B. Neaton, L. M. Campos, and L. Venkataraman, “Single-molecule diodes with high rectification ratios through environmental control”, *Nature Nanotechnology* **10**, 522–527 (2015).
- [41] S. Kubatkin, A. Danilov, M. Hjort, J. Cornil, J.-L. Brédas, N. Stuhr-Hansen, P. Hedegård, and T. Bjørnholm, “Single-electron transistor of a single organic molecule with access to several redox states”, *Nature* **425**, 698–701 (2003).
- [42] Xu, Bingqian, Xiao, Xiaoyin, X. Yang, L. Zang, and Tao, Nongjian, “Large Gate Modulation in the Current of a Room Temperature Single Molecule Transistor”, *Journal of the American Chemical Society* **127**, 2386–2387 (2005).
- [43] X. Li, B. Xu, X. Xiao, X. Yang, L. Zang, and N. Tao, “Controlling charge transport in single molecules using electrochemical gate”, *Faraday Discussions* **131**, 111–120 (2006).
- [44] H. Song, Y. Kim, Y. H. Jang, H. Jeong, M. A. Reed, and T. Lee, “Observation of molecular orbital gating”, *Nature* **462**, 1039–1043 (2009).
- [45] B. Capozzi, Q. Chen, P. Darancet, M. Kotiuga, M. Buzzeo, J. B. Neaton, C. Nuckolls, and L. Venkataraman, “Tunable Charge Transport in Single-Molecule Junctions via Electrolytic Gating”, *Nano Letters* **14**, 1400–1404 (2014).
- [46] K. Xu, H. Lu, E. W. Kinder, A. Seabaugh, and S. K. Fullerton-Shirey, “Monolayer Solid-State Electrolyte for Electric Double Layer Gating of Graphene Field-Effect Transistors”, *ACS Nano* **11**, 5453–5464 (2017).
- [47] Q. Xu, G. Scuri, C. Mathewson, P. Kim, C. Nuckolls, and D. Bouilly, “Single Electron Transistor with Single Aromatic Ring Molecule Covalently Connected to Graphene Nanogaps”, *Nano Letters* **17**, 5335–5341 (2017).

- [48] M. L. Perrin, E. Burzurí, and H. S. J. van der Zant, “Single-molecule transistors”, *Chemical Society Reviews* **44**, 902–919 (2015).
- [49] C. M. Guédon, H. Valkenier, T. Markussen, K. S. Thygesen, J. C. Hummelen, and S. J. van der Molen, “Observation of quantum interference in molecular charge transport”, *Nature Nanotechnology* **7**, 305–309 (2012).
- [50] H. Li, M. H. Garner, Z. Shangguan, Y. Chen, Q. Zheng, T. A. Su, M. Neupane, T. Liu, M. L. Steigerwald, F. Ng, C. Nuckolls, S. Xiao, G. C. Solomon, and L. Venkataraman, “Large Variations in the Single-Molecule Conductance of Cyclic and Bicyclic Silanes”, *Journal of the American Chemical Society* **140**, 15080–15088 (2018).
- [51] P. Sautet and C. Joachim, “Electronic interference produced by a benzene embedded in a polyacetylene chain”, *Chemical Physics Letters* **153**, 511–516 (1988).
- [52] D. Q. Andrews, G. C. Solomon, R. H. Goldsmith, T. Hansen, M. R. Wasielewski, R. P. V. Duyne, and M. A. Ratner, “Quantum Interference: The Structural Dependence of Electron Transmission through Model Systems and Cross-Conjugated Molecules”, *The Journal of Physical Chemistry C* **112**, 16991–16998 (2008).
- [53] T. Hansen, G. C. Solomon, D. Q. Andrews, and M. A. Ratner, “Interfering pathways in benzene: An analytical treatment”, *The Journal of Chemical Physics* **131**, 194704 (2009).
- [54] T. Markussen, R. Stadler, and K. S. Thygesen, “The Relation between Structure and Quantum Interference in Single Molecule Junctions”, *Nano Letters* **10**, 4260–4265 (2010).
- [55] A. Borges, J. Xia, S. H. Liu, L. Venkataraman, and G. C. Solomon, “The Role of Through-Space Interactions in Modulating Constructive and Destructive Interference Effects in Benzene”, *Nano Letters* **17**, 4436–4442 (2017).
- [56] S. Gunasekaran, J. E. Greenwald, and L. Venkataraman, “Visualizing Quantum Interference in Molecular Junctions”, *Nano Letters* **20**, 2843–2848 (2020).
- [57] W. Liang, M. P. Shores, M. Bockrath, J. R. Long, and H. Park, “Kondo resonance in a single-molecule transistor”, *Nature* **417**, 725–729 (2002).
- [58] L. Bogani and W. Wernsdorfer, “Molecular spintronics using single-molecule magnets”, *Nature Materials* **7**, 179–186 (2008).
- [59] R. Vincent, S. Klyatskaya, M. Ruben, W. Wernsdorfer, and F. Balestro, “Electronic read-out of a single nuclear spin using a molecular spin transistor”, *Nature* **488**, 357–360 (2012).
- [60] S. Wagner, F. Kisslinger, S. Ballmann, F. Schramm, R. Chandrasekar, T. Bodenstein, O. Fuhr, D. Secker, K. Fink, M. Ruben, and H. B. Weber, “Switching of a coupled spin pair in a single-molecule junction”, *Nature Nanotechnology* **8**, 575–579 (2013).

- [61] S. Thiele, F. Balestro, R. Ballou, S. Klyatskaya, M. Ruben, and W. Wernsdorfer, “Electrically driven nuclear spin resonance in single-molecule magnets”, *Science* **344**, 1135–1138 (2014).
- [62] H. Hammar and J. Fransson, “Time-dependent spin and transport properties of a single-molecule magnet in a tunnel junction”, *Physical Review B* **94**, 054311 (2016).
- [63] R. Gaudenzi, J. de Bruijckere, D. Reta, I. d. P. R. Moreira, C. Rovira, J. Veciana, H. S. J. van der Zant, and E. Burzurí, “Redox-Induced Gating of the Exchange Interactions in a Single Organic Diradical”, *ACS Nano* **11**, 5879–5883 (2017).
- [64] E. Coronado, “Molecular magnetism: from chemical design to spin control in molecules, materials and devices”, *Nature Reviews Materials*, 1–18 (2019).
- [65] C.-H. Ko, M.-J. Huang, M.-D. Fu, and C.-h. Chen, “Superior Contact for Single-Molecule Conductance: Electronic Coupling of Thiolate and Isothiocyanate on Pt, Pd, and Au”, *Journal of the American Chemical Society* **132**, 756–764 (2010).
- [66] T. Kim, H. Vázquez, M. S. Hybertsen, and L. Venkataraman, “Conductance of Molecular Junctions Formed with Silver Electrodes”, *Nano Letters* **13**, 3358–3364 (2013).
- [67] T. Kim, Z.-F. Liu, C. Lee, J. B. Neaton, and L. Venkataraman, “Charge transport and rectification in molecular junctions formed with carbon-based electrodes”, *Proceedings of the National Academy of Sciences* **111**, 10928–10932 (2014).
- [68] C. Jia, B. Ma, N. Xin, and X. Guo, “Carbon Electrode–Molecule Junctions: A Reliable Platform for Molecular Electronics”, *Accounts of Chemical Research* **48**, 2565–2575 (2015).
- [69] C. Jia and X. Guo, “Molecule–electrode interfaces in molecular electronic devices”, *Chemical Society Reviews* **42**, 5642–5660 (2013).
- [70] X. Pan, B. Lawson, A. M. Rustad, and M. Kamenetska, “pH-Activated Single Molecule Conductance and Binding Mechanism of Imidazole on Gold”, *Nano Letters* **20**, 4687–4692 (2020).
- [71] H. Atesci, V. Kaliginedi, J. A. C. Gil, H. Ozawa, J. M. Thijssen, P. Broekmann, M.-a. Haga, and S. J. van der Molen, “Humidity-controlled rectification switching in ruthenium-complex molecular junctions”, *Nature Nanotechnology*, 1 (2017).
- [72] J. C. Cuevas and E. Scheer, *Molecular Electronics*, 2nd, World Scientific Series in Nanoscience and Nanotechnology, Vol. 15 Volume 15 (World Scientific, Singapore, Apr. 2017).
- [73] R. Landauer, “Spatial Variation of Currents and Fields Due to Localized Scatterers in Metallic Conduction”, *IBM Journal of Research and Development* **1**, 223–231 (1957).

- [74] R. Landauer, “Electrical resistance of disordered one-dimensional lattices”, *The Philosophical Magazine: A Journal of Theoretical Experimental and Applied Physics* **21**, 863–867 (1970).
- [75] A. V. Krasavin, P. V. Borisyuk, O. S. Vasiliev, Y. V. Zhumagulov, V. A. Kashurnikov, U. N. Kurelchuk, and Y. Y. Lebedinskii, “Calculation of density of states of transition metals: From bulk sample to nanocluster”, *Review of Scientific Instruments* **89**, 033907 (2018).
- [76] N. Ittah, G. Noy, I. Yutsis, and Y. Selzer, “Measurement of Electronic Transport through  $1G_0$  Gold Contacts under Laser Irradiation”, *Nano Letters* **9**, 1615–1620 (2009).
- [77] H. Ishii, K. Sugiyama, E. Ito, and K. Seki, “Energy Level Alignment and Interfacial Electronic Structures at Organic/Metal and Organic/Organic Interfaces”, *Advanced Materials* **11**, 605–625 (1999).
- [78] S. Braun, W. R. Salaneck, and M. Fahlman, “Energy-Level Alignment at Organic/Metal and Organic/Organic Interfaces”, *Advanced Materials* **21**, 1450–1472 (2009).
- [79] J. B. Neaton, M. S. Hybertsen, and S. G. Louie, “Renormalization of Molecular Electronic Levels at Metal-Molecule Interfaces”, *Physical Review Letters* **97**, 216405 (2006).
- [80] G. Witte, S. Lukas, P. S. Bagus, and C. Wöll, “Vacuum level alignment at organic/metal junctions: “Cushion” effect and the interface dipole”, *Applied Physics Letters* **87**, 263502 (2005).
- [81] J. Heurich, J. C. Cuevas, W. Wenzel, and G. Schön, “Electrical Transport through Single-Molecule Junctions: From Molecular Orbitals to Conduction Channels”, *Physical Review Letters* **88**, 256803 (2002).
- [82] A. Arnold, F. Weigend, and F. Evers, “Quantum chemistry calculations for molecules coupled to reservoirs: Formalism, implementation, and application to benzenedithiol”, *The Journal of Chemical Physics* **126**, 174101 (2007).
- [83] A. Bagrets, “Spin-Polarized Electron Transport Across Metal–Organic Molecules: A Density Functional Theory Approach”, *Journal of Chemical Theory and Computation* **9**, 2801–2815 (2013).
- [84] A. D. Bochevarov, E. Harder, T. F. Hughes, J. R. Greenwood, D. A. Braden, D. M. Philipp, D. Rinaldo, M. D. Halls, J. Zhang, and R. A. Friesner, “Jaguar: A high-performance quantum chemistry software program with strengths in life and materials sciences”, *International Journal of Quantum Chemistry* **113**, 2110–2142 (2013).
- [85] U. Peskin, “An introduction to the formulation of steady-state transport through molecular junctions”, *Journal of Physics B: Atomic, Molecular and Optical Physics* **43**, 153001 (2010).

- [86] G. Breit and E. Wigner, “Capture of Slow Neutrons”, *Physical Review* **49**, 519–531 (1936).
- [87] C. Ott, A. Kaldun, P. Raith, K. Meyer, M. Laux, J. Evers, C. H. Keitel, C. H. Greene, and T. Pfeifer, “Lorentz Meets Fano in Spectral Line Shapes: A Universal Phase and Its Laser Control”, *Science* **340**, 716–720 (2013).
- [88] P. W. Anderson, D. J. Thouless, E. Abrahams, and D. S. Fisher, “New method for a scaling theory of localization”, *Physical Review B* **22**, 3519–3526 (1980).
- [89] M. Büttiker, Y. Imry, R. Landauer, and S. Pinhas, “Generalized many-channel conductance formula with application to small rings”, *Physical Review B* **31**, 6207–6215 (1985).
- [90] M. Büttiker, “Scattering theory of current and intensity noise correlations in conductors and wave guides”, *Physical Review B* **46**, 12485–12507 (1992).
- [91] H. Ness, S. A. Shevlin, and A. J. Fisher, “Coherent electron-phonon coupling and polaron-like transport in molecular wires”, *Physical Review B* **63**, 125422 (2001).
- [92] Z. Zhang and J. Wang, “Vibrational and coherence dynamics of molecules”, *Physical Chemistry Chemical Physics* **17**, 23754–23760 (2015).
- [93] R. F. Begley, A. B. Harvey, and R. L. Byer, “Coherent anti-Stokes Raman spectroscopy”, *Applied Physics Letters* **25**, 387–390 (1974).
- [94] O. F. A. Larsen, P. Bodis, W. J. Buma, J. S. Hannam, D. A. Leigh, and S. Woutersen, “Probing the structure of a rotaxane with two-dimensional infrared spectroscopy”, *Proceedings of the National Academy of Sciences of the United States of America* **102**, 13378 (2005).
- [95] S. S. Kondov, C.-H. Lee, K. H. Leung, C. Liedl, I. Majewska, R. Moszynski, and T. Zelevinsky, “Molecular lattice clock with long vibrational coherence”, *Nature Physics* **15**, 1118–1122 (2019).
- [96] M. Maldovan, “Sound and heat revolutions in phononics”, *Nature* **503**, 209–217 (2013).
- [97] F. Reif, Fundamentals of Statistical and Thermal Physics (Waveland Press, 2009).
- [98] M. Galperin, M. A. Ratner, and A. Nitzan, “Inelastic electron tunneling spectroscopy in molecular junctions: Peaks and dips”, *The Journal of Chemical Physics* **121**, 11965–11979 (2004).
- [99] Z. Bihary and M. A. Ratner, “Dephasing effects in molecular junction conduction: An analytical treatment”, *Physical Review B* **72**, 115439 (2005).
- [100] R. Golizadeh-Mojarad and S. Datta, “Nonequilibrium Green’s function based models for dephasing in quantum transport”, *Physical Review B* **75**, 081301(R) (2007).

- [101] D. Nozaki, C. Gomes da Rocha, H. M. Pastawski, and G. Cuniberti, “Disorder and dephasing effects on electron transport through conjugated molecular wires in molecular junctions”, *Physical Review B* **85**, 155327 (2012).
- [102] M. Galperin, “Photonics and spectroscopy in nanojunctions: a theoretical insight”, *Chemical Society Reviews* **46**, 4000–4019 (2017).
- [103] A. J. White, B. D. Fainberg, and M. Galperin, “Collective Plasmon-Molecule Excitations in Nanojunctions: Quantum Consideration”, *The Journal of Physical Chemistry Letters* **3**, 2738–2743 (2012).
- [104] B. C. Stipe, M. A. Rezaei, and W. Ho, “Single-Molecule Vibrational Spectroscopy and Microscopy”, *Science* **280**, 1732–1735 (1998).
- [105] X. H. Qiu, G. V. Nazin, and W. Ho, “Vibrationally Resolved Fluorescence Excited with Submolecular Precision”, *Science* **299**, 542–546 (2003).
- [106] X. H. Qiu, G. V. Nazin, and W. Ho, “Vibronic States in Single Molecule Electron Transport”, *Physical Review Letters* **92**, 206102 (2004).
- [107] E. Ćavar, M.-C. Blüm, M. Pivetta, F. Patthey, M. Chergui, and W.-D. Schneider, “Fluorescence and phosphorescence from individual  $C_{60}$  molecules excited by local electron tunneling”, *Phys. Rev. Lett.* **95**, 196102 (2005).
- [108] S. W. Wu, G. V. Nazin, and W. Ho, “Intramolecular photon emission from a single molecule in a scanning tunneling microscope”, *Physical Review B* **77**, 205430 (2008).
- [109] B. Doppagne, M. C. Chong, H. Bulou, A. Boeglin, F. Scheurer, and G. Schull, “Electrofluorochromism at the single-molecule level”, *Science* **361**, 251–255 (2018).
- [110] A. Roy-Gobeil, Y. Miyahara, K. H. Bevan, and P. Grutter, “Fully Quantized Electron Transfer Observed in a Single Redox Molecule at a Metal Interface”, *Nano Letters* **19**, 6104–6108 (2019).
- [111] K. Kimura, K. Miwa, H. Imada, M. Imai-Imada, S. Kawahara, J. Takeya, M. Kawai, M. Galperin, and Y. Kim, “Selective triplet exciton formation in a single molecule”, *Nature*, 1 (2019).
- [112] L. H. Yu, Z. K. Keane, J. W. Ciszek, L. Cheng, M. P. Stewart, J. M. Tour, and D. Natelson, “Inelastic Electron Tunneling via Molecular Vibrations in Single-Molecule Transistors”, *Physical Review Letters* **93**, 266802 (2004).
- [113] J. G. Kushmerick, J. Lazorcik, C. H. Patterson, R. Shashidhar, D. S. Seferos, and G. C. Bazan, “Vibronic Contributions to Charge Transport Across Molecular Junctions”, *Nano Letters* **4**, 639–642 (2004).

- [114] W. Wang, T. Lee, I. Kretzschmar, and M. A. Reed, “Inelastic Electron Tunneling Spectroscopy of an Alkanedithiol Self-Assembled Monolayer”, *Nano Letters* **4**, 643–646 (2004).
- [115] M. Galperin, M. A. Ratner, A. Nitzan, and A. Troisi, “Nuclear Coupling and Polarization in Molecular Transport Junctions: Beyond Tunneling to Function”, *Science* **319**, 1056–1060 (2008).
- [116] M. Galperin, M. A. Ratner, and A. Nitzan, “Molecular transport junctions: vibrational effects”, *Journal of Physics: Condensed Matter* **19**, 103201 (2007).
- [117] Y. Selzer, M. A. Cabassi, T. S. Mayer, and D. L. Allara, “Thermally Activated Conduction in Molecular Junctions”, *Journal of the American Chemical Society* **126**, 4052–4053 (2004).
- [118] S. H. Choi, B. Kim, and C. D. Frisbie, “Electrical Resistance of Long Conjugated Molecular Wires”, *Science* **320**, 1482–1486 (2008).
- [119] B. Giese, J. Amaudrut, A.-K. Köhler, M. Spormann, and S. Wessely, “Direct observation of hole transfer through DNA by hopping between adenine bases and by tunnelling”, *Nature* **412**, 318–320 (2001).
- [120] L. Luo, S. H. Choi, and C. D. Frisbie, “Probing Hopping Conduction in Conjugated Molecular Wires Connected to Metal Electrodes”, *Chemistry of Materials* **23**, 631–645 (2011).
- [121] R. Arielly, A. Ofarim, G. Noy, and Y. Selzer, “Accurate Determination of Plasmonic Fields in Molecular Junctions by Current Rectification at Optical Frequencies”, *Nano Letters* **11**, 2968–2972 (2011).
- [122] M. Vadai, N. Nachman, M. Ben-Zion, M. Bürkle, F. Pauly, J. C. Cuevas, and Y. Selzer, “Plasmon-Induced Conductance Enhancement in Single-Molecule Junctions”, *The Journal of Physical Chemistry Letters* **4**, 2811–2816 (2013).
- [123] K. Yoshida, K. Shibata, and K. Hirakawa, “Terahertz Field Enhancement and Photon-Assisted Tunneling in Single-Molecule Transistors”, *Physical Review Letters* **115**, 138302 (2015).
- [124] M. Vadai and Y. Selzer, “Plasmon-Induced Hot Carriers Transport in Metallic Ballistic Junctions”, *The Journal of Physical Chemistry C* **120**, 21063–21068 (2016).
- [125] D. Natelson, Y. Li, and J. B. Herzog, “Nanogap structures: combining enhanced Raman spectroscopy and electronic transport”, **15**, 5262–5275 (2013).
- [126] N. L. Schneider, J. T. Lü, M. Brandbyge, and R. Berndt, “Light Emission Probing Quantum Shot Noise and Charge Fluctuations at a Biased Molecular Junction”, *Physical Review Letters* **109**, 186601 (2012).

- [127] G. Reecht, F. Scheurer, V. Speisser, Y. J. Dappe, F. Mathevet, and G. Schull, “Electroluminescence of a Polythiophene Molecular Wire Suspended between a Metallic Surface and the Tip of a Scanning Tunneling Microscope”, *Physical Review Letters* **112**, 047403 (2014).
- [128] M. C. Chong, G. Reecht, H. Bulou, A. Boeglin, F. Scheurer, F. Mathevet, and G. Schull, “Narrow-Line Single-Molecule Transducer between Electronic Circuits and Surface Plasmons”, *Physical Review Letters* **116**, 036802 (2016).
- [129] M. C. Chong, L. Sosa-Vargas, H. Bulou, A. Boeglin, F. Scheurer, F. Mathevet, and G. Schull, “Ordinary and Hot Electroluminescence from Single-Molecule Devices: Controlling the Emission Color by Chemical Engineering”, *Nano Letters* **16**, 6480–6484 (2016).
- [130] M. C. Chong, N. Afshar-Imani, F. Scheurer, C. Cardoso, A. Ferretti, D. Prezzi, and G. Schull, “Bright Electroluminescence from Single Graphene Nanoribbon Junctions”, *Nano Letters* **18**, 175–181 (2018).
- [131] S. Datta, Electronic transport in mesoscopic systems (Cambridge University Press, Cambridge, 2009).
- [132] S. Datta, Quantum Transport: Atom to Transistor. (Cambridge University Press, Cambridge, 2013).
- [133] R. D. Mattuck, A Guide to Feynman Diagrams in the Many-Body Problem: Second Edition (Courier Corporation, Aug. 2012).
- [134] L. P. Kadanoff and G. Baym, Quantum Statistical Mechanics (Avalon Publishing, Dec. 1994).
- [135] J. Rammer and H. Smith, “Quantum field-theoretical methods in transport theory of metals”, *Reviews of Modern Physics* **58**, 323–359 (1986).
- [136] G. D. Mahan, Many-Particle Physics, Third, Physics of Solids and Liquids (Springer US, 2000).
- [137] E. N. Economou, Green’s Functions in Quantum Physics, Third, Springer Series in Solid-State Sciences (Springer-Verlag, Berlin Heidelberg, 2006).
- [138] J. M. Krans, J. M. van Ruitenbeek, V. V. Fisun, I. K. Yanson, and L. J. de Jongh, “The signature of conductance quantization in metallic point contacts”, *Nature* **375**, 767–769 (1995).
- [139] C. J. Muller, J. M. van Ruitenbeek, and L. J. de Jongh, “Experimental observation of the transition from weak link to tunnel junction”, *Physica C: Superconductivity* **191**, 485–504 (1992).

- [140] J. Moreland and J. W. Ekin, “Electron tunneling experiments using Nb-Sn “break” junctions”, *Journal of Applied Physics* **58**, 3888–3895 (1985).
- [141] J. R. Widawsky, “Probing Electronic and Thermoelectric Properties of Single Molecule Junctions”, PhD thesis (Columbia University, 2013).
- [142] C. A. Martin, D. Ding, J. K. Sørensen, T. Bjørnholm, J. M. van Ruitenbeek, and H. S. J. van der Zant, “Fullerene-Based Anchoring Groups for Molecular Electronics”, *Journal of the American Chemical Society* **130**, 13198–13199 (2008).
- [143] J. Lambe and S. L. McCarthy, “Light Emission from Inelastic Electron Tunneling”, *Physical Review Letters* **37**, 923–925 (1976).
- [144] K. Kuhnke, C. Große, P. Merino, and K. Kern, “Atomic-Scale Imaging and Spectroscopy of Electroluminescence at Molecular Interfaces”, *Chemical Reviews* **117**, 5174–5222 (2017).
- [145] R. Pechou, R. Coratger, F. Ajustron, and J. Beauvillain, “Cutoff anomalies in light emitted from the tunneling junction of a scanning tunneling microscope in air”, *Applied Physics Letters* **72**, 671–673 (1998).
- [146] V. Kalathingal, P. Dawson, and J. Mitra, “Scanning tunnelling microscope light emission: Finite temperature current noise and over cut-off emission”, *Scientific Reports* **7**, 3530 (2017).
- [147] F. Xu, C. Holmqvist, and W. Belzig, “Overbias Light Emission due to Higher-Order Quantum Noise in a Tunnel Junction”, *Physical Review Letters* **113**, 066801 (2014).
- [148] F. Xu, C. Holmqvist, G. Rastelli, and W. Belzig, “Dynamical Coulomb blockade theory of plasmon-mediated light emission from a tunnel junction”, *Physical Review B* **94**, 245111 (2016).
- [149] K. Kaasbjerg and A. Nitzan, “Theory of Light Emission from Quantum Noise in Plasmonic Contacts: Above-Threshold Emission from Higher-Order Electron-Plasmon Scattering”, *Physical Review Letters* **114**, 126803 (2015).
- [150] G. Schull, N. Néel, P. Johansson, and R. Berndt, “Electron-Plasmon and Electron-Electron Interactions at a Single Atom Contact”, *Physical Review Letters* **102**, 057401 (2009).
- [151] N. L. Schneider, G. Schull, and R. Berndt, “Optical Probe of Quantum Shot-Noise Reduction at a Single-Atom Contact”, *Physical Review Letters* **105**, 026601 (2010).
- [152] N. L. Schneider, P. Johansson, and R. Berndt, “Hot electron cascades in the scanning tunneling microscope”, *Physical Review B* **87**, 045409 (2013).

- [153] P.-J. Peters, F. Xu, K. Kaasbjerg, G. Rastelli, W. Belzig, and R. Berndt, “Quantum Coherent Multielectron Processes in an Atomic Scale Contact”, *Physical Review Letters* **119**, 066803 (2017).
- [154] A. Downes, P. Dumas, and M. E. Welland, “Measurement of high electron temperatures in single atom metal point contacts by light emission”, *Applied Physics Letters* **81**, 1252–1254 (2002).
- [155] M. Buret, A. V. Uskov, J. Dellinger, N. Cazier, M.-M. Mennemantueil, J. Berthelot, I. V. Smetanin, I. E. Protsenko, G. Colas-des-Francs, and A. Bouhelier, “Spontaneous Hot-Electron Light Emission from Electron-Fed Optical Antennas”, *Nano Letters* **15**, 5811–5818 (2015).
- [156] T. Malinowski, H. R. Klein, M. Iazykov, and P. Dumas, “Infrared light emission from nano hot electron gas created in atomic point contacts”, *Europhysics Letters* **114**, 57002 (2016).
- [157] M. Buret, I. V. Smetanin, A. V. Uskov, G. C. des Francs, and A. Bouhelier, “Effect of quantized conductivity on the anomalous photon emission radiated from atomic-size point contacts”, *Nanophotonics* **9**, 413–425 (2020).
- [158] L. Cui, Y. Zhu, M. Abbasi, A. Ahmadvand, B. Gerislioglu, P. Nordlander, and D. Natelson, “Electrically Driven Hot-Carrier Generation and Above-Threshold Light Emission in Plasmonic Tunnel Junctions”, *Nano Letters* (2020).
- [159] W. Du, T. Wang, H.-S. Chu, and C. A. Nijhuis, “Highly efficient on-chip direct electronic–plasmonic transducers”, *Nature Photonics* **11**, 623–627 (2017).
- [160] J. M. Krans, C. J. Muller, I. K. Yanson, T. C. M. Govaert, R. Hesper, and J. M. van Ruitenberg, “One-atom point contacts”, *Physical Review B* **48**, 14721–14724 (1993).
- [161] R. Fukuzumi, S. Kaneko, S. Fujii, T. Nishino, and M. Kiguchi, “Formation of a Chain-like Water Single Molecule Junction with Pd Electrodes”, *The Journal of Physical Chemistry C* **122**, 4698–4703 (2018).
- [162] B. Rogez, S. Cao, G. Dujardin, G. Comtet, E. L. Moal, A. Mayne, and E. Boer-Duchemin, “The mechanism of light emission from a scanning tunnelling microscope operating in air”, *Nanotechnology* **27**, 465201 (2016).
- [163] M. G. Boyle, J. Mitra, and P. Dawson, “The tip–sample water bridge and light emission from scanning tunnelling microscopy”, *Nanotechnology* **20**, 335202 (2009).
- [164] D. Hone, B. Mühlischlegel, and D. J. Scalapino, “Theory of light emission from small particle tunnel junctions”, *Applied Physics Letters* **33**, 203–204 (1978).

- [165] M. Parzefall and L. Novotny, “Optical antennas driven by quantum tunneling: a key issues review”, *Reports on Progress in Physics* **82**, 112401 (2019).
- [166] G. B. Lesovik and R. Loosen, “On the detection of finite-frequency current fluctuations”, *Journal of Experimental and Theoretical Physics Letters* **65**, 295–299 (1997).
- [167] U. Gavish, Y. Levinson, and Y. Imry, “Detection of quantum noise”, *Physical Review B* **62**, R10637–R10640 (2000).
- [168] A. A. Clerk, M. H. Devoret, S. M. Girvin, F. Marquardt, and R. J. Schoelkopf, “Introduction to quantum noise, measurement, and amplification”, *Reviews of Modern Physics* **82**, 1155–1208 (2010).
- [169] D Rogovin and D. J Scalapino, “Fluctuation phenomena in tunnel junctions”, *Annals of Physics* **86**, 1–90 (1974).
- [170] Y. M. Blanter and M. Büttiker, “Shot noise in mesoscopic conductors”, *Physics Reports* **336**, 1–166 (2000).
- [171] R. Aguado and L. P. Kouwenhoven, “Double Quantum Dots as Detectors of High-Frequency Quantum Noise in Mesoscopic Conductors”, *Physical Review Letters* **84**, 1986–1989 (2000).
- [172] J. Tobiska, J. Danon, I. Snyman, and Y. V. Nazarov, “Quantum Tunneling Detection of Two-Photon and Two-Electron Processes”, *Physical Review Letters* **96**, 096801 (2006).
- [173] P. Tomchuk and R. Fedorovich, “Emission of hot electrons from thin metal films”, *Soviet Physics, Solid State* **8**, 226–227 (1966).
- [174] A. Downes, Private Communication, 2020.
- [175] A. R. Downes, “Photon emission from metals in the scanning tunnelling microscope”, Ph.D. Dissertation (University of Cambridge, 1997).
- [176] R. Esteban, A. G. Borisov, P. Nordlander, and J. Aizpurua, “Bridging quantum and classical plasmonics with a quantum-corrected model”, *Nature Communications* **3**, 825 (2012).
- [177] V. Kravtsov, S. Berweger, J. M. Atkin, and M. B. Raschke, “Control of Plasmon Emission and Dynamics at the Transition from Classical to Quantum Coupling”, *Nano Letters* **14**, 5270–5275 (2014).
- [178] D. Marinica, A. Kazansky, P. Nordlander, J. Aizpurua, and A. G. Borisov, “Quantum Plasmonics: Nonlinear Effects in the Field Enhancement of a Plasmonic Nanoparticle Dimer”, *Nano Letters* **12**, 1333–1339 (2012).

- [179] J. Zuloaga, E. Prodan, and P. Nordlander, “Quantum Description of the Plasmon Resonances of a Nanoparticle Dimer”, *Nano Letters* **9**, 887–891 (2009).
- [180] K. J. Savage, M. M. Hawkeye, R. Esteban, A. G. Borisov, J. Aizpurua, and J. J. Baumberg, “Revealing the quantum regime in tunnelling plasmonics”, *Nature* **491**, 574–577 (2012).
- [181] A. N. Koya and J. Lin, “Charge transfer plasmons: Recent theoretical and experimental developments”, *Applied Physics Reviews* **4**, 021104 (2017).
- [182] E.-D. Fung, O. Adak, G. Lovat, D. Scarabelli, and L. Venkataraman, “Too Hot for Photon-Assisted Transport: Hot-Electrons Dominate Conductance Enhancement in Illuminated Single-Molecule Junctions”, *Nano Letters* **17**, 1255–1261 (2017).
- [183] O. Adak, R. Korytár, A. Y. Joe, F. Evers, and L. Venkataraman, “Impact of Electrode Density of States on Transport through Pyridine-Linked Single Molecule Junctions”, *Nano Letters* **15**, 3716–3722 (2015).
- [184] M. Galperin and A. Nitzan, “Molecular optoelectronics: the interaction of molecular conduction junctions with light”, *14*, 9421–9438 (2012).
- [185] D. Dulić, S. J. van der Molen, T. Kudernac, H. T. Jonkman, J. J. D. de Jong, T. N. Bowden, J. van Esch, B. L. Feringa, and B. J. van Wees, “One-Way Optoelectronic Switching of Photochromic Molecules on Gold”, *Physical Review Letters* **91**, 207402 (2003).
- [186] A.-P. Jauho, N. S. Wingreen, and Y. Meir, “Time-dependent transport in interacting and noninteracting resonant-tunneling systems”, *Physical Review B* **50**, 5528–5544 (1994).
- [187] S. Kohler, S. Camalet, M. Strass, J. Lehmann, G.-L. Ingold, and P. Hänggi, “Charge transport through a molecule driven by a high-frequency field”, *Chemical Physics* **296**, The Spin-Boson Problem: From Electron Transfer to Quantum Computing ... to the 60th Birthday of Professor Ulrich Weiss, 243 –249 (2004).
- [188] G. Platero and R. Aguado, “Photon-assisted transport in semiconductor nanostructures”, *Physics Reports* **395**, 1–157 (2004).
- [189] S. Kohler, J. Lehmann, and P. Hänggi, “Driven quantum transport on the nanoscale”, *Physics Reports* **406**, 379–443 (2005).
- [190] A. H. Dayem and R. J. Martin, “Quantum Interaction of Microwave Radiation with Tunneling Between Superconductors”, *Physical Review Letters* **8**, 246–248 (1962).
- [191] P. K. Tien and J. P. Gordon, “Multiphoton Process Observed in the Interaction of Microwave Fields with the Tunneling between Superconductor Films”, *Physical Review* **129**, 647–651 (1963).

- [192] B. Pettinger, B. Ren, G. Picardi, R. Schuster, and G. Ertl, “Nanoscale Probing of Adsorbed Species by Tip-Enhanced Raman Spectroscopy”, *Physical Review Letters* **92**, 096101 (2004).
- [193] A. Campion and P. Kambhampati, “Surface-enhanced Raman scattering”, *27*, 241–250 (1998).
- [194] A. Giugni, B. Torre, A. Toma, M. Francardi, M. Malerba, A. Alabastri, R. P. Zaccaria, M. I. Stockman, and E. D. Fabrizio, “Hot-electron nanoscopy using adiabatic compression of surface plasmons”, *Nature Nanotechnology* **8**, 845–852 (2013).
- [195] S. Lal, S. Link, and N. J. Halas, “Nano-optics from sensing to waveguiding”, *Nature Photonics* **1**, 641–648 (2007).
- [196] E. Ozbay, “Plasmonics: Merging Photonics and Electronics at Nanoscale Dimensions”, *Science* **311**, 189–193 (2006).
- [197] J. Zhang, L. Zhang, and W. Xu, “Surface plasmon polaritons: physics and applications”, *Journal of Physics D: Applied Physics* **45**, 113001 (2012).
- [198] M. Lenner, P. Rácz, P. Dombi, G. Farkas, and N. Kroó, “Field enhancement and rectification of surface plasmons detected by scanning tunneling microscopy”, *Physical Review B* **83**, 205428 (2011).
- [199] H. Q. Nguyen, P. H. Cutler, T. E. Feuchtwang, Z. H. Huang, Y. Kuk, P. J. Silverman, A. A. Lucas, and T. E. Sullivan, “Mechanisms of current rectification in an STM tunnel junction and the measurement of an operational tunneling time”, *IEEE Transactions on Electron Devices* **36**, 2671–2678 (1989).
- [200] A. V. Bragas, S. M. Landi, and O. E. Martínez, “Laser field enhancement at the scanning tunneling microscope junction measured by optical rectification”, *Applied Physics Letters* **72**, 2075–2077 (1998).
- [201] D. R. Ward, F. Hüser, F. Pauly, J. C. Cuevas, and D. Natelson, “Optical rectification and field enhancement in a plasmonic nanogap”, *Nature Nanotechnology* **5**, 732–736 (2010).
- [202] T. C. L. G. Sollner, W. D. Goodhue, P. E. Tannenwald, C. D. Parker, and D. D. Peck, “Resonant tunneling through quantum wells at frequencies up to 2.5 THz”, *Applied Physics Letters* **43**, 588–590 (1983).
- [203] D. Benner, J. Boneberg, P. Nürnberger, R. Waitz, P. Leiderer, and E. Scheer, “Lateral and Temporal Dependence of the Transport through an Atomic Gold Contact under Light Irradiation: Signature of Propagating Surface Plasmon Polaritons”, *Nano Letters* **14**, 5218–5223 (2014).

- [204] D. C. Guhr, D. Rettinger, J. Boneberg, A. Erbe, P. Leiderer, and E. Scheer, “Influence of Laser Light on Electronic Transport through Atomic-Size Contacts”, *Physical Review Letters* **99**, 086801 (2007).
- [205] A. O. Govorov, H. Zhang, and Y. K. Gun’ko, “Theory of Photo-injection of Hot Plasmonic Carriers from Metal Nanostructures into Semiconductors and Surface Molecules”, *The Journal of Physical Chemistry C* **117**, 16616–16631 (2013).
- [206] M. Kornbluth, A. Nitzan, and T. Seideman, “Light-induced electronic non-equilibrium in plasmonic particles”, *The Journal of Chemical Physics* **138**, 174707 (2013).
- [207] R. Sundararaman, P. Narang, A. S. Jermyn, W. A. G. Iii, and H. A. Atwater, “Theoretical predictions for hot-carrier generation from surface plasmon decay”, *Nature Communications* **5**, 5788 (2014).
- [208] M. Bernardi, J. Mustafa, J. B. Neaton, and S. G. Louie, “Theory and computation of hot carriers generated by surface plasmon polaritons in noble metals”, *Nature Communications* **6**, 7044 (2015).
- [209] P. Banerjee, D. Conklin, S. Nanayakkara, T.-H. Park, M. J. Therien, and D. A. Bonnell, “Plasmon-Induced Electrical Conduction in Molecular Devices”, *ACS Nano* **4**, 1019–1025 (2010).
- [210] P. P. Pal, N. Jiang, M. D. Sonntag, N. Chiang, E. T. Foley, M. C. Hersam, R. P. Van Duyne, and T. Seideman, “Plasmon-Mediated Electron Transport in Tip-Enhanced Raman Spectroscopic Junctions”, *The Journal of Physical Chemistry Letters* **6**, 4210–4218 (2015).
- [211] S. F. Tan, L. Wu, J. K. W. Yang, P. Bai, M. Bosman, and C. A. Nijhuis, “Quantum Plasmon Resonances Controlled by Molecular Tunnel Junctions”, *Science* **343**, 1496–1499 (2014).
- [212] A. Thon, M. Merschdorf, W. Pfeiffer, T. Klamroth, P. Saalfrank, and D. Diesing, “Photon-assisted tunneling versus tunneling of excited electrons in metal–insulator–metal junctions”, *Applied Physics A* **78**, 189–199 (2004).
- [213] S. W. Wu, N. Ogawa, and W. Ho, “Atomic-Scale Coupling of Photons to Single-Molecule Junctions”, *Science* **312**, 1362–1365 (2006).
- [214] S. W. Wu and W. Ho, “Two-photon-induced hot-electron transfer to a single molecule in a scanning tunneling microscope”, *Physical Review B* **82**, 085444 (2010).
- [215] J. R. Widawsky, P. Darancet, J. B. Neaton, and L. Venkataraman, “Simultaneous Determination of Conductance and Thermopower of Single Molecule Junctions”, *Nano Letters* **12**, 354–358 (2012).

- [216] M. Tsutsui, M. Taniguchi, and T. Kawai, “Local Heating in Metal-Molecule-Metal Junctions”, *Nano Letters* **8**, 3293–3297 (2008).
- [217] Z. Huang, F. Chen, R. D’agosta, P. A. Bennett, M. Di Ventra, and N. Tao, “Local ionic and electron heating in single-molecule junctions”, *Nature Nanotechnology* **2**, 698–703 (2007).
- [218] M. Wagner and W. Zwerger, “Characteristic scaling parameters for tunneling in strong time-dependent electric fields”, *Physical Review B* **55**, R10217–R10220 (1997).
- [219] S. Hou, J. Zhang, R. Li, J. Ning, R. Han, Z. Shen, X. Zhao, Z. Xue, and Q. Wu, “First-principles calculation of the conductance of a single 4,4 bipyridine molecule”, *Nanotechnology* **16**, 239 (2005).
- [220] Á. J. Pérez-Jiménez, “Uncovering Transport Properties of 4,4'-Bipyridine/Gold Molecular Nanobridges”, *The Journal of Physical Chemistry B* **109**, 10052–10060 (2005).
- [221] M. Kaganov, I. Lifshitz, and L. Tanatarov, “Relaxation between Electrons and the Crystalline Lattice”, *Soviet physics, Journal of Experimental and Theoretical Physics* **4**, 232 (1957).
- [222] D. Pines and P Nozières, Normal Fermi liquids (W.A. Benjamin, New York, 1966).
- [223] W. S. Fann, R. Storz, H. W. K. Tom, and J. Bokor, “Electron thermalization in gold”, *Physical Review B* **46**, 13592–13595 (1992).
- [224] C.-K. Sun, F. Vallée, L. H. Acioli, E. P. Ippen, and J. G. Fujimoto, “Femtosecond-tunable measurement of electron thermalization in gold”, *Physical Review B* **50**, 15337–15348 (1994).
- [225] D. Cvetko, G. Fratesi, G. Kladnik, A. Cossaro, G. P. Brivio, L. Venkataraman, and A. Morgante, “Ultrafast electron injection into photo-excited organic molecules”, *18*, 22140–22145 (2016).
- [226] S. Y. Quek, L. Venkataraman, H. J. Choi, S. G. Louie, M. S. Hybertsen, and J. B. Neaton, “Amine-gold linked single-molecule circuits: experiment and theory”, *Nano Letters* **7**, PMID: 17900162, 3477–3482 (2007).
- [227] S. M. Sze, J. L. Moll, and T. Sugano, “Range-energy relation of hot electrons in gold”, *Solid-State Electronics* **7**, 509–523 (1964).
- [228] H. Kanter, “Slow-Electron Mean Free Paths in Aluminum, Silver, and Gold”, *Physical Review B* **1**, 522–536 (1970).
- [229] N. W. Ashcroft and N. D. Mermin, Solid state physics (Brooks/Cole Thomson Learning, New York, 1976).

- [230] R. L. Olmon, B. Slovick, T. W. Johnson, D. Shelton, S.-H. Oh, G. D. Boreman, and M. B. Raschke, “Optical dielectric function of gold”, *Physical Review B* **86**, 235147 (2012).
- [231] G.-L. Ingold and Y. V. Nazarov, “Charge Tunneling Rates in Ultrasmall Junctions”, in *Single Charge Tunneling: Coulomb Blockade Phenomena In Nanostructures*, edited by H. Grabert and M. H. Devoret, NATO ASI Series (Springer US, Boston, MA, 1992), pp. 21–107.
- [232] J. M. Ziman, *Principles of the theory of solids* (Cambridge University Press, Cambridge, 1999).
- [233] E.-D. Fung, D. Gelbwaser, J. Taylor, J. Low, J. Xia, I. Davydenko, L. M. Campos, S. Marder, U. Peskin, and L. Venkataraman, “Breaking Down Resonance: Nonlinear Transport and the Breakdown of Coherent Tunneling Models in Single Molecule Junctions”, *Nano Letters* **19**, 2555–2561 (2019).
- [234] B. Capozzi, J. Z. Low, J. Xia, Z.-F. Liu, J. B. Neaton, L. M. Campos, and L. Venkataraman, “Mapping the Transmission Functions of Single-Molecule Junctions”, *Nano Letters* **16**, 3949–3954 (2016).
- [235] B. C. Stipe, M. A. Rezaei, W. Ho, S. Gao, M. Persson, and B. I. Lundqvist, “Single-Molecule Dissociation by Tunneling Electrons”, *Physical Review Letters* **78**, 4410–4413 (1997).
- [236] T. Seideman, “Current-driven dynamics in molecular-scale devices”, *Journal of Physics: Condensed Matter* **15**, R521–R549 (2003).
- [237] R. H. M. Smit, C. Untiedt, and J. M. van Ruitenbeek, “The high-bias stability of monatomic chains”, *Nanotechnology* **15**, S472–S478 (2004).
- [238] J. Koch, M. Semmelhack, F. von Oppen, and A. Nitzan, “Current-induced nonequilibrium vibrations in single-molecule devices”, *Physical Review B* **73**, 155306 (2006).
- [239] M. Suzuki, Y. Ominami, Q. Ngo, C. Y. Yang, A. M. Cassell, and J. Li, “Current-induced breakdown of carbon nanofibers”, *Journal of Applied Physics* **101**, 114307 (2007).
- [240] M. Taniguchi, M. Tsutsui, K. Yokota, and T. Kawai, “Inelastic electron tunneling spectroscopy of single-molecule junctions using a mechanically controllable break junction”, *Nanotechnology* **20**, 434008 (2009).
- [241] H. Li, T. A. Su, V. Zhang, M. L. Steigerwald, C. Nuckolls, and L. Venkataraman, “Electric Field Breakdown in Single Molecule Junctions”, *Journal of the American Chemical Society* **137**, 5028–5033 (2015).

- [242] H. Li, N. T. Kim, T. A. Su, M. L. Steigerwald, C. Nuckolls, P. Darancet, J. L. Leighton, and L. Venkataraman, “Mechanism for Si–Si Bond Rupture in Single Molecule Junctions”, *Journal of the American Chemical Society* **138**, 16159–16164 (2016).
- [243] M. L. Perrin, C. J. O. Verzijl, C. A. Martin, A. J. Shaikh, R. Eelkema, J. H. van Esch, J. M. van Ruitenbeek, J. M. Thijssen, H. S. J. van der Zant, and D. Dulić, “Large tunable image-charge effects in single-molecule junctions”, *Nature Nanotechnology* **8**, 282–287 (2013).
- [244] G. Kuang, S.-Z. Chen, W. Wang, T. Lin, K. Chen, X. Shang, P. N. Liu, and N. Lin, “Resonant Charge Transport in Conjugated Molecular Wires beyond 10 nm Range”, *Journal of the American Chemical Society* **138**, 11140–11143 (2016).
- [245] B. Xu and Y. Dubi, “Negative differential conductance in molecular junctions: an overview of experiment and theory”, *Journal of Physics: Condensed Matter* **27**, 263202 (2015).
- [246] X. Xiao, L. A. Nagahara, A. M. Rawlett, and N. Tao, “Electrochemical Gate-Controlled Conductance of Single Oligo(phenylene ethynylene)s”, *Journal of the American Chemical Society* **127**, 9235–9240 (2005).
- [247] N. Kang, A. Erbe, and E. Scheer, “Observation of negative differential resistance in DNA molecular junctions”, *Applied Physics Letters* **96**, 023701 (2010).
- [248] M. L. Perrin, R. Frisenda, M. Koole, J. S. Seldenthuis, J. A. C. Gil, H. Valkenier, J. C. Hummelen, N. Renaud, F. C. Grozema, J. M. Thijssen, D. Dulić, and H. S. J. van der Zant, “Large negative differential conductance in single-molecule break junctions”, *Nature Nanotechnology* **9**, 830–834 (2014).
- [249] G. Kuang, S. Z. Chen, L. Yan, K. Q. Chen, X. Shang, P. N. Liu, and N. Lin, “Negative Differential Conductance in Polyporphyrin Oligomers with Nonlinear Backbones”, *Journal of the American Chemical Society* **140**, 570–573 (2018).
- [250] J. Chen, M. A. Reed, A. M. Rawlett, and J. M. Tour, “Large On-Off Ratios and Negative Differential Resistance in a Molecular Electronic Device”, *Science* **286**, 1550–1552 (1999).
- [251] F. Schwarz, G. Kastlunger, F. Lissel, H. Riel, K. Venkatesan, H. Berke, R. Stadler, and E. Lörtscher, “High-Conductive Organometallic Molecular Wires with Delocalized Electron Systems Strongly Coupled to Metal Electrodes”, *Nano Letters* **14**, 5932–5940 (2014).
- [252] B. Muralidharan and S. Datta, “Generic model for current collapse in spin-blockaded transport”, *Physical Review B* **76**, 035432 (2007).
- [253] A. Migliore and A. Nitzan, “Nonlinear Charge Transport in Redox Molecular Junctions: A Marcus Perspective”, *ACS Nano* **5**, 6669–6685 (2011).

- [254] A. Migliore and A. Nitzan, “Irreversibility and Hysteresis in Redox Molecular Conduction Junctions”, *Journal of the American Chemical Society* **135**, 9420–9432 (2013).
- [255] M. Galperin, M. A. Ratner, and A. Nitzan, “Hysteresis, switching, and negative differential resistance in molecular junctions: a polaron model”, *Nano Letters* **5**, PMID: 15792425, 125–130 (2005).
- [256] S. Yeganeh, M. Galperin, and M. A. Ratner, “Switching in molecular transport junctions: polarization response”, *Journal of the American Chemical Society* **129**, 13313–13320 (2007).
- [257] J. Ulrich, D. Esrail, W. Pontius, L. Venkataraman, D. Millar, and L. H. Doerrer, “Variability of Conductance in Molecular Junctions”, *The Journal of Physical Chemistry B* **110**, 2462–2466 (2006).
- [258] E. J. Dell, B. Capozzi, J. Xia, L. Venkataraman, and L. M. Campos, “Molecular length dictates the nature of charge carriers in single-molecule junctions of oxidized oligothiophenes”, *Nature Chemistry* **7**, 209–214 (2015).
- [259] L. A. Nagahara, T. Thundat, and S. M. Lindsay, “Preparation and characterization of STM tips for electrochemical studies”, *Review of Scientific Instruments* **60**, 3128–3130 (1989).
- [260] A. A. Dzhioev and D. S. Kosov, “Solvent-induced current-voltage hysteresis and negative differential resistance in molecular junctions”, *Physical Review B* **85**, 033408 (2012).
- [261] D. V. Matyushov, “Solvent reorganization energy of electron-transfer reactions in polar solvents”, *The Journal of Chemical Physics* **120**, 7532–7556 (2004).
- [262] R. A. Marcus, “Electrostatic Free Energy and Other Properties of States Having Nonequilibrium Polarization. I”, *The Journal of Chemical Physics* **24**, 979–989 (1956).
- [263] L. V. Slipchenko, T. E. Munsch, P. G. Wentholt, and A. I. Krylov, “5-Dehydro-1,3-quinodimethane: A Hydrocarbon with an Open-Shell Doublet Ground State”, *Angewandte Chemie International Edition* **43**, 742–745 (2004).
- [264] R. Pati, M. McClain, and A. Bandyopadhyay, “Origin of Negative Differential Resistance in a Strongly Coupled Single Molecule-Metal Junction Device”, *Physical Review Letters* **100**, 246801 (2008).
- [265] D. M. Cardamone and G. Kirczenow, “Single-molecule device prototypes for protein-based nanoelectronics: Negative differential resistance and current rectification in oligopeptides”, *Physical Review B* **77**, 165403 (2008).
- [266] E. G. Emberly and G. Kirczenow, “Current-driven conformational changes, charging, and negative differential resistance in molecular wires”, *Physical Review B* **64**, 125318 (2001).

- [267] J. M. Seminario, A. G. Zacarias, and J. M. Tour, “Theoretical Study of a Molecular Resonant Tunneling Diode”, *Journal of the American Chemical Society* **122**, 3015–3020 (2000).
- [268] G. C. Solomon, D. Q. Andrews, R. P. V. Duyne, and M. A. Ratner, “Electron Transport through Conjugated Molecules: When the  $\pi$  System Only Tells Part of the Story”, *ChemPhysChem* **10**, 257–264 (2009).
- [269] S. Woitellier, J. P. Launay, and C. Joachim, “The possibility of molecular switching: Theoretical study of  $[(\text{NH}_3)_5\text{Ru}-4,4'\text{-bipy}-\text{Ru}(\text{NH}_3)_5]^{5+}$ ”, *Chemical Physics* **131**, 481–488 (1989).
- [270] M. Büttiker, “Coherent and sequential tunneling in series barriers”, *IBM Journal of Research and Development* **32**, 63–75 (1988).
- [271] U. Peskin, “Analysis of a dissipative resonant tunneling trap by temperature-dependent Langevin–Schrödinger equations”, *The Journal of Chemical Physics* **113**, 7479–7487 (2000).
- [272] A. M. Kuznetsov and J. Ulstrup, “Mechanisms of in Situ Scanning Tunnelling Microscopy of Organized Redox Molecular Assemblies”, *The Journal of Physical Chemistry A* **104**, 11531–11540 (2000).
- [273] J. K. Sowa, J. A. Mol, G. A. D. Briggs, and E. M. Gauger, “Beyond Marcus theory and the Landauer–Büttiker approach in molecular junctions: A unified framework”, *The Journal of Chemical Physics* **149**, 154112 (2018).
- [274] D. A. Ryndyk, P. D’Amico, G. Cuniberti, and K. Richter, “Charge-memory polaron effect in molecular junctions”, *Physical Review B* **78**, 085409 (2008).
- [275] C. Kergueris, J.-P. Bourgoin, S. Palacin, D. Esteve, C. Urbina, M. Magoga, and C. Joachim, “Electron transport through a metal-molecule-metal junction”, *Physical Review B* **59**, 12505–12513 (1999).
- [276] R. Frisenda, D. Stefani, and H. S. J. van der Zant, “Quantum Transport through a Single Conjugated Rigid Molecule, a Mechanical Break Junction Study”, *Accounts of Chemical Research* **51**, 1359–1367 (2018).
- [277] Y. Isshiki, S. Fujii, T. Nishino, and M. Kiguchi, “Fluctuation in Interface and Electronic Structure of Single-Molecule Junctions Investigated by Current versus Bias Voltage Characteristics”, *Journal of the American Chemical Society* **140**, 3760–3767 (2018).
- [278] Y. Isshiki, Y. Matsuzawa, S. Fujii, and M. Kiguchi, “Investigation on Single-Molecule Junctions Based on Current–Voltage Characteristics”, *Micromachines* **9**, 67 (2018).
- [279] L. Simeral and R. L. Amey, “Dielectric properties of liquid propylene carbonate”, *The Journal of Physical Chemistry* **74**, 1443–1446 (1970).

- [280] K. Luka-Guth, S. Hambsch, A. Bloch, P. Ehrenreich, B. M. Briechle, F. Kilibarda, T. Sendler, D. Sysoiev, T. Huhn, A. Erbe, and E. Scheer, “Role of solvents in the electronic transport properties of single-molecule junctions”, *Beilstein Journal of Nanotechnology* **7**, 1055–1067 (2016).
- [281] V. Blum, R. Gehrke, F. Hanke, P. Havu, V. Havu, X. Ren, K. Reuter, and M. Scheffler, “Ab initio molecular simulations with numeric atom-centered orbitals”, *Computer Physics Communications* **180**, 2175–2196 (2009).
- [282] V. Havu, V. Blum, P. Havu, and M. Scheffler, “Efficient O(N) integration for all-electron electronic structure calculation using numeric basis functions”, *Journal of Computational Physics* **228**, 8367–8379 (2009).
- [283] J. P. Perdew, K. Burke, and M. Ernzerhof, “Generalized Gradient Approximation Made Simple”, *Physical Review Letters* **77**, 3865–3868 (1996).
- [284] M. Koentopp, K. Burke, and F. Evers, “Zero-bias molecular electronics: Exchange-correlation corrections to Landauer’s formula”, *Physical Review B* **73**, 121403 (2006).